Hybrid-PIC Modeling of Hall Thruster Plumes

by

David Marshall Brenizer

Submitted to the Department of Aeronautics and Astronautics in partial fulfillment of the requirements for the degree of

Master of Science

at the

MASSACHUSETTS INSTITUTE OF TECHNOLOGY

September 2000

Author.....
Department of Aeronautics and Astronautics
August 4, 2000

Certified by.....
Professor Manuel Martinez-Sanchez
Department of Aeronautics and Astronautics
Thesis Supervisor

Accepted by.....
Dr. Nesbitt Hagood
Chairman, Departmental Committee on Graduate Studies
Department of Aeronautics and Astronautics

Hybrid-PIC Modeling of Hall Thruster Plumes

by
David Marshall Brenizer

Submitted to the Department of Aeronautical and Astronautical Engineering on August 4, 2000, in partial fulfillment of the requirements for the degree of Master of Science in Engineering

Abstract

While electric propulsion engines offer performance advantages for many space missions, the potential interactions between the plume and the spacecraft environment are not as well understood. Potential, temperature, and ion density oscillations, charge exchange collisions, non-quasi-neutrality away from the thrust centerline, the Earth's magnetic field, and near-threshold sputtering of engine component surfaces all affect the structure of the plume in a Hall thruster. Modeling these phenomena are crucial to predicting the effects of interactions between the plume and the space environment.

In this work, Dr. Mike Fife's simulation of a Hall thruster is modified and extended to explore unsteady behavior in the plume and model the charge exchange collision process and its effects. It has been determined that Fife's algorithm can be extended to cover the plume region up to the point at which the Earth's magnetic field is equal to that of the engine without negatively affecting the calculated temperature and potential distributions. By extending the grid, oscillations in potential, temperature, and ion density are tracked from station to station as the ions move downstream.

Charge exchange collisions create low speed ions in the plume, many of which travel backwards towards the engine and spacecraft. The presence of these ions creates additional peaks in the energy distributions at angles away from the engine centerline. The presence of a few high energy ions are found in those regions greater than 80°, which agrees with some existing experimental data.

Thesis Supervisor: Manuel Martinez-Sanchez
Title: Professor of Aeronautics and Astronautics

Acknowledgements

First, I would like to thank Professor Martinez-Sanchez. His guidance and wisdom was instrumental in motivating me to complete this work. Throughout the later part of my MIT career, he has been an inspiration and mentor in the field of rocket science. I left each meeting with him confident that all the problems and hang-ups would quickly fade away.

I thank my friends and family. Although many of them did not understand my desire to continue studying this stuff, they were supportive and understanding all the time. They provided the necessary distractions that have made life at MIT not only bearable, but often fun.

Finally, thank you Shivaun. Her presence at my side made all the stress and discomforts of graduate life fade away. I could not have enjoyed myself so much without all the people around me.

This work was sponsored in part by the Massachusetts Space Grant Consortium.

Table of Contents

CHAPTER 1: INTRODUCTION 11

1.1 BACKGROUND 11
1.2 BENEFITS OF ELECTRIC PROPULSION 12
1.3 POTENTIAL HAZARDS OF ELECTRIC PROPULSION 13
1.3.1 Unsteady Current Oscillations 14
1.3.2 Engine Deposition 15
1.3.3 Plume – Spacecraft Interactions 15
1.4 MOTIVATION FOR RESEARCH 17

CHAPTER 2: HALL THRUSTER PHYSICS 19

2.1 PLASMAS 19
2.2 HALL THRUSTER HISTORY 19
2.3 BASICS OF THRUSTER OPERATION 20
2.3.1 SPT-100 22
2.3.2 Future Engine Designs 22
2.4 HALL THRUSTER RESEARCH 23
2.4.1 Computational Hall Thruster Research 24
2.4.2 Experimental Work 25

CHAPTER 3: EXISTING MIT HALL THRUSTER PLUME SIMULATIONS 29

3.1 D. OH'S PLUME MODEL 29
3.1.1 D. Oh's Assumptions 29
3.1.2 Later Modifications of Oh's Code 30
3.1.3 Applicability 30
3.2 UNSTEADY 2D HYBRID-PIC SIMULATION OF A HALL THRUSTER 31
3.2.1 Fife's Assumptions 31
3.2.2 Later Modifications of Fife's Code 32
3.2.3 Applicability 32
3.2.4 Baseline Results 32
3.3 OTHER WORK AT MIT 36

CHAPTER 4: PHYSICS IN THE PLUME 38

4.1 PLUME CURRENT 38
4.1.1 Boundary Conditions 39
4.2 COLLISION THEORY 39
4.2.1 Collision Cross-Section 40
4.2.2 Particle Number Density 42
4.3 ONE-DIMENSIONAL RESULTS 43
4.3.1 Relative Velocity 43
4.3.2 Number Density Data 43
4.3.3 Charge Exchange Rate 44
4.3.4 Comparison to Ionization Rate 45

CHAPTER 5: COMPUTATIONAL METHODS 49

5.1 MAGNETIC FIELD EXTENSION 49
5.1.1 Magnetic Field Strength 51
5.2 ELECTRON EQUATION ASSUMPTIONS 54
5.2.1 Discussion 56
5.2.2 Recommendations 57
5.3 CHARGE EXCHANGE COLLISIONS 57
5.3.1 Ionization vs. Charge Exchange Collision Rates 58

CHAPTER 6: GEOMETRY **61**

6.1 HARDWARE 61
6.2 TWO-DIMENSIONAL APPROXIMATION 62
6.3 GRID GENERATION 63
6.3.1 Near-Field Plume *63*
6.3.2 Far-Field Plume *64*

CHAPTER 7: SIMULATION RESULTS **67**

7.1 BASELINE PLUME CHARACTERISTICS WITH EXPANDED GRID 67
7.1.1 Potential *67*
7.1.2 Electric Field *69*
7.1.3 Ion Velocity *70*
7.1.4 Ion Density *71*
7.1.5 Electron Temperature *72*
7.1.6 Charge-Exchange Collisions *74*
7.2 UNSTEADY PLUME CHARACTERISTICS 75
7.3 EFFECT OF CHARGE EXCHANGE COLLISIONS 87
7.3.1 Two-Dimensional Results *88*
7.3.2 Charge Exchange Ions in the Plume *91*
7.3.3 Charge Exchange Ions in the Backflow Region *94*
7.3.4 Energy Distribution in the Plume *97*

CHAPTER 8: CONCLUSIONS AND RECOMMENDATIONS **105**

8.1 NET CURRENT IN THE PLUME 105
8.1.1 Recommendations *105*
8.2 UNSTEADY PLUME SIMULATION DATA 106
8.2.1 Recommendations *107*
8.3 EFFECT OF CHARGE EXCHANGE COLLISIONS 107
8.3.1 Recommendations *109*

CHAPTER 9: REFERENCES **111**

APPENDIX A: UNSTEADY DATA WITH CEX **113**

APPENDIX B: SAMPLE INPUT FILES **121**

List of Figures

FIGURE 1.1: OSCILLATIONS IN CURRENT AND ISP FOR SPT-100. RESULTS FROM SIMULATION. 15
FIGURE 1.2: HALL THRUSTER ON A SATELLITE: SPACECRAFT-PLUME INTERACTIONS. 18
FIGURE 2.1: SPT-100 HALL EFFECT THRUSTER USED IN TESTING. 21
FIGURE 2.2: CROSS-SECTION SCHEMATIC OF AN "SPT-100-LIKE" THRUSTER. 21
FIGURE 2.3:ION CURRENT AS A FUNCTION OF ION VOLTAGE AT 0.5 M RADIUS FROM THE SPT-100 FOR POINTS AT 80, 90, 100, AND 110 DEGREES OFF THRUST AXIS [KING, 1998] 26
FIGURE 2.4: ION CURRENT AS A FUNCTION OF ION VOLTAGE AT 1.0 M RADIUS FROM THE SPT-100 FOR POINTS AT 80, 90, 100, AND 110 DEGREES OFF THRUST AXIS [KING, 1998] 27
FIGURE 3.1: ANODE CURRENT AND ISP VS. TIME FOR THE BASELINE SIMULATION. 33
FIGURE 3.2: BEAM CURRENT AND ANODE VOLTAGE VS. TIME FOR BASELINE SIMULATION. 34
FIGURE 3.3: ELECTRON TEMPERATURE [EV], BASELINE. 35
FIGURE 3.4: POTENTIAL [V], BASELINE. 35
FIGURE 3.5: ION DENSITY [M^{-3}], BASELINE. 36
FIGURE 4.1: DIAGRAM OF 2 BODY CLASSICAL COLLISION 40
FIGURE 4.2: CEX CROSS-SECTION [M^2]. SOLID LINE: Xe^+. DOTTED LINE: Xe^{++} (DOUBLE ELECTRON TRANSFER). 41
FIGURE 4.4: EXHAUST FLOW DATA FROM SIMULATION OF SPT-70. ENGINE EXIT PLANE AT X =0.04M. 44
FIGURE 4.5: ONE-DIMENSIONAL AVERAGED CHARGE EXCHANGE COLLISION RATE. ENGINE EXIT PLANE AT X =0.04M. 45
FIGURE 4.6: COMPARISON BETWEEN CHARGE EXCHANGE RATE AND IONIZATION RATE IN THRUSTER. ENGINE EXIT PLANE AT X =0.04M. 47
FIGURE 5.1: MAGNETIC FIELD POTENTIAL LINES FOR SPT-100. 50
FIGURE 5.2: "LAMBDA," THE MAGNETIC STREAM FUNCTION PLOTTED FOR SPT-100 SIMULATION. CATHODE AT R=0.07M. 51
FIGURE 5.3: VECTOR PLOT OF MAGNETIC FIELD LINES IN THE SPT-100. 52
FIGURE 5.4: VECTOR PLOT OF MAGNETIC FIELD LINES IN SPT-100 ACCELERATION ZONE. 53
FIGURE 5.5: MAGNETIC FIELD STRENGTH. THE FINAL CONTOUR CORRESPONDS TO $5x10^{-5}$. 54
FIGURE 5.6: ELECTRON TEMPERATURE, ASSUMING ZERO NET CURRENT IN THE PLUME. CATHODE AT R=0.07M. 55
FIGURE 5.7: SPACE POTENTIAL, ASSUMING ZERO NET CURRENT IN THE PLUME. CATHODE AT R=0.07M. 56
FIGURE 5.8: IONIZATION RATE IN THE PLUME. [$M^{-3}S^{-1}$] 59
FIGURE 5.9: CHARGE EXCHANGE RATE IN THE PLUME. [$M^{-3}S^{-1}$] 60
FIGURE 6.1: SPT-100 USED IN TESTING AT THE UNIVERSITY OF MICHIGAN 61
FIGURE 6.2: FRONT AND SIDE VIEWS OF SPT-100 WITH CRITICAL DIMENSIONS. 62
FIGURE 6.3: TWO-DIMENSIONAL GRID FOR NEAR-FIELD SPT-100 GEOMETRY. 64
FIGURE 7.1: SPACE POTENTIAL (V) PLOTTED IN THE ENGINE GEOMETRY. CATHODE AT R=0.07M. 68
FIGURE 7.2: ZOOM IN FOR BASELINE POTENTIAL CONTOURS. CATHODE AT R=0.07M. 69
FIGURE 7.3: ELECTRIC FIELD NEAR ACCELERATION ZONE. 70
FIGURE 7.4: AVERAGE ION VELOCITY. 71
FIGURE 7.5: ION NUMBER DENSITY IN NEAR PLUME REGION. [M^{-3}] 72
FIGURE 7.6: ELECTRON TEMPERATURE [EV]. 73
FIGURE 7.7: ELECTRON TEMPERATURE [EV] – ZOOM IN. 74
FIGURE 7.8:CHARGE EXCHANGE COLLISION RATE. [$M^{-3}S^{-1}$] 74
FIGURE 7.9: SIMULATION PROBE LOCATIONS, SUPER IMPOSED ON THE GRID. 75
FIGURE 7.10: ANODE CURRENT AND ISP FOR HALL THRUSTER SIMULATION. 76
FIGURE 7.11: BEAM CURRENT AND ANODE VOLTAGE FOR SPT-100 SIMULATION. 77
FIGURE 7.12: POTENTIAL VS. TIME IN THE ACCELERATION ZONE, BOTH AXIAL STATIONS SHOWN. 78
FIGURE 7.13: ELECTRON TEMPERATURE VS. TIME IN ACCELERATION ZONE. 79
FIGURE 7.14: ION DENSITY VS. TIME IN ACCELERATION ZONE. 80
FIGURE 7.15: POTENTIAL VS. TIME AT THE EXIT PLANE. 80

FIGURE 7.16: ELECTRON TEMPERATURE VS. TIME AT THE EXIT PLANE. 81
FIGURE 7.17: ION DENSITY VS. TIME AT THE EXIT PLANE. 82
FIGURE 7.18: POTENTIAL VS. TIME, 0.06 M FROM ANODE. (3.5 CM FROM EXIT PLANE) 82
FIGURE 7.19: ELECTRON TEMPERATURE VS. TIME, 0.06 M FROM ANODE. (3.5 CM FROM EXIT PLANE) 83
FIGURE 7.20: ION DENSITY VS. TIME 0.06 M FROM ANODE. (3.5 CM FROM EXIT PLANE) 83
FIGURE 7.21: POTENTIAL VS. TIME, 0.1 M FROM ANODE. (7.5 CM FROM EXIT PLANE) 84
FIGURE 7.22: ELECTRON TEMPERATURE VS. TIME, 0.1 M FROM ANODE. (7.5 CM FROM EXIT PLANE) 84
FIGURE 7.23: ION DENSITY VS. TIME, 0.1 M FROM ANODE. (7.5 CM FROM EXIT PLANE) 85
FIGURE 7.24: ION DENSITY AT SUCCESSIVE DOWNSTREAM LOCATIONS VS. TIME. 86
FIGURE 7.25: CLOSE COMPARISON OF OSCILLATIONS IN SPT-100. 87
FIGURE 7.26: PLASMA POTENTIAL [V] FOR SPT-100 SIMULATION, INCLUDING CEX. 88
FIGURE 7.27: ION DENSITY [M^{-3}]IN SPT-100 SIMULATION, INCLUDING CEX. 89
FIGURE 7.28: ELECTRON TEMPERATURE [EV] FOR SPT-100 SIMULATION, INCLUDING CHARGE EXCHANGE. 90
FIGURE 7.29: SPT-100 SIMULATED PERFORMANCE WITH CEX COLLISIONS PRESENT. 91
FIGURE 7.30: BEAM CURRENT DENSITY [A/CM^2] IN THE PLUME, AS A FUNCTION OF DIVERGENCE ANGLE. 92
FIGURE 7.31: VELOCITY PHASE-SPACE PLOT FOR IONS IN THE PLUME. 93
FIGURE 7.32: VELOCITY PHASE-SPACE PLOTS FOR CEX IONS. 94
FIGURE 7.33: VELOCITY PHASE-SPACE PLOT FOR IONS IN THE BACK FLOW REGION. 95
FIGURE 7.34: DISTRIBUTION OF ION HITS ALONG A RADIAL "BACK PLATE." ($1.5X10^{-5}$ SECONDS) 96
FIGURE 7.35: ENERGY DISTRIBUTION IN THE BACKFLOW REGION. ($1.5X10^{-5}$ SECONDS) 97
FIGURE 7.36: PLUME ENERGY DISTRIBUTION, 0-7° OFF-AXIS. [NUMBER OF PARTICLES PER CELL] 98
FIGURE 7.37: PLUME ENERGY DISTRIBUTION, 7-14° OFF-AXIS. [NUMBER OF PARTICLES PER CELL] 99
FIGURE 7.38: PLUME ENERGY DISTRIBUTION, 14-21° OFF-AXIS. [NUMBER OF PARTICLES PER CELL] 99
FIGURE 7.39: PLUME ENERGY DISTRIBUTION, 21-28° OFF-AXIS. [NUMBER OF PARTICLES PER CELL] 100
FIGURE 7.40: PLUME ENERGY DISTRIBUTION, 28-35° OFF-AXIS. [NUMBER OF PARTICLES PER CELL] 100
FIGURE 7.41: PLUME ENERGY DISTRIBUTION, 35-42° OFF-AXIS. [NUMBER OF PARTICLES PER CELL] 101
FIGURE 7.42: PLUME ENERGY DISTRIBUTION, 42-49° OFF-AXIS. [NUMBER OF PARTICLES PER CELL] 101
FIGURE 7.43: PLUME ENERGY DISTRIBUTION, 49-56° OFF-AXIS. [NUMBER OF PARTICLES PER CELL] 102
FIGURE 7.44: PLUME ENERGY DISTRIBUTION, 56-63° OFF-AXIS. [NUMBER OF PARTICLES PER CELL] 102
FIGURE 7.45: PLUME ENERGY DISTRIBUTION, 63-70° OFF-AXIS. [NUMBER OF PARTICLES PER CELL] 103
FIGURE 7.46: PLUME ENERGY DISTRIBUTION, 70-77° OFF-AXIS. [NUMBER OF PARTICLES PER CELL] 103
FIGURE 7.47: PLUME ENERGY DISTRIBUTION, 77-84° OFF-AXIS. [NUMBER OF PARTICLES PER CELL] 104
FIGURE A.1: POTENTIAL VS. TIME IN THE ACCELERATION ZONE, BOTH AXIAL STATIONS SHOWN. 113
FIGURE A.2: ELECTRON TEMPERATURE VS. TIME IN THE ACCELERATION ZONE. 114
FIGURE A.3: ION DENSITY IN ACCELERATION ZONE. 114
FIGURE A.4: POTENTIAL AT THE EXIT PLANE. 115
FIGURE A.5: ELECTRON TEMPERATURE AT THE EXIT PLANE. 115
FIGURE A.6: ION DENSITY AT THE EXIT PLANE. 116
FIGURE A.7: POTENTIAL, 0.06 M FROM THE ANODE. 116
FIGURE A.8: ELECTRON TEMPERATURE 0.06M FROM THE ANODE. 117
FIGURE A.9: ION DENSITY 0.06 M FROM THE ANODE. 117
FIGURE A.10: POTENTIAL, 0.1 M FROM THE ANODE. 118
FIGURE A.11: ELECTRON TEMPERATURE, 0.1 M FROM THE ANODE. 118
FIGURE A.12: ION DENSITY, 0.1 M FROM THE ANODE. 119

Chapter 1: Introduction

The choice of propulsion system is an important part of space mission design; the propellant mass and associated launch costs consume a large portion of system budgets. There are two main divisions of propulsion systems: chemical, where the energy is provided through chemical reactions in the propellant, and electric, where the energy is added from a source external to the propellant. The following sections describe some of the design trades between the two propulsion system types, as well as the research issues associated with operating an electric propulsion system, specifically a Hall Effect Thruster.

1.1 Background

Current satellites and space vehicles require large mass fractions for propellant, as performance is limited by the rocket equation, relating velocity change to mass change. As the specific impulse, Isp, increases, less propellant mass is required for the same "delta v" providing a higher level of efficiency.

$$M_{propellant} = M_0(1 - e^{-\frac{\Delta V}{c}}) \tag{1.1}$$

There are two main trends in spacecraft design that require higher engine efficiency and less propellant weight:

- Longer lifetimes for Earth-orbiting satellites, with higher lifetime delta v requirements.
- Interplanetary spacecraft that execute high delta v maneuvers over a long mission lifetime, traveling farther into the solar system.

For Earth-orbiting missions, station keeping is required to correct for disturbances to the orbit from atmospheric drag, the effect of the sun, moon, and planets, and the variation in the curvature and magnetic fields of the Earth. For satellites near a geosynchronous orbit

where drag is not an issue, North-South station keeping (NSSK), which is required to counteract the effects of the sun and moon, is the greatest delta v requirement, at about 50 m/s a year. Over a 10-year lifetime of the mission, this could be a significant quantity of propellant, depending on the size of the satellite system.

Chemical rockets, which are extensively used today, offer low relative efficiency as compared with electric propulsion. Cold gas thrusters, such as Nitrogen, have an exhaust velocity of about 700 m/s (Isp = 70 seconds). Hydrazine, a popular choice for most large satellites, approaches 2300 m/s, while state of the art hydrogen-oxygen or hydrogen-fluorine engines might conceivably reach 5000 m/s. However, it is difficult to store cryogenic propellants for the duration of a long-term space mission, so hydrazine tends to be the favorite choice. However, hydrazine is extremely toxic, incurring additional handling costs. Therefore, engineers look towards means of adding energy to the exhaust flow from sources other than chemical energy.

1.2 Benefits of Electric Propulsion

Electric propulsion has been a popular alternative to chemical rockets in recent history. An electric power device is used to add energy to the flow, separating the energy production and the energy conversion functions of the engine. There are three main categories of EP devices, depending on how the energy is added to the flow:

- Electrothermal: adding heat to the flow (resistojet, arcjet).
- Electrostatic: accelerating charged particles in an electric field (ion engine, closed drift thruster).
- Electromagnetic: accelerating particles with a magnetic field (MPD, PPT).

Electric propulsion devices can create exhaust velocities an order of magnitude higher than chemical rockets, making them about 10 times as efficient in reducing mass. Specifically, Hall thrusters, also called closed-drift or stationary plasma thrusters, have an exhaust velocity of 16000 m/s, or about 3-4 times as good as the very best cryogenic

chemical systems. EP devices trade thrust for fuel efficiency, though. Equation 1.2 shows that for a limited power system, an engine with a high exhaust velocity must have a low thrust.

Mission planners can take advantage of the fact that once on-orbit, there is enough time built into the mission to accommodate low thrust maneuvers. Rather than fire a large engine for 10 seconds and then drift for a month, the spacecraft should take advantage of the high efficiency of electric propulsion and just thrust for the entire month, completing the same delta v maneuver.

$$\eta P = \frac{1}{2} Fc \qquad (1.2)$$

For space missions, the delta v requirements can be used to optimize the engine exhaust velocity. For most on-orbit maneuvers, including North-South station keeping, the optimum exhaust velocity is between 10 and 20 km/s – the very same region covered by the Hall thruster. The Russians have continued to develop this technology since the 1960's. As a result, the United States has adopted the use of this technology and is now beginning to enter a phase of on-orbit usage and experience. The economic pressures facing space flight have made this technology even more desirable.

1.3 Potential Hazards of Electric Propulsion

Clearly, electric propulsion, specifically Hall thrusters, offers the potential for large monetary savings over the lifetime of a satellite. However, some aspects of the technology are still not well understood. The potential side effects of operating electric propulsion devices on a spacecraft could increase the risk of failure and reduce spacecraft lifetime if not properly controlled. Some of these issues include:

- Unsteady engine behavior
- Deposition of engine metals on spacecraft components
- Ion impact with spacecraft components, sputtering of spacecraft materials
- Plasma beam interference with communications

When modeling engine operation, it is important to examine these potential effects on the spacecraft environment, as well as understand their implications on engine performance.

1.3.1 Unsteady Current Oscillations

Hall thruster operation is an unsteady process; there are severe time-dependent oscillations in beam current that change over the lifetime of the engine. The standard analysis method is to just time-average the performance. These oscillations, thought to be created by instabilities in the plasma, are the reason the United States abandoned the technology 30 years ago. Lifetime testing indicates that the oscillation amplitudes saturate, often at 100% current modulation, but they erode performance over the lifetime of the engine. As a result, complicated power processing units are required to maintain constant voltage during engine operation, but even then, the current may oscillate strongly.

Figure 1.1 shows a simulation of the current oscillations, and resulting fluctuations in Isp. The current can vary by as much as three or four amps above or below the average operating conditions of 4.5 A. The oscillations are fast enough that the engine performance can be time averaged. However, studying the development of these oscillations over time is important for lifetime testing and for studying interference between the plume and any communication or sensor signals.

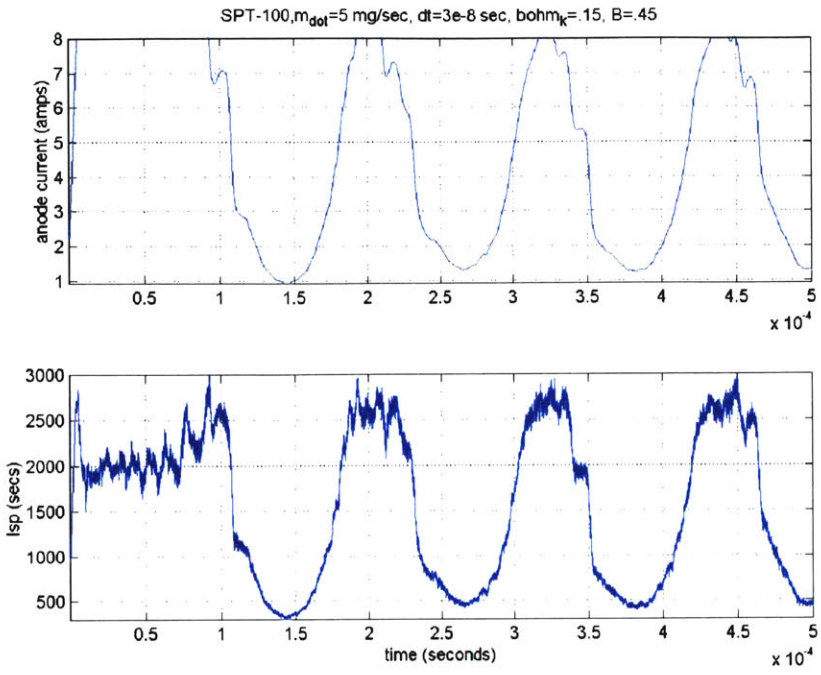

Figure 1.1: Oscillations in current and Isp for SPT-100. Results from simulation.

1.3.2 Engine Deposition

Inside the engine, high-energy ions collide with the acceleration chamber walls or ion engine grids. These collisions sputter insulating material from the walls and grids, which travels out of the engine into the spacecraft environment. These particles can deposit on spacecraft components such as solar array panels, sensors, or other sensitive pieces of equipment. Studying this deposition in the laboratory is difficult, as material sputtered from the tank walls in a ground test would be difficult to distinguish from the engine material. This deposition can erode solar array performance and inhibit payload operations.

1.3.3 Plume – Spacecraft Interactions

Additionally, the space environment provides unique problems for Hall thrusters and the interaction between the thruster plume and the spacecraft. The background environment, including the spacecraft, is at a lower potential than the ions in the plume. Thus positive

Xenon atoms would tend to ride down the potential well and fly back into the spacecraft. Most ions, however, are traveling too fast for the potential to draw them backwards. However, there is a phenomenon in the plume that creates "charge exchange ions" (CEX). In this process, high-speed ions collide with low speed neutrals coming out of the engine. An energetic electron can jump from the neutral to the ion, leaving a high speed neutral and a low speed ion. These charge exchange ions are moving slow enough to be drawn out of the plume and back into the spacecraft due to the potential difference, facilitated by the high vacuum of space. These ions, while traveling relatively slowly, still carry plenty of energy with which to create further collisions with the walls of the spacecraft, as they gain energy from sheaths around spacecraft components. The solar panels are potentially susceptible to collisions with the charge exchange ions, as thrusters for North-South station keeping are pointed parallel to the solar panels, in the N-S axis. Also, solar panels tend to float at some moderately large negative potential because their positive end draws more electrons from the plasma than the negative end.

Simulations have been run in vacuum tanks on Earth, however it is difficult to accurately reproduce the high vacuum of space. Tank simulations tend to have re-circulation of the plasma, as well as sputtering from the tank walls. It is difficult to distinguish between the re-circulated ions and the charge exchange ions that might collide with the thruster mount, representing the satellite body.

The exhaust beam, which may grow wider due to the effect of CEX ions in the plume, can also interfere with communications to the spacecraft. The plume, interfering with antennas, will shield communications operating at less than the plasma frequency. Most communications occur at well above the plasma frequency in order to penetrate the ionosphere; however, extra care should be taken to model exhaust plumes that might cross the field of view of an antenna. [Samanta Roy, 1994] Even above the plasma frequency, there are phase shifts in the signal due to passage through the plasma beam. If the plasma is inhomogeneous, the signal will be scattered. A time varying plasma will introduce other modulations.

1.4 Motivation for Research

Do to the lack of understanding in some areas of Hall Thruster operations, as well as a commercial advantage seen in their use, extensive modeling and simulation efforts have begun in earnest. The goal is to develop simulations that accurately predict performance of a Hall thruster and model the shape and characteristics of the plume. Some factors that affect the shape of the plume that are not yet modeled are:

- Plume fluctuations (potential, temperature, ion density)
- Near-field charge exchange collisions
- Non-quasi-neutrality in the off-axis plume region
- Geo-magnetic field lines on the scale of a spacecraft
- Near-threshold sputtering of engine component surfaces

All of these topics directly affect predictions about the interaction between the plume and the spacecraft, which is of great concern to satellite designers looking to cut propellant weight costs. Given accurate simulation tools, various design trades, such as pointing the thrust vector off-axis or using shielding to stop CEX ions from flowing back into the spacecraft, can be studied and optimized for mission success. This research will deal with resolving the first two issues – modeling the transient behavior of the potential downstream of the cathode and modeling the charge exchange process within the engine itself, as the creation of slow ions upstream in the acceleration region affects the shape of the plume in the far field.

Figure 1.2 shows a three dimensional picture of a Hall thruster mounted on a spacecraft firing as if it were performing North-South station keeping. The space potential lines are shown surrounding the thruster, as calculated by David Oh's plume simulation. The spacecraft is at a significantly negative potential relative to the engine. To avoid damaging the solar arrays, the engines are canted to the sides 45°. This results in a performance loss, which engineers would like to avoid. Understanding the structure, shape, and characteristics of the plume is important to minimize the losses associated with protecting the solar arrays and other spacecraft components.

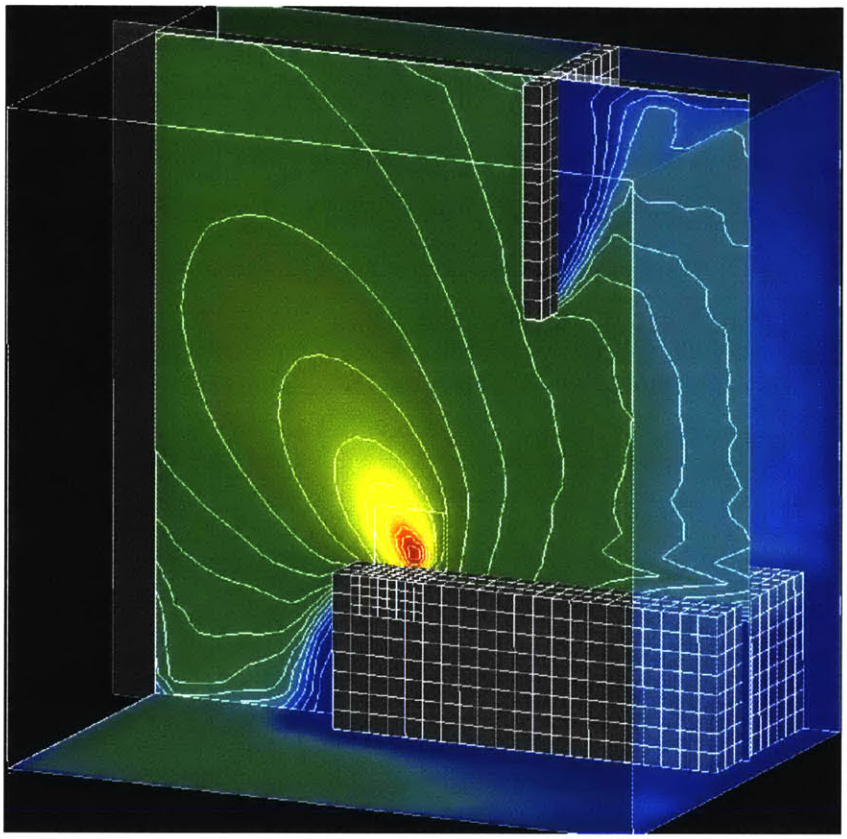

Figure 1.2: Hall thruster on a satellite: spacecraft-plume interactions.

Chapter 2: Hall Thruster Physics

There is a large body of research on plasma physics and Hall Thruster experiments. The following sections detail some of that research and the physical principles involved.

2.1 Plasmas

Plasmas are an ionized state of matter that occurs naturally at temperatures above 10,000°C. The resulting substance is an electrically charged fluid subject to the effects of electric and magnetic fields, and is thus fundamental to many electric propulsion applications. The interactions between the charged particles and any external or internal electric or magnetic fields are complicated and require new tools to understand them.

Plasmas can be found in many other processes in manufacturing and materials processing. Some important applications include plasma etching of silicon for microchips, gas discharge for lasers, killing bacteria in foods and other instruments, as well as space propulsion.

2.2 Hall Thruster History

As mentioned previously, research into the development of "Hall Effect Thrusters" began simultaneously in Russia and the U.S. in the 1960's. However, the current oscillations convinced the Americans to abandon the research until recently. The Russians, however, continued to develop the engines, gaining flight experience on 21 missions since 1971. Most recently, the Russians developed the SPT-100 (Stationary Plasma Thruster) and have flown it several times. This is the engine that has been adopted by the United States and passed qualification testing. The SPT-100 is planned for flights on Space Systems/Loral satellites to be launched in the near future.

Because of the high efficiency and optimum Isp of Hall Thrusters, there has been ever increasing interest in developing commercial applications of this technology. The U.S. Ballistic Missile Defense Organization is planning to use SPT's as part of its Russian Hall Effect Thruster Technology program.

The performance results in testing are encouraging, but as with any new technology, more understanding and experience is required before Hall Thrusters are extensively used. Research into the effects of the plume on the spacecraft will go a long way towards verifying the safety of the engines.

2.3 Basics of Thruster Operation

Hall thrusters, also called closed-drift thrusters, use electric power to create an electric field, acting much like a standard ion engine, but without a grid. A cathode injects electrons into the plume, some of which travel upstream, inside the engine and collide with Xenon neutrals. A picture of a Hall Thruster firing is shown in figure 2.1. The high-energy collisions inside the thruster knock more electrons free, creating Xenon ions and secondary electrons, which continue the ionization process. These Xenon ions accelerate in the presence of the electric field, imparting momentum to the engine, and thus creating thrust on the vehicle. A radial magnetic field is generated inside the engine to trap the electrons, as they move many times faster than the Xenon ions.

Figure 2.2 shows a schematic cross-section of a Hall thruster. The axial electric field and radial magnetic field are shown. The presence of the two fields causes electrons to travel in a circular motion about the centerline of the engine. The cyclotron frequency for ions is much higher than for electrons, so the magnetic field has a negligible effect on the ion motion.

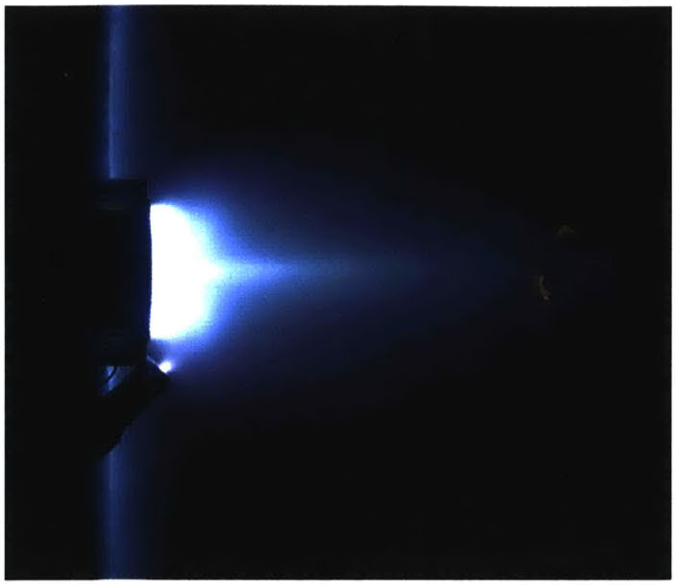

Figure 2.1: SPT-100 Hall Effect Thruster used in testing.

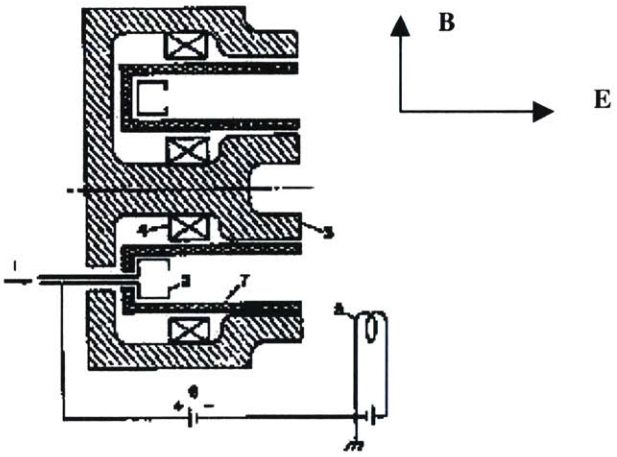

Figure 2.2: Cross-section schematic of an "SPT-100-like" thruster.

Xenon has an ideal atomic weight and low ionization energy, giving an optimum Isp of about 1600 seconds. As is true for most electric propulsion devices, thrust and efficiency are power limited. Current Hall Thrusters have been built with thrust levels between 3 mN and 2 N. Theoretically, a higher power source could provide more thrust, as there are no predictions of any upper bound on plasma development.

2.3.1 SPT-100

The most popular design in production now is the SPT-100, developed by the Russians, manufactured by Fakel, and qualified for flights on American spacecraft. This design has channel walls made of Boron Nitride, a dielectric material. Most test data comes from one of these engines, so it is the best understood and most readily used for future flights. Performance parameters are shown in Table 2.1:

Table 2.1: SPT-100 performance parameters.

Isp	1610 seconds
Thrust	84.9 mN
Discharge Voltage	300 V
Discharge Current	4.5 A
Power	1350 W
Efficiency	49.70%
Efficiency w/o Cathode	53.50%
Inner Insulator Diam.	56 mm
Outer Insulator Diam.	100 mm
Propellant	Xenon
Propellant Flow Rate	5.37 mg/s
Fraction of Prop. To Cathode	7.10%
Plume Electron Temp	2-4 eV
Axial ion velocity	17,000 m/s
Fraction of Prop Ionized	>95 %

2.3.2 Future Engine Designs

While the SPT-100 represents a simple design, modern engine research is focusing on developing more advanced engine technology. Some examples of these design modifications are:

- Thruster with Anode Layer (TAL)
- Scalable Hall thrusters
- Miniaturization of Hall thrusters
- Two-stage thrusters

The TAL engine operates much like the SPT engines; however, the acceleration chamber walls are made of conducting materials, whereas the SPT walls are insulators. The potential of the walls varies, and a sheath insulates the wall from the plasma. This reduces heat loss to the wall, resulting in thinner ionization layers and a shorter ionization chamber length. Similar performance can be achieved with a less massive engine. Additionally, the discharge is pushed mostly outside the engine, which reduces erosion. This improves engine lifetime and reduces the amount of sputtered material in the plume.

Different space missions require different sized engines, and rather than redesign a Hall thruster for each new customer, research is underway to develop an engine with adjustable linear components to expand the size of the engine while maintaining a similar design. These ovoid engines provide similar performance with the advantage of scalability to whatever mission is required.

Many space operations call for very fine thrusting maneuvers such as attitude control for pointing high gain antennas or maintaining formation flying for distributed satellites. Pulsed, low thrust engines are required to complete those missions. Miniaturized Hall thrusters could be potential candidates for high efficiency and high precision thrust maneuvers.

2.4 Hall Thruster Research

As previously stated, while performance data exist, good experimental data for the plume effects are hard to come by, as ground testing in a vacuum tank introduces serious uncertainty into the modeling of a Hall Thruster. Therefore, extensive computational work, as well as experimental, has been undertaken in academic, industry, and government laboratories.

2.4.1 Computational Hall Thruster Research

Many tools for modeling plasma flow have been developed over the years. The goal is to develop a methodology that is accurate with respect to experimental results, captures as many aspects of the physical behavior of the engine, and is computationally efficient enough to be used for design as well as analysis. Because the numerical methods themselves have been fully developed and tested before, only an overview will be presented. The techniques used most often are:

- Molecular Dynamics
- Particle-in-Cell
- Direct-Simulation-Monte-Carlo
- Hybrid Particle-in-Cell/Direct-Simulation-Monte-Carlo

A plume simulation code used at MIT, developed by David Oh, uses the Hybrid PIC-DSMC method to track particles, perform collisions, and analyze performance [Oh, 1997]. The detailed descriptions and relative merits of the above techniques can be found in Birdsall and Langdon [1991] and Lubachevsky [1991].

The most recent work, by VanGilder, Keidar, and Boyd [1999], uses an algorithm much like David Oh's, however the electron temperature is allowed to vary. In Oh's model, the electron temperature is a constant. The VanGilder, Keidar, and Boyd paper indicates that variable electron temperatures match experimental results better.

In addition to these far-field plume codes, J. Michael Fife developed an unsteady model of the operation within the acceleration zone of a Hall thruster. His code models the ionization process directly, tracking ions and neutrals as macro-particles according to the PIC method, while modeling electrons as a fluid, much like Oh's hybrid method. His electron fluid model goes into much more detail. Rather than assuming electron equilibrium like Van Gilder et al, Fife's code solves the continuity, momentum, and energy equations for the electron gas. Unlike Oh or VanGilder et al., Fife's code does

not model charge exchange collisions at all, arguing that in the near-field regions, collisionality is not important.

2.4.2 Experimental Work

Experimental research has been conducted using Hall Thrusters in Russia since the 1960's. These data were not understood in the United States until the 1990's though. Absalamov et al. [1992] was the first to publish results pertaining to the interactions associated with the far-plume. He measured the erosion rates and deposition on solar cell cover glass.

The work of the Russians was validated and extended in the United States by Myers and Manzella [1993]. This work took a closer look at the details of the plume, recording electron density, electron temperature, and ion current density. Other research has followed, observing the details of the plume, as well as measuring interactions between the plume and materials placed downstream at various angles.

Recent work, published in 1998 by Lyon King and Alec Gallimore at the University of Michigan has examined the ion distribution in the plume. Of particular interest is the energy level of ions found above 90° from the centerline axis. Figures 2.3 and 2.4 show their results.

At 0.5 meters from the engine exit, ions were found with a energy of more than 200 volts at up to 100° off the thrust axis. Ions with less energy were found at these locations one meter from the exit. This means that some ions are accelerating radially, through a potential drop near that for the engine. As these angles do not lie in the field of view for ions created inside the acceleration zone, some ions must be created near the exit of the engine. This seems to support the idea that CEX ions created at the exit experience near 200 V of potential drop. Current computational models do not accurately explain this phenomenon. [King, 1998]

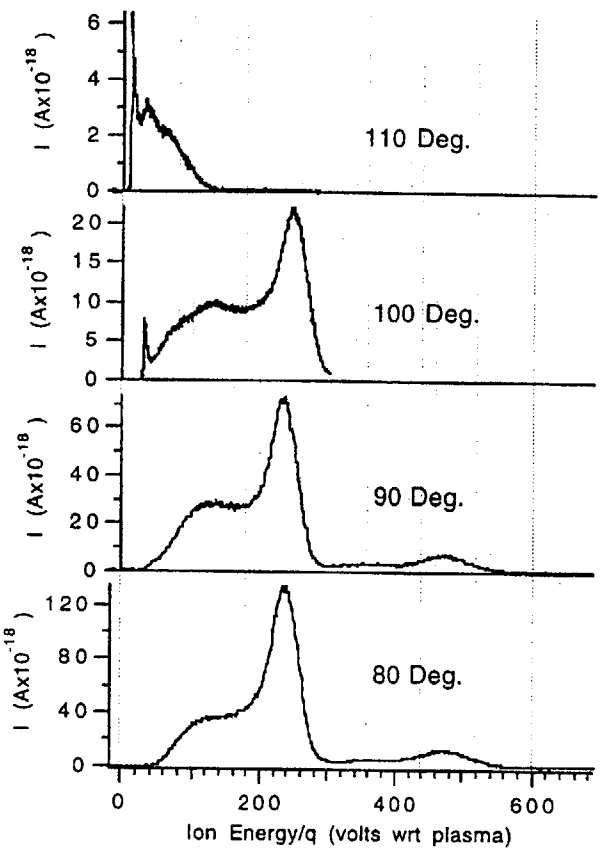

Figure 2.1:Ion current as a function of ion voltage at 0.5 m radius from the SPT-100 for points at 80, 90, 100, and 110 degrees off thrust axis [King, 1998]

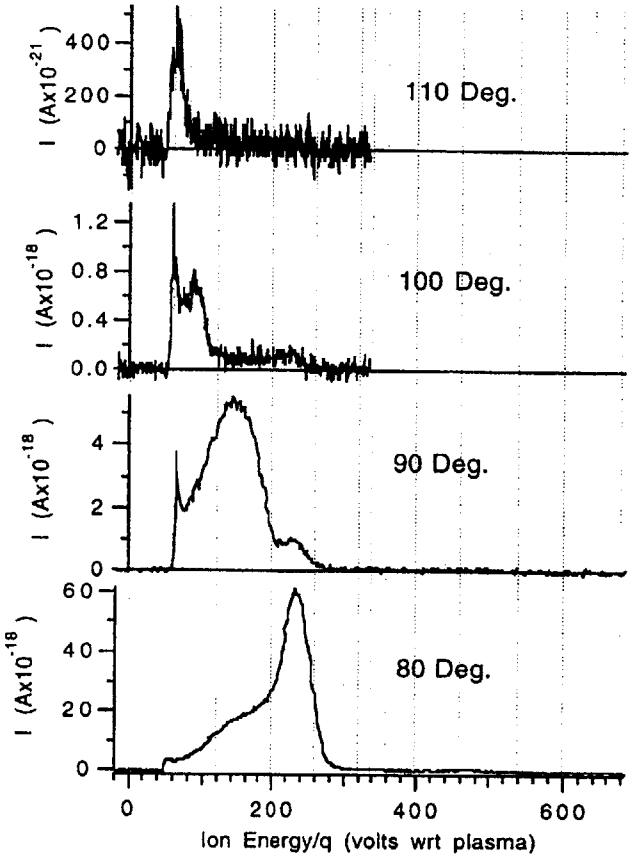

Figure 2.2: Ion current as a function of ion voltage at 1.0 m radius from the SPT-100 for points at 80, 90, 100, and 110 degrees off thrust axis [King, 1998]

The computational work has been able to model the experimental results with pretty good accuracy, although the recent push to develop this technology commercially is encouraging even better computational agreement in trying to understand the full physics of the Hall Thruster plume.

Chapter 3: Existing MIT Hall Thruster Plume Simulations

As part of an on-going effort to improve our understanding of the physics of Hall Thrusters and their interactions with the spacecraft and its environment, two main simulations of the engine have been developed at MIT. Several revisions and modifications have been made to the codes in order to improve their accuracy and capability, and modernized versions are currently being validated.

3.1 D. Oh's Plume Model

In 1997, David Oh completed his simulation of the Hall Thruster plume. He employed a hybrid PIC-DSMC computational method to track the particles in the plume as it evolves in time. The code does detailed collision analysis, probabilistically determining collisions and momentum transfers in the plume. The code tracks the charged particles, calculating potential in the plume. The original code can model some surface interactions in determining erosion rates for the lifetime of the spacecraft.

3.1.1 D. Oh's Assumptions

The code makes a few important simplifying assumptions. Among others, Oh assumed:

- Electron temperature is constant in the plume. Potential is calculated by inverting the Boltzmann equilibrium relationship
- The plume is quasi-neutral and steady
- There is no effect of any external magnetic field from the Earth or from the thruster
- Ion flux distribution at the engine exit plane is taken as given.

These assumptions are made in order to speed up computation time. However, the region in the grid where the plume is likely to come into contact with the spacecraft does not necessarily behave according to these assumptions.

Whereas a PIC method can model the long-range Coulomb forces present in the flow, a DSMC algorithm is necessary for modeling collisions. The effective cross-sectional collision area for different collision types varies depending on collision type. Coulomb collisions, between Xenon ions of various states are assumed to be elastic with relatively long mean-free-paths. The CEX collisions dominate and are the focus of the DSMC part of the simulation. The details of the collision model can be found in Oh's thesis [Oh, 1997].

3.1.2 Later Modifications of Oh's Code

Several modifications [Qarnain, 1998; Asare, 1999]have been made to the code increasing its accuracy and capability. The first set of changes involved the inputs from the engine itself. As the plume code does not model time dependent oscillations of the engine, its input values for densities, distribution, and angular variation is given by time-averaged results of other engine simulations. Connecting the time-averaged output of the engine simulation to the plume code input increased the accuracy of the model. An effort to automatically connect the output of Fife's code to the input of Oh's code has been examined but not completed to date.

Other modifications deal with plume-spacecraft interactions. Sputtering data for more materials has been added, as well as the capability to model the angular distribution of sputtered materials from a collision. Qarnain and Asare explain these modifications in more detail. [Qarnain, 1998; Asare, 1999]

3.1.3 Applicability

Oh's simulation ignores the operation of the engine itself, modeling the thruster only as a source of particles. This code is effective at examining plume effects on the scale of a spacecraft. The most powerful tool associated with the plume model is the ability to model interactions with objects in the plume region, such as solar panels, the spacecraft

bus, and vacuum tank walls. Oh's code has extensive capability to examine the issues of sputtering from the spacecraft surfaces and model component erosion rates.

3.2 Unsteady 2D Hybrid-PIC Simulation of a Hall Thruster

In 1998, John Michael Fife published his computational model that analyzes the performance inside the engine, using a more complex calculation method with fewer assumptions. He is able to model the time-dependent operation of an engine and track variations over the engine lifetime. His algorithm models the ionization process directly, whereas the Oh's plume code just adds a number of ions and number of neutrals each time step. The output is able to take a closer look at the phenomena occurring inside the acceleration zone and in the near field exhaust region.

3.2.1 Fife's Assumptions

In Fife's code, some electron characteristics are assumed constant along magnetic field lines and between lines they are subject to conservation of current. Specifically, Fife assumes the relationship between plasma potential and electron temperature in equation 3.1 to be constant along the magnetic field lines. Thus, for a pre-computed magnetic field, the potential and electron temperature can be updated based on changes in the ion number density.

$$\Phi - \frac{kT_e}{e}\ln(n_e) = \Phi^*(\lambda) \tag{3.1}$$

Like Oh's code, Fife assumes quasi-neutrality; however, the plasma is subject to the magnetic field in the computational domain. Oh's code ignores the magnetic field, as he is concerned with the plume region far away from the engine exit.

Thus Φ^* and the electron temperature are constant along field lines. Fife is able to model the time-dependent dynamics of the engine operation, including direct modeling of the

ionization process. Ions and neutrals are tracked as super-particles, while electrons obey fluid equations. Fife's code does not model CEX collisions, as they affect the plume characteristics in the far field. A more detailed explanation of the operation of the unsteady code can be found in Fife's thesis. [Fife 1998]

3.2.2 Later Modifications of Fife's Code

Prior to this research, the main modifications to the Hybrid-PIC code increased the number of possible geometries the simulation can model. Comparing the results to experimental data taken for those engine geometries further validated the accuracy of the simulation. [Szabo, Martinez-Sanchez, and Monheiser, 1998]

3.2.3 Applicability

Modeling the unsteady engine behavior allows for a more detailed and accurate calculation of the effects inside the engine. A time-averaged output of Fife's code is used for the initial conditions of Oh's plume code. Efforts to combine the two codes have been undertaken, but with little success due to the different algorithms used to track the particles. Namely, Oh does not model electrons at all, while Fife does calculate electron temperature and velocity. Oh's code merely inverts the Boltzmann equilibrium relation to calculate potential, rather than solving electron fluid equations..

For the purposes of understanding the engine operation processes that determine the plume shape, the Hybrid-PIC code offers the best solution. The existing model need only be further modified to continue its calculations into the plume region. The details of these modifications will be explained in Chapter 5.

3.2.4 Baseline Results

The following figures show the baseline results from Fife's simulation prior to any modifications to the grid or computational algorithm. The results in Chapter 7 should be referenced to the existing capability of the simulation.

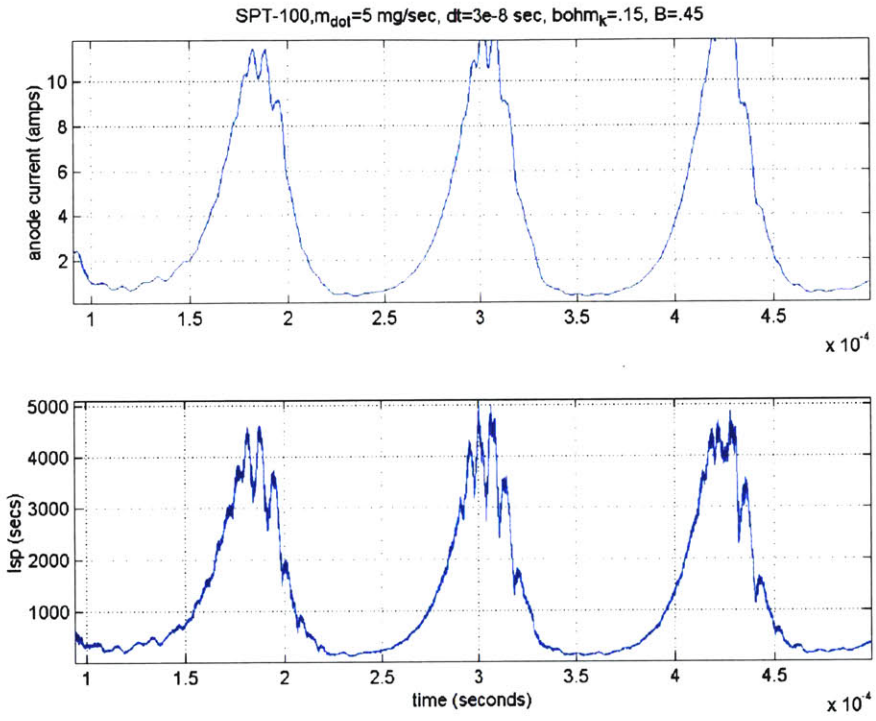

Figure 3.1: Anode current and Isp vs. time for the baseline simulation.

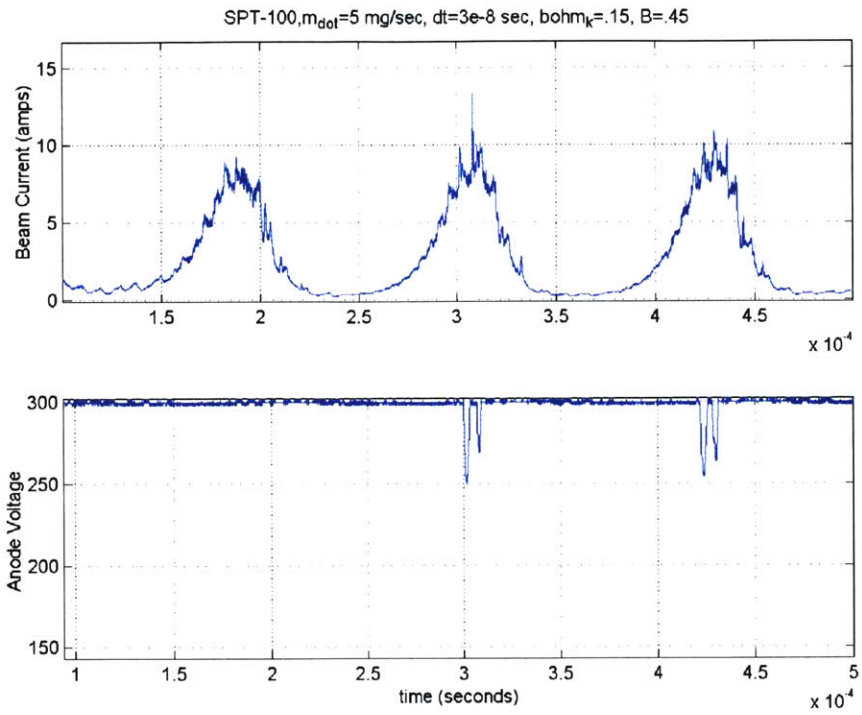

Figure 3.2: Beam current and anode voltage vs. time for baseline simulation.

The oscillations in current occur at about 9 kilohertz, lower than experimental results (20 kHz). The temperature, potential, and ion density plots are closer to experimental results.

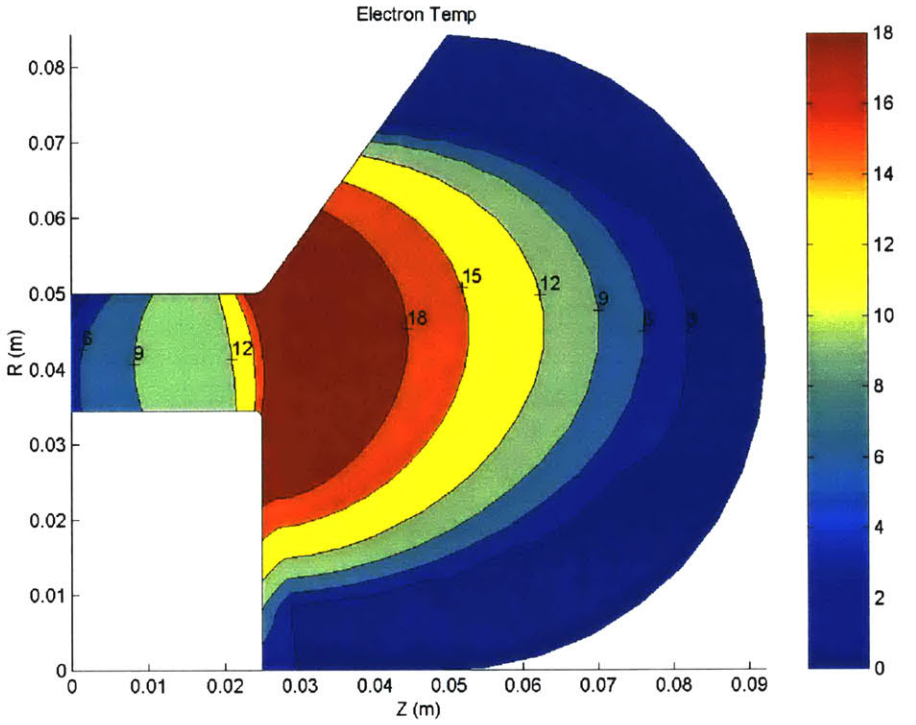

Figure 3.3: Electron temperature [eV], baseline.

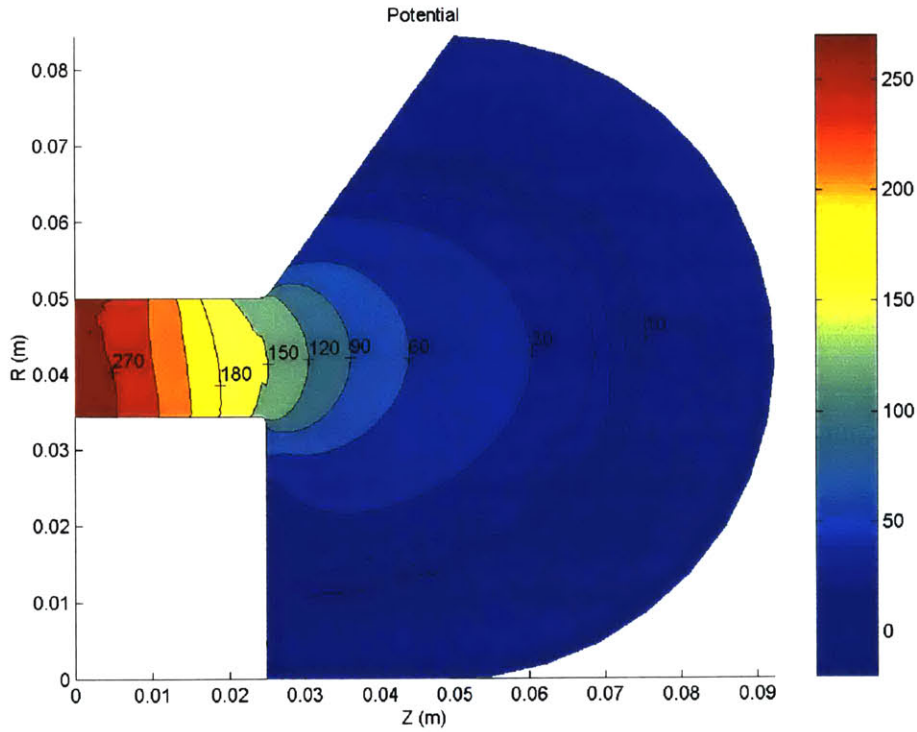

Figure 3.4: Potential [V], baseline.

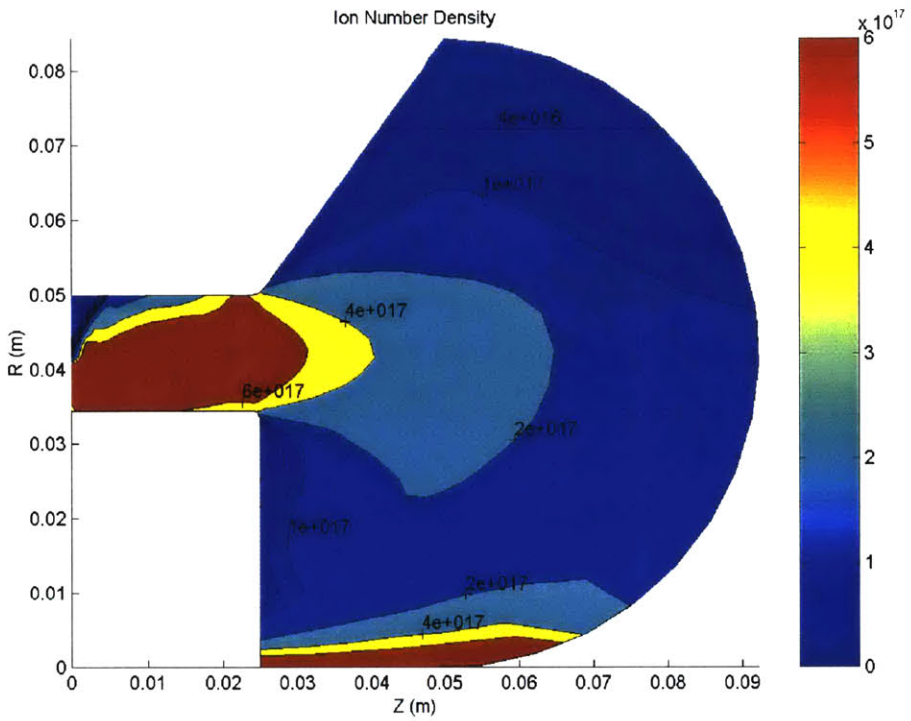

Figure 3.5: Ion density [m^{-3}], baseline.

3.3 Other Work at MIT

Still other one-dimensional analyses have begun to try to understand and model the oscillations in the plume. Noguchi developed a model based on linear perturbations of a steady-state solution. His results found modes of oscillation at frequencies higher than those observed in experimental work.

James Szabo is advancing the computational methods of Fife's code to directly model the electrons as particles, tracking them on a faster time-step. Recent advances in computational power allow such a simulation to run in a timely fashion. This research allows detailed modeling of the electron distribution function. Previous thruster simulations assume the electron distribution is Maxwellian; however, experimental research seems to indicate this may not be the case.

In addition to the computational research, an experiment to fly a small Hall thruster built by Busek Company on the Space Shuttle is being developed by Stephanie Thomas. Data from the on-orbit experiment will be used to correct for the problems experienced in ground tank testing due to ambient background pressure in Earth-based tank experiments.

Chapter 4: Physics in the Plume

Fife's code models the physics of the acceleration zone in a Hall thruster. Two significant differences between the acceleration zone and plume zone physics is the lack of net current and the dominance of charge exchange collisions.

4.1 Plume Current

In the acceleration region, a net current flows from the anode to the cathode. Some electrons emanating from the cathode travel upstream to initiate ionization, while the rest neutralize the plasma beam downstream of the cathode. To prevent the engine from charging, the current at the cathode and the current at the anode must be the same. At the anode, there is an ion current, an electron current, and current lost to the walls of the engine.

$$I_a = I_i + I_e + I_w \tag{4.1}$$

Beyond the cathode, there is no wall current and the ion and electron currents exactly balance to give a zero net current. The current conservation in the plume can be written

$$-2\pi e\int_0^l n_i u_{i,\hat{n}} r ds + 2\pi e\int_0^l n_e u_{e,\hat{n}} r ds = 0 \tag{4.2}$$

Fife derives expressions for the electron velocity in terms of electron mobility across magnetic field lines, $\mu_{e,\perp}$. By rewriting the derivatives of potential in the lab frame, those derivatives which are constant along lines of force can be pulled out of the integration. The details are included in Fife's thesis. He arrives at equation 4.3 for the electron velocity.

$$u_{e,\hat{n}} = \mu_{e,\perp}\left(-rB\frac{\partial\Phi^*}{\partial\lambda} - rB\frac{k}{e}(\ln(n_e)-1)\frac{\partial T_e}{\partial\lambda}\right) \tag{4.3}$$

Substituting equation 4.3 into 4.2 and solving for $\frac{\partial\Phi^*}{\partial\lambda}$ gives an equation for the change in potential functions across lines of force in the plume.

$$\frac{\partial \Phi^*}{\partial \lambda} = \frac{-2\pi k \frac{\partial T_e}{\partial \lambda} \int_0^l n_e \mu_{e,\perp} B(\ln(n_e) - 1) r^2 ds - 2\pi e \int_0^l n_i u_{i,\hat{n}} r ds}{2\pi e \int_0^l n_e \mu_{e,\perp} B r^2 ds} \tag{4.4}$$

Integrating equation 4.4 and using equation 3.1, the potential can be calculated everywhere on the grid as a function of λ. The temperature is calculated from the electron energy equation prior to computing the potential.

4.1.1 Boundary Conditions

In computing the temperature profile, boundary conditions are imposed at the cathode. In order to extend the calculations beyond the cathode into the plume where net current is zero, the cathode boundary conditions are applied, while plume boundary conditions are prescribed downstream. The change in calculations creates a discontinuity, as the current drops to zero over a single step. Smoothing in this area is required to ensure realistic results.

4.2 Collision Theory

Charge exchange collisions are subject to classical collision theory. The particles are large enough that classical theory is a pretty good estimate of the collision behavior, without using quantum mechanical methods. Charge exchange collisions occur between a neutral and an ion, either charged plus one or plus two.

Figure 4.1 shows a diagram of the collision process. There is a collision cross-section, beyond which incident particles do not collide. Within this cross-section, the particles will collide, and in the case of the charge exchange type, an electron will move from a neutral particle to the ion.

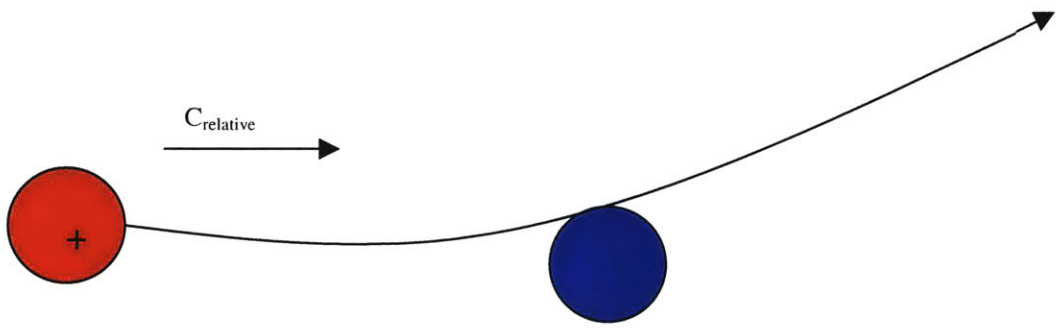

Figure 4.1: Diagram of 2 body classical collision

The likelihood of a collision is given by the collision rate. Equation 4.1 shows that this rate is a function of the cross-section for this type of collision, the number density of each of the colliders, and the relative velocity of the particles.

$$\dot{n}_{CEX} = n_i n_n c_{relative} \sigma_{CEX} \tag{4.1}$$

4.2.1 Collision Cross-Section

The cross-section, σ_{CEX}, is also a function of the relative velocity. In general, as the relative velocity increases, the chances two particles will exchange charge decreases. They are more likely to fly by at high speed. The relationship for the CEX cross-section was given by Oh in his simulation from curve fits to experimental data by Rapp and Francis [1962] and Hasted [1964] for single and double charged Xenon, respectively. These are given in equations 4.2 and 4.3, and plotted in figure 4.2. In the case of Xe^{++}, two electrons are transferred.

$$\sigma_{CEX+} = (15.1262 - 0.8821 \ln(c_{relative}))^2 \cdot 10^{-20} m^2 \tag{4.2}$$

$$\sigma_{CEX++} = \left(3.4069 \cdot 10^{-9} - 2.7038 \cdot 10^{-10} \ln(c_{relative})\right)^2 m^2 \tag{4.3}$$

As seen in figure 4.2, the cross-section for collisions with double charged Xenon is higher than that of single charged, but the number density of Xe^{+} is much greater than Xe^{++}, so the collision rate for Xe^{+} dominates. The collision rate is plotted in figure 4.3.

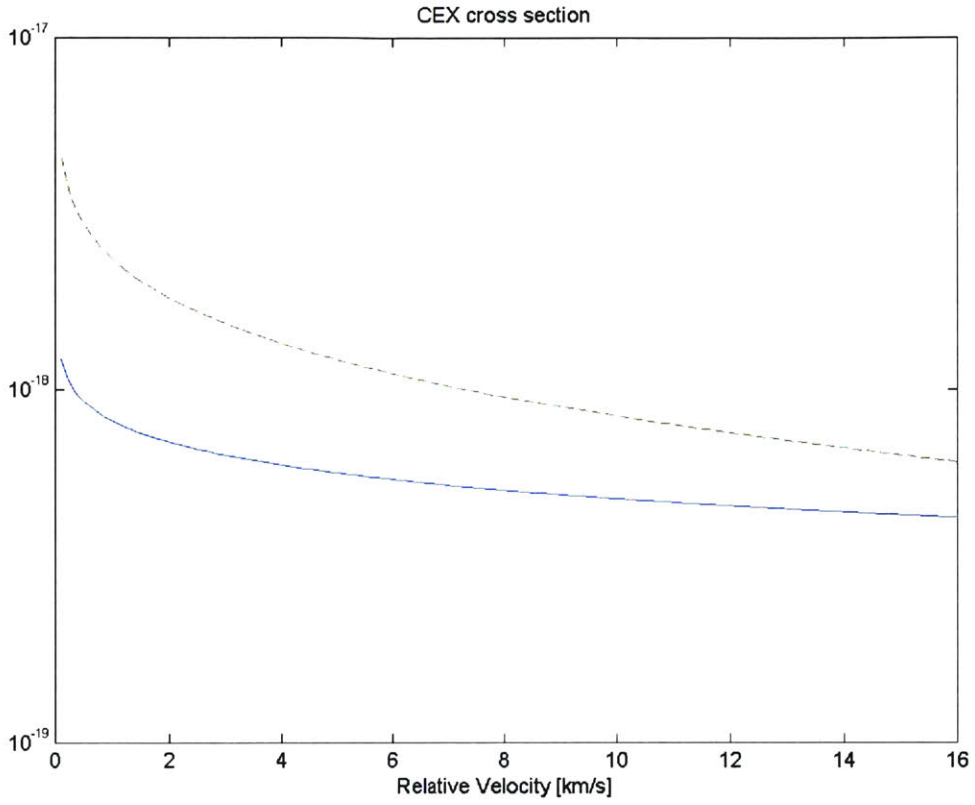

Figure 4.1: CEX Cross-section [m^2]. Solid line: Xe^{+}. Dotted line: Xe^{++} (double electron transfer).

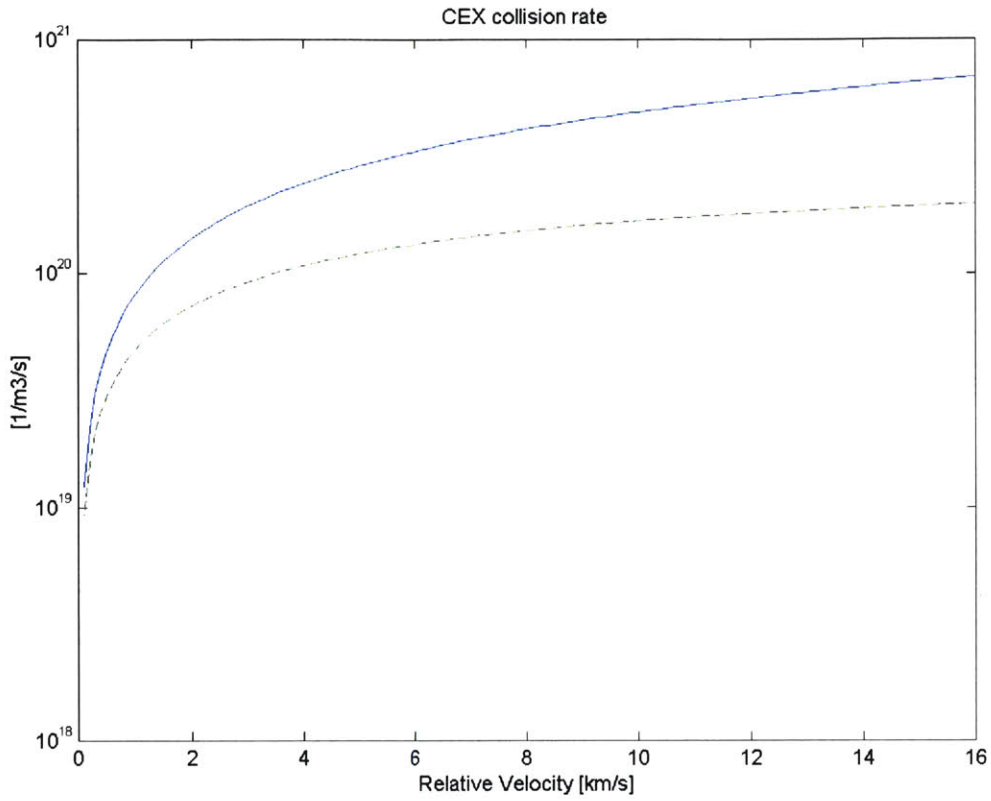

Figure 4.2: CEX collision rate: Solid line: Xe^{+}. Dotted line: Xe^{++}

In figure 4.3, a neutral density of $1x10^{18}$ and a Xe^{+} density of $1x10^{17}$ is assumed. The density of double-charged Xenon is 20% of single charged Xenon.

In this research, only Xe^{+} is considered. Other versions of the Hybrid-PIC code include double-charged ions, and implementing the procedure for CEX collisions with both ion types would be straightforward.

4.2.2 Particle Number Density

Figures 4.2-4.3 assume only a local value for ion and neutral number density, which is not an accurate picture of overall Hall thruster operation. The higher relative velocities are found in those regions where the ion and neutral number densities are smaller – in the plume. The neutral density in particular falls off by an order of magnitude by the time the flow leaves the acceleration zone. The ion density fluctuates according to the

ionization rates and temperature profiles. The inverse relationship between velocity and cross-section means the total rate is more sensitive to changes in number density than relative speed. To better understand the process of creating charge exchange ions, it is useful to look at one-dimensional data from the centerline of the annulus of an engine.

4.3 One-Dimensional Results

Data from Fife's thesis is used to estimate the collision rate for charge exchange events in the acceleration zone of an SPT-70, a smaller version of the SPT-100. Fife compared his computational results with test data and found the simulation to be an accurate model of the ion and neutral number densities within the plume.

4.3.1 Relative Velocity

The relative velocity of an ion-neutral pair is calculated assuming the neutral has zero velocity compared to the ion. The ion's velocity is a function of potential drop from the anode, which is related to the axial position in the engine. Again, Fife's data provided the potential profile. For simplicity's sake, the ions are created at the anode, subject to all 300 volts of possible acceleration. This is not a very accurate assumption, as many ions are created downstream and may only accelerate to some fraction of the full potential drop. However, to illustrate the trends in the acceleration zone, this is adequate. Equation 4.4 shows the relationship between ion velocity and potential.

$$c_{realtive} = \sqrt{\frac{2e(300-\Phi)}{m_{ion}}} \tag{4.4}$$

4.3.2 Number Density Data

Results published in Fife's thesis are used to generate the data for ion and neutral number density, as well as potential, Φ. Data is read from the centerline of the upper annulus of

the engine. The potenial is used to calculate relative velocity as in equation 4.4. The relative velocity is then used to estimate the collision cross-section.

Figure 4.4 shows plots of the data from Fife's code taken from the centerline of the annulus within the acceleration zone. The computation extends some distance into the near-field plume. At the end of the acceleration zone, the ions are assumed to travel at constant velocity, while the density contiues to decrease. By the end of the acceleration zone, near 0.04 meters, the neutral and ion densities have dropped by an order of magnitude. (X = 0 corresponds to the anode, inside the acceleration zone.)

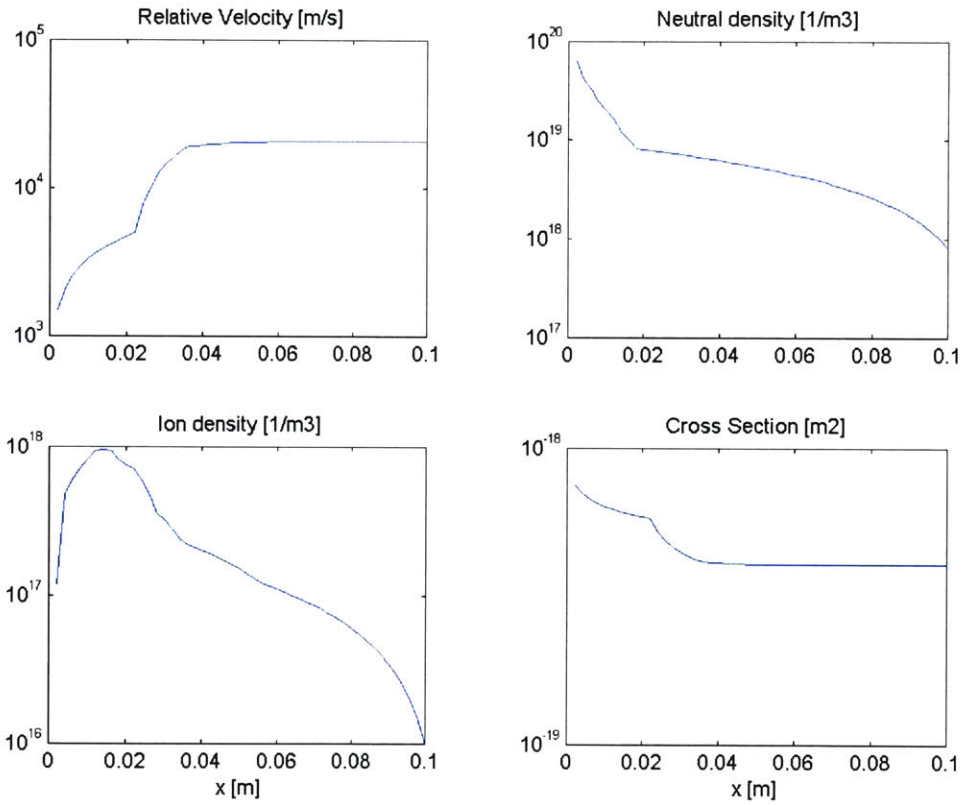

Figure 4.1: Exhaust flow data from simulation of SPT-70. Engine exit plane at x =0.04m.

4.3.3 Charge Exchange Rate

Even though the relative velocity increases and the cross-section remains fairly constant, the total ionization rate decreases in the plume. This is shown in figure 4.5. The peak lies inside the acceleration zone, where the ion density is the highest.

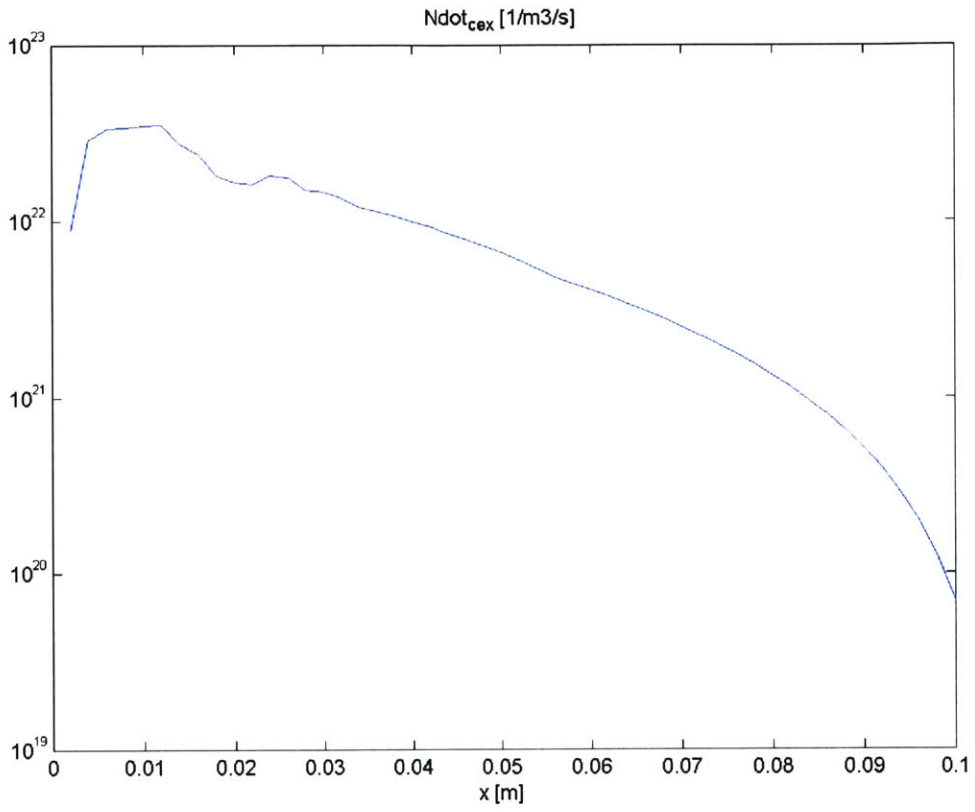

Figure 4.1: One-dimensional averaged charge exchange collision rate. Engine exit plane at x =0.04m.

It is clear from this example that the rate of CEX collisions falls off by two orders of magnitude by the time the ions enter the plume 6cm from the engine exit plane (at X=0.04m). It is therefore important to model the exchange process as part of the engine operation. The location within the acceleration chamber where the collision takes place is important, as those that collide early will accelerate and travel too fast to be drawn back into the vehicle. Those that collide in the exit plane of the engine will not undergo much more acceleration and will pose a potential risk to the spacecraft.

4.3.4 Comparison to Ionization Rate

Ionization could occur in the near-field plume region as well. To compare the relative rates of CEX collisions and ionization events, the one-dimensional analysis was repeated for the ionization process. Ionization from Xe to Xe^+ is modeled by the following equations:

$$\dot{n}_i = n_e n_n Q \beta_1 \frac{I(\Theta)}{\Theta^{3/2}} \tag{4.5}$$

where

$$I(\Theta) = \int_1^\infty e^{-\frac{u}{\Theta}} \frac{(u-1)}{u} \ln(1.25\beta_2 u) du \tag{4.6}$$

In these equations, u is the ratio of energy to ionization energy and is integrated over all possible energies. For Xenon, to fit the data, the threshold energy, ε_i, used is 21.2eV. Θ is the ratio of thermal energy to ionization energy, $\frac{kT_e}{\varepsilon_i}$, and Q, β_1, and β_2 are given as constants to fit experimental data according to the Drawin ionization model with Maxwellian electrons. For Xenon, Q is 4.13×10^{-13}, β_1 is 1.00 and β_2 is 0.80.

Figure 4.6 shows a plot of one-dimensional averaged ionization rate and charge exchange rate from a slice of data from Fife's SPT-70 simulation. Inside the acceleration zone, ionization is much higher than charge exchange; however, as the temperature falls off in the plume, CEX collisions dominate the ion production methods. Ions created at the thruster exit are equally likely to products of ionization or of a CEX collision. A short distance downstream, nearly all the ions created are the result of charge exchange.

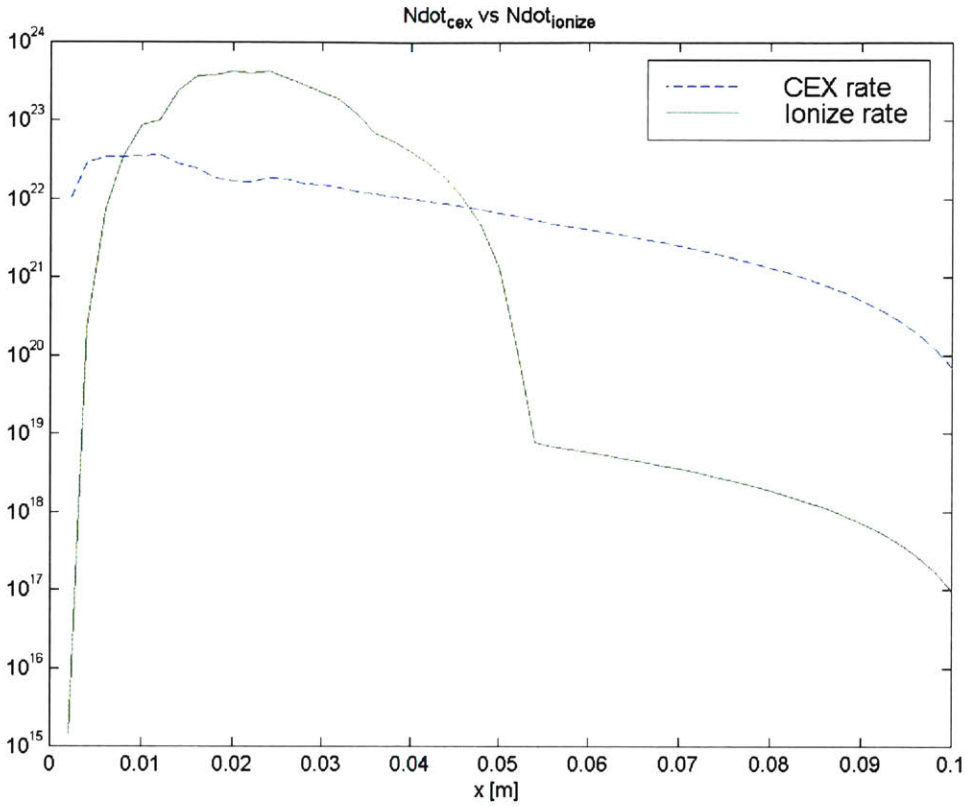

Figure 4.1: Comparison between charge exchange rate and ionization rate in thruster. Engine exit plane at x =0.04m.

The kink in the ionization data is a result of interpolating points in the plume region of Fife's original data. However, the ionization rate falls sharply as the temperature drops outside the engine, whereas the charge exchange rate decreases more slowly.

This one-dimensional model does not include possible changes to the potential distribution in the channel or plume. As charge exchange collisions take place, the distribution of ions will change, thus altering the electric fields and the potential. It is necessary to incorporate the CEX collision process into Fife's model to understand these changes.

While David Oh's simulation tracks collisions in the far-field plume, many more occur in the acceleration zone and should be modeled there as well. The following sections

describe an effort to directly model charge exchange collisions as part of Fife's unsteady hybrid-PIC simulation.

Chapter 5: Computational Methods

Michael Fife's two-dimensional simulation of a Hall thruster (SPT-70, SPT-100) was validated with experimental data and has since been used to estimate the performance of other Hall thruster geometries [Szabo, 1998]. Due to the historical accuracy of this software package, it will be used to examine the plume region and study the phenomena occurring there. Several modifications to Fife's code allow a detailed examination of the plume:

- Expand computational grid downstream – adds nodes, increases computational time
- Extend magnetic field calculations – pre-computed magnetic field lines are used to compute electron fluid equations
- Add charge-exchange collisions to the reactions taking place

There are several implications to each of the above changes, which will be explained in more detail for each modification. Chapter 6 will explain the changes to the geometry and the computational domain. The following sections detail the computational modifications themselves.

5.1 Magnetic Field Extension

The magnetic field is computed prior to any geometry change. The magnetic field solution is specific to the placement and strength of magnetic poles in the geometry of the thruster. For ease of calculation, the poles are assumed to be infinitely permeable. Laplace's equation is then solved in the specified regions about the poles. Once the grid geometry is specified, the magnetic field is converted to grid coordinates. Figure 5.1 shows the magnetic field solution for the upper side of a two-dimensional slice of the SPT-100. The potential lines are drawn; the field lines are perpendicular to the potential lines.

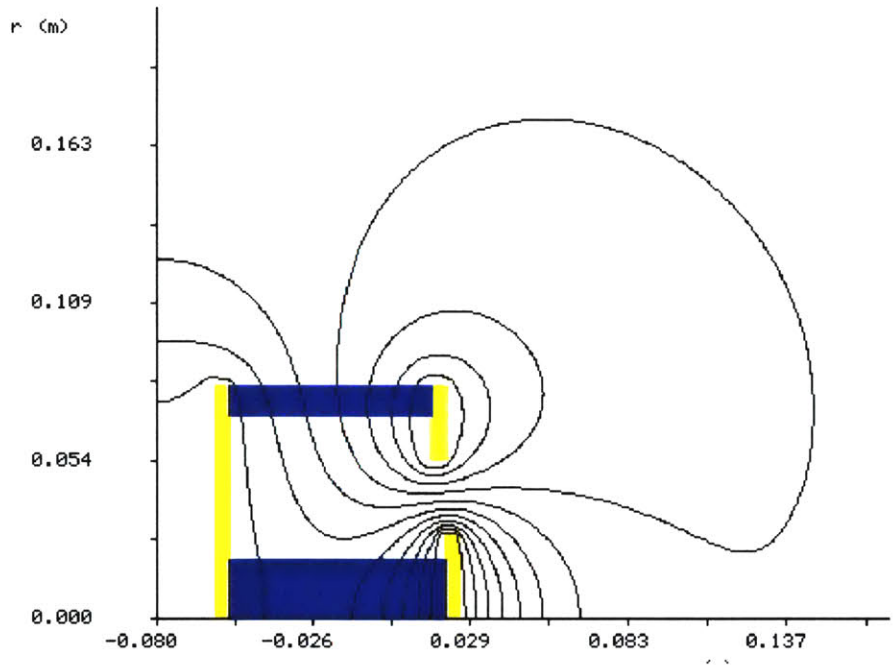

Figure 5.1: Magnetic field potential lines for SPT-100.

In order to solve Laplace's equation, the poles are assumed to be perfect solenoids, reducing the problem to that of potential flow. The magnetic stream function, lambda, can then be calculated. The stream function is used to compute values of electron temperature and space potential, which remain constant on streamlines.

The lambda values for the stream function are shown in figure 5.2. These values, where constant, create the integration paths for the module that calculates electron temperature and potential at locations in the grid.

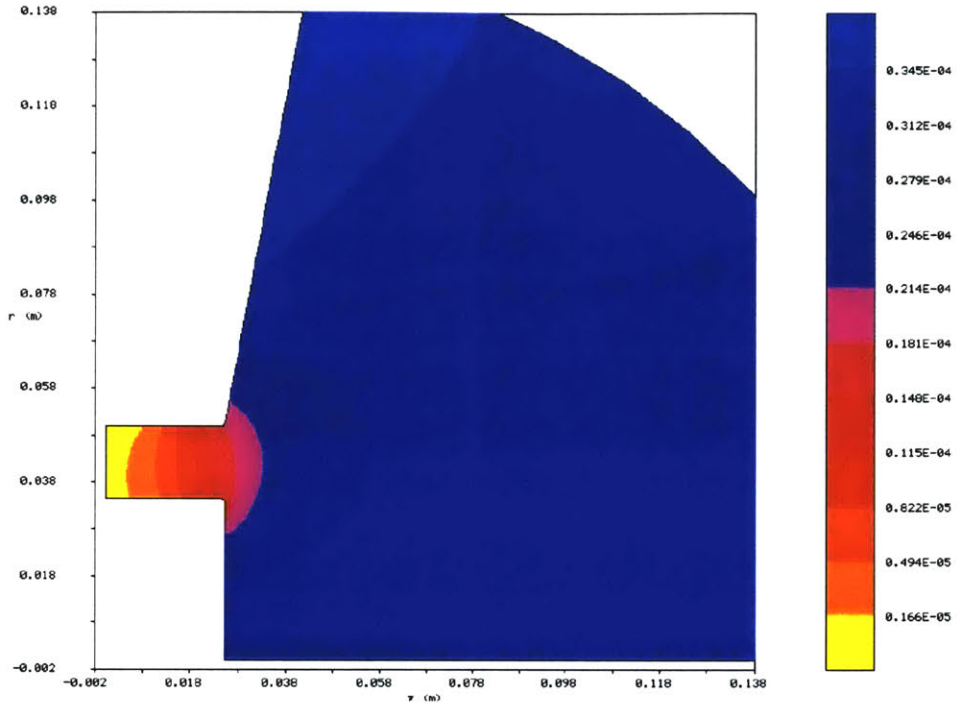

Figure 5.2: "Lambda," the magnetic stream function plotted for SPT-100 simulation. Cathode at r=0.07m.

5.1.1 Magnetic Field Strength

In the domain of a Hall thruster operating on a spacecraft, the magnetic field from the engine will dominate the field structure near the engine exit. However, as the flow expands into the plume region, other magnetic fields begin to dominate the magnetic field from the engine.

In his simulation, David Oh assumed there was no appreciable magnetic field, ignoring effects of the Earth's magnetic field, arguing that it is small enough to not affect the structure of the plume. Additionally, he assumed a constant electron temperature of 2 eV in the plume. By just extending the magnetic field solution in Fife's code, the temperature is allowed to vary in the plume, while the magnitude of the magnetic field drops off, providing a reasonable simulation of the magnetic field in the plume. Figure 5.3 shows the vector plot of the field lines in an SPT-100 geometry. The magnitude of

the field, shown by the proximity of vectors, falls off away from the exit of the acceleration zone in the engine.

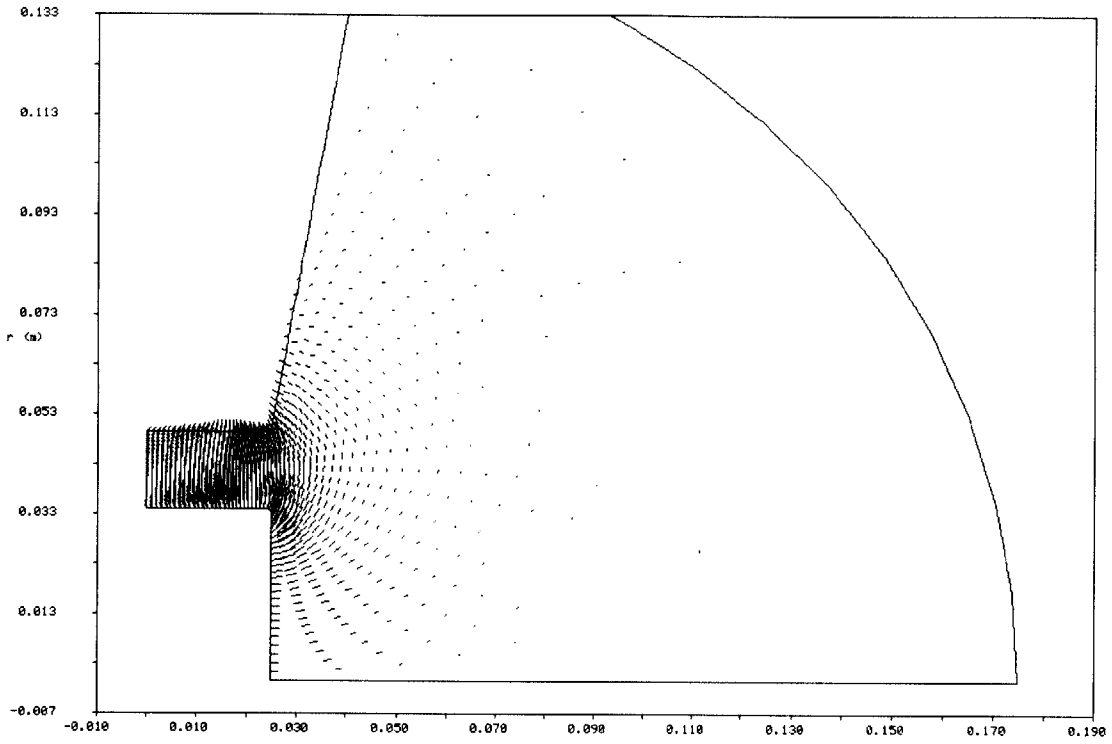

Figure 5.1: Vector plot of magnetic field lines in the SPT-100.

The coils set up a magnetic field to trap electrons flying from the cathode to the upstream anode. A radial magnetic field, in addition to the axial electric field, will create the Hall current as the electrons drift azimuthally. Figure 5.4 shows a close up of the field lines inside the acceleration zones. These lines, clearly radial, capture electrons while allowing the ions to fly through unhindered.

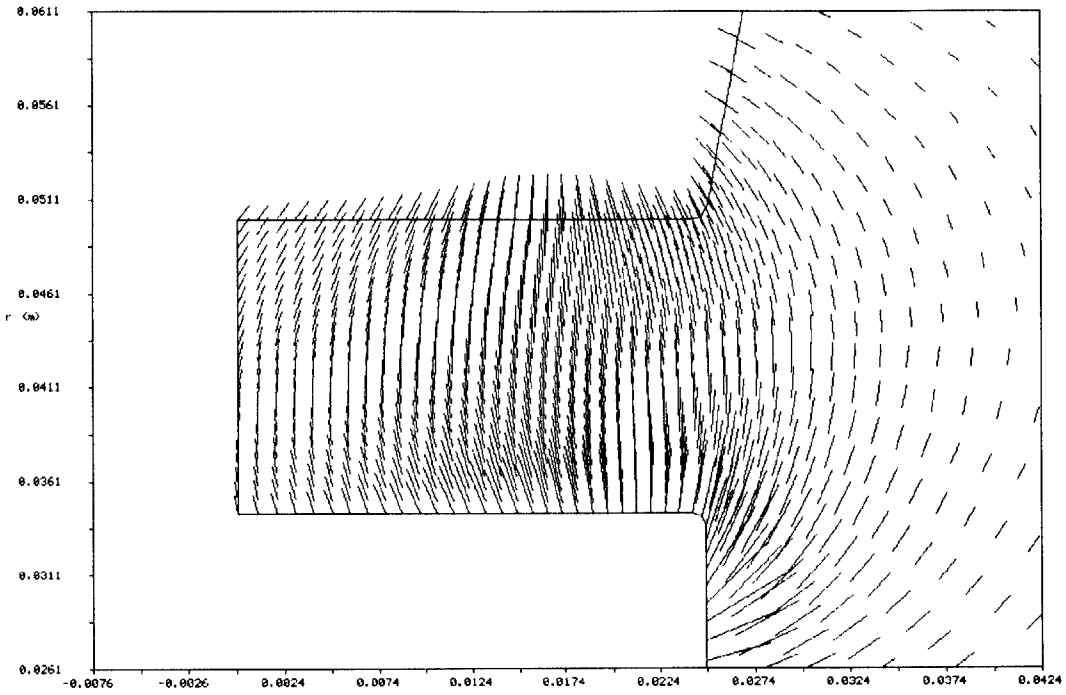

Figure 5.2: Vector plot of magnetic field lines in SPT-100 acceleration zone.

One can look at the actual strength of the magnetic field to find the limit where the assumption that electrons are trapped by field lines from the engine breaks down. When the Earth's geomagnetic field and the engine's field are of the same strength, it becomes more difficult to model the electrons in the plume. The assumptions about electron properties that change across lines and remain constant along lines is no longer valid, as those lines become mixed with the field lines from Earth. The Earth's field lines change with time throughout the orbit, and are difficult to model in a transient way. Figure 5.5 shows that the field strength drops to about 5×10^{-5} Tesla, approximately the value for the Earth's field, at the border of the current simulation domain. Extension beyond this point would violate the assumptions that electrons are trapped by field lines generated by the engine.

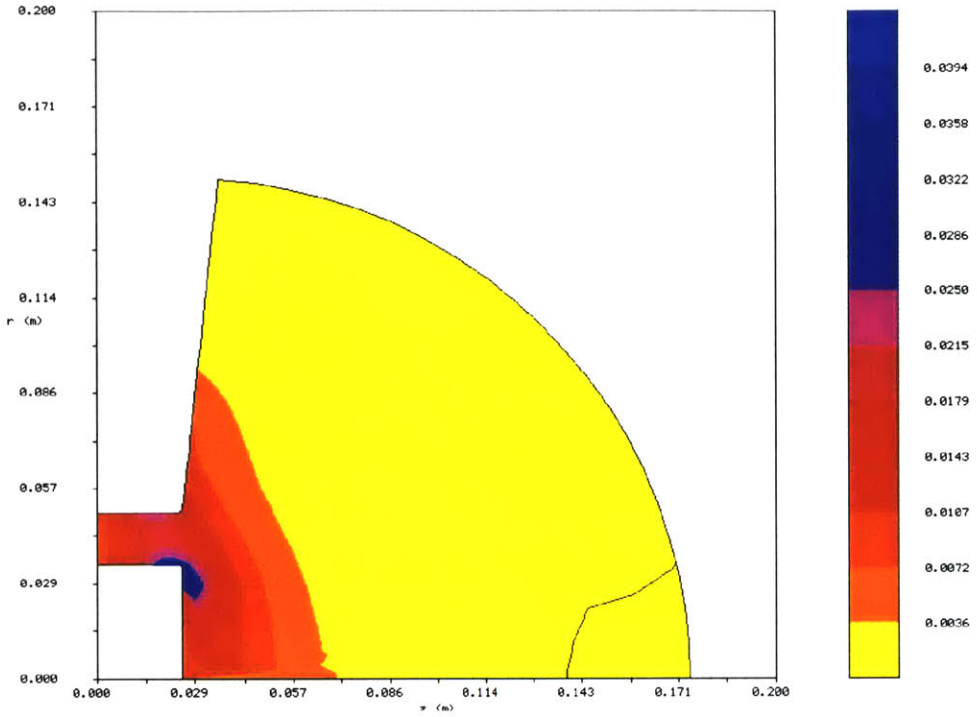

Figure 5.3: Magnetic field strength. The final contour corresponds to $5x10^{-5}$.

5.2 Electron Equation Assumptions

In Fife's original simulation, the current is conserved across magnetic stream lines. Some of the current from the cathode flows upstream to ionize the propellant, while the rest neutralizes the beam. The cathode is modeled as an "effective cathode" represented by a surface generated by rotation of the magnetic field line that intersects the actual cathode. Beyond the cathode, ϕ^* and T_e are constant, and potential is a function of ion density.

As discussed in section 4.1, there is a more accurate way to calculate the potential distribution in the plume. Rather than assume a linear drop in potential beyond the cathode, the electron equations can be solved assuming zero net current in the plume. ϕ^* is a function of λ only; when λ increases beyond the cathode value, the net current will be set to zero. The cathode value of λ can be computed by the code, where it is taken as the

minimum value of λ that intersects the right hand side plume boundary. Otherwise, an input value corresponding to the streamline that intersects the physical cathode can be used. The lines intersecting the right hand side boundary can be seen in figure 5.2. Using the this minimum value of lambda, the cathode is placed at a radial location of about 0.07 m from the centerline of the engine.

Figures 5.5 and 5.6 show the electron temperature and potential distributions in the engine. The distributions are consistent with Fife's results upstream of the cathode. In the figures below, the cathode is placed very near the exit of the acceleration zone where the temperature contours converge, about 0.07 m from the centerline.

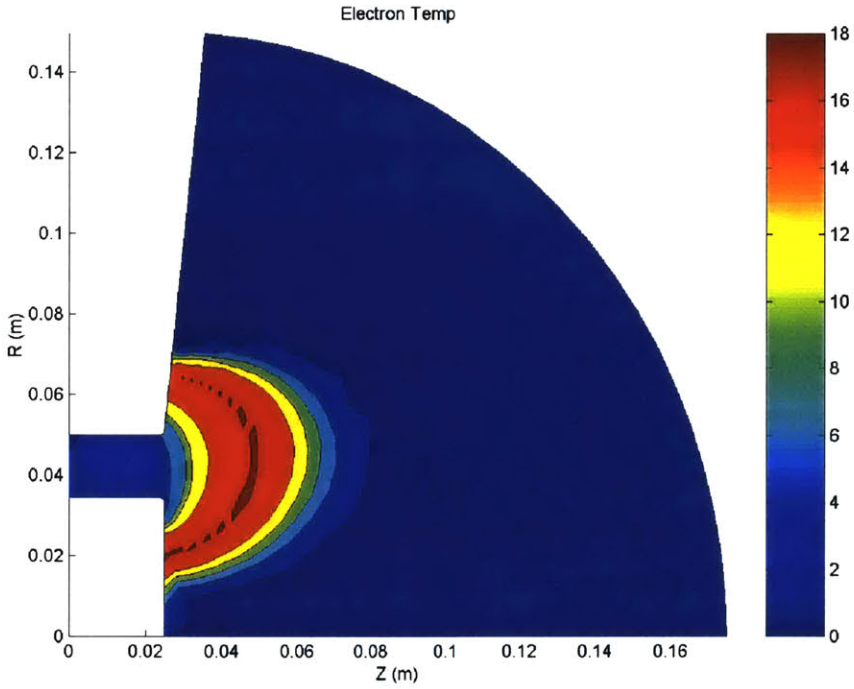

Figure 5.1: Electron temperature, assuming zero net current in the plume. Cathode at r=0.07m.

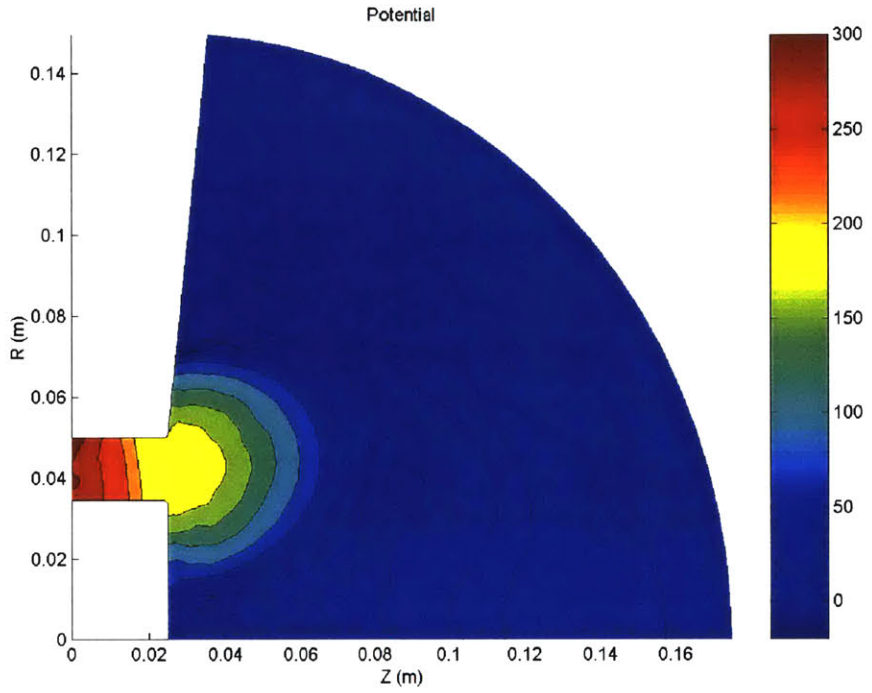

Figure 5.2: Space potential, assuming zero net current in the plume. Cathode at r=0.07m.

5.2.1 Discussion

The calculations become unstable after about 500 iterations; the anode current will either increase to the point where the code responds by decreasing the anode voltage below zero, or the current will become negative and be unable to recover. 500 iterations is long enough for several ion flow times, but not long enough to study any oscillatory behavior. Attempts to adjust the boundary conditions and smooth out the discontinuity at the cathode were unable to correct this problem. It is hypothesized that the connection between the potential distribution and regulation of the "power supply" prevents stable operations. The anode current, a measure of the net current, falls below zero with no natural mechanism to increase it. The "power supply" regulator responds by increasing the anode voltage applied, but this is unable to stabilize operation.

5.2.2 Recommendations

Because there are only about 10-12 cm between the region bound by the cathode and the downstream point where the field strength is small enough that the assumptions about electron mobility break down, it may not be important to model the current in the plume with this computational algorithm. The plume region just beyond the cathode is important; ionization and charge exchange collisions, which occur outside the acceleration chamber, happen most often in the near-plume regime. However, the potential and temperature distributions can be modeled with enough accuracy using Fife's current methodology.

An extension of Fife's simulation is not able to model the far-field plume any more accurately than other methods. However, it still provides insight into the unsteady behavior in the plume, as well as an understanding of the CEX process in the near-field, where the preponderance of collisions occur.

5.3 Charge Exchange Collisions

David Oh uses Direct-Simulation Monte Carlo methods to compute the probabilities for particle collisions. When a charge exchange collision occurs, one or more electrons will jump from one particle to the other. Effectively, the slow neutral is ionized and the fast ion is neutralized. Computationally speaking, this is the same as the slow neutral speeding up and the fast ion slowing down. Rather than swap charge, it is more computationally efficient to swap velocities, as less information per collision is transferred [Oh, 1997].

Due to the method of data storage in Fife's code, it is difficult to search particles based on location. The particles are stored in a linked list. Part of the data stored with each particle is a pointer to the next one in the list. If a particle leaves the simulation, it is deleted from the list. The previous particle will then point to the following particle. Any

time a particle is added, during ionization for example, the data are added to the beginning of the linked list. Therefore, the list is not sorted by location in the grid, although each particle has its grid location stored with it. It is therefore more efficient to loop through all the particles directly. For the purposes of ionization, this presents no problem because the second body in the collision, the electron, is modeled as a distribution. Each neutral is ionized independent of any other particle in the simulation at that time.

The process would be more complicated for a two-body charge CEX collision. Therefore, a similar approach to the ionization process is taken. Looping through the entire list of ions, the probability of collision for each ion in the list is computed based on the local CEX collision rate. This probability is compared to a random number to determine whether or not a collision took place. If so, the ion reverts to the average neutral velocity for that grid cell, simulating the fact that in reality, a slow neutral would have been ionized.

Neutrals can be likewise sped up, given the average ion velocity for their local cell. However, in order to maintain the proper number of neutral macro-particles in the simulation, the neutrals are left alone. To achieve computational efficiency, there are fewer, but more massive, neutral particles in the simulation. Thus, for each CEX collision, only a fraction of a neutral particle would change velocity. Implementing this computationally is difficult, and tracking the fast neutrals is not as interesting as tracking the ions.

5.3.1 Ionization vs. Charge Exchange Collision Rates

In order to track the particles, ions "created" through charge exchange are marked differently than those created through ionization. The location and energy for each type of ion can be recorded as it leaves the simulation. Figure 4.6 in section 4.3.4 showed the relative rates of collision for ionization and charge exchange in one dimension. Using Fife's code, the relative rates can be computed for the two-dimensional simulation.

Figure 5.8 shows that ionization dominates the region just outside the acceleration zone. However, as the temperature drops off, ionization becomes almost non-existent. Figure 5.9 shows the charge exchange rate plotted on the same scale. A few centimeters downstream, CEX dominates.

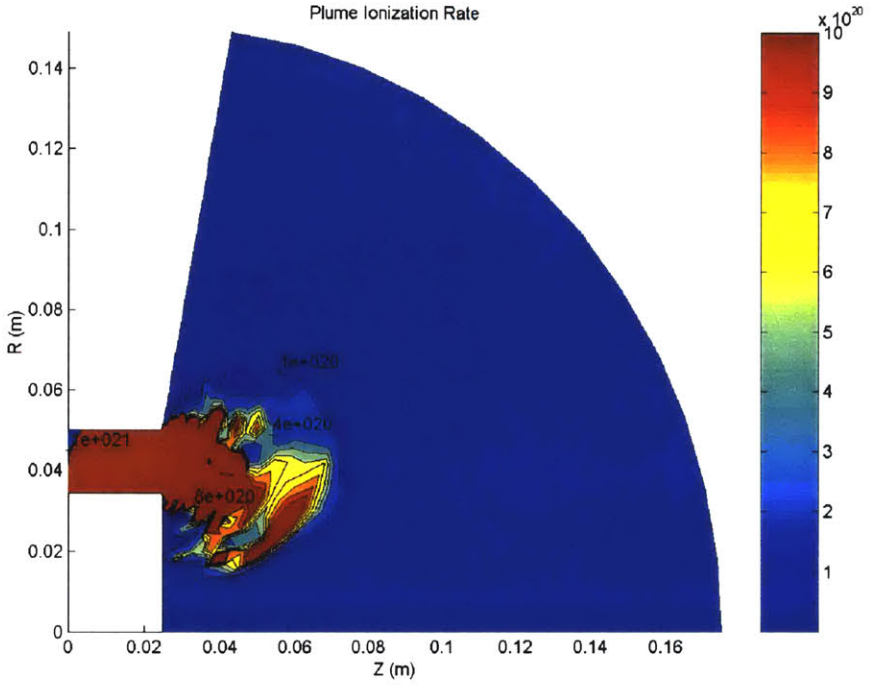

Figure 5.1: Ionization rate in the plume. [$m^{-3}s^{-1}$]

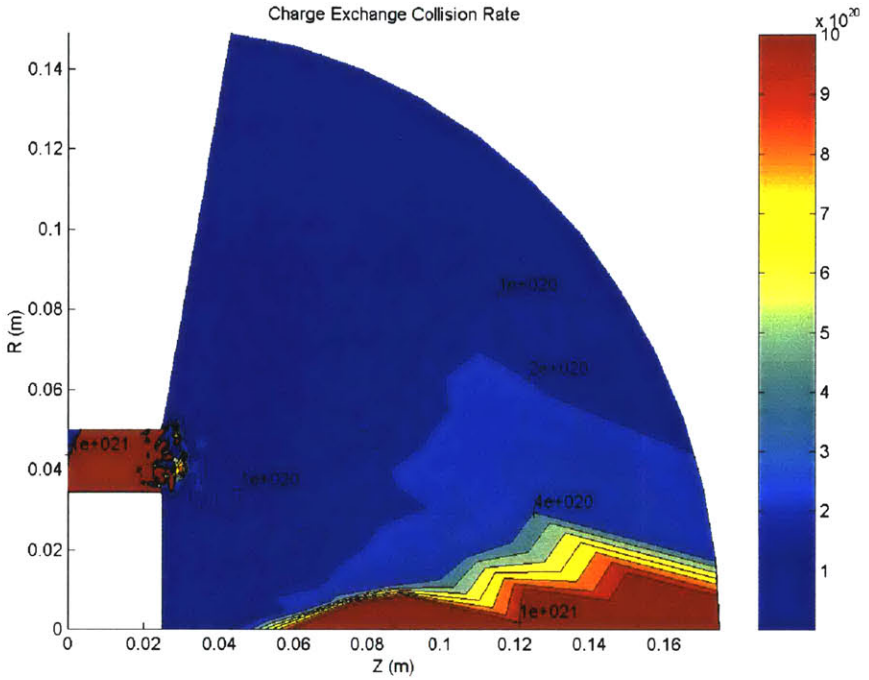

Figure 5.2: Charge exchange rate in the plume. [$m^{-3}s^{-1}$]

The ions found at angles greater than 90° off axis and behind the thruster could result from ionization collisions rather than CEX. Modeling ionization in a plume simulation is also important. Oh's model ignores ionization collisions (and other Coulomb collisions, as well) in order to speed up computation. In running the simulation, ions created from ionization and charge exchange can be tracked to find out where they leave the simulation. The distribution of ion velocities and energies leaving the simulation are shown in the results.

Chapter 6: Geometry

Due to its popularity among researchers, the SPT-100 was chosen for this research. Comparisons to prior research and existing flight hardware would be possible. Section 2.3 discussed the performance characteristics of an operational SPT-100 and showed a photo and schematic of the engine. The following sections will describe the geometry of the hardware, as well as the grid generation process for the computational geometry. The Hybrid-PIC code is capable of solving almost any Hall thruster geometry.

6.1 Hardware

Figure 6.1 shows a laboratory test model from the University of Michigan, while figure 6.2 shows a diagram illustrating the dimensions of the geometry.

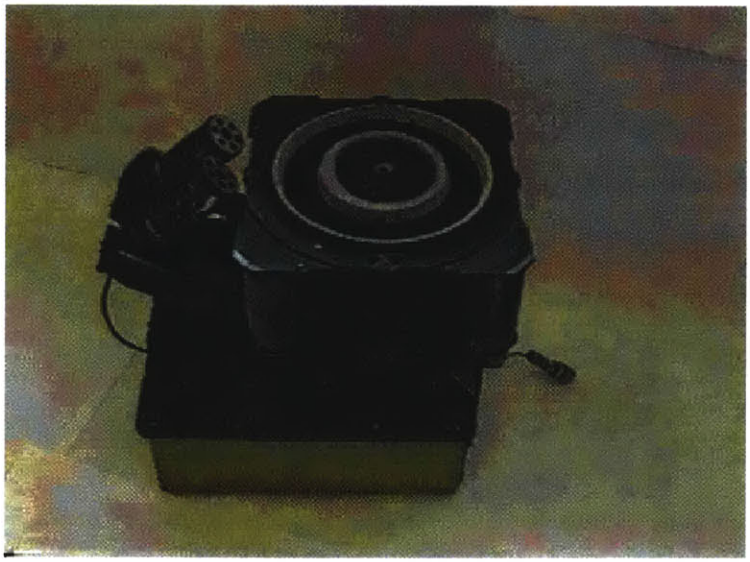

Figure 6.1: SPT-100 used in testing at the University of Michigan

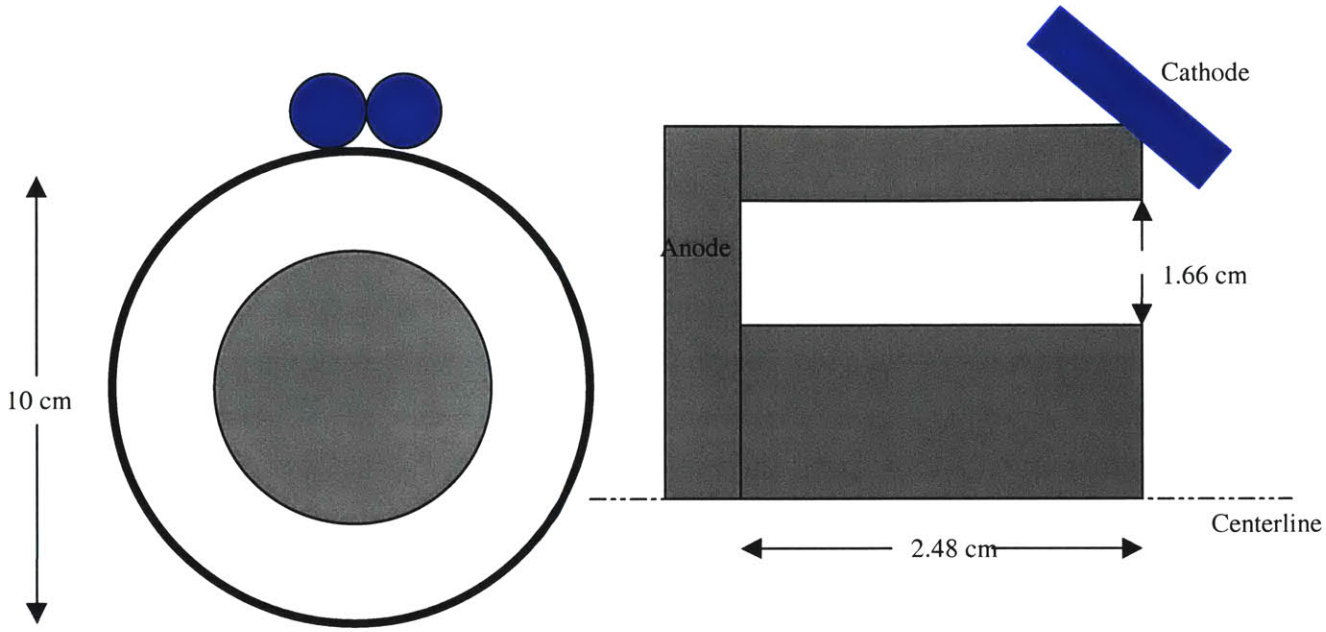

Figure 6.2: Front and side views of SPT-100 with critical dimensions.

6.2 Two-Dimensional Approximation

The original code assumes a two-dimensional axisymmetric geometry. Because his research was interested in modeling only large-scale effects, Fife ignored azimuthal magnetic field variations and azimuthal drift waves. He did account for azimuthal effects through modifications to the classical transport equations. The two-dimensional results are consistent with experimental research, so no modifications to this assumption are necessary at this time.

Oh's plume model is three-dimensional, as modeling objects in the plume requires extra capability. For those interested in directly simulating the plume's impact of surfaces outside of the acceleration zone, a three-dimensional model is necessary.

6.3 Grid Generation

The grid generator creates a non-uniform spatial grid according to boundary nodes input by the user. Elliptic partial differential equations are solved to generate the internal nodes. This method, used in computational fluid dynamics, creates a grid that closely follows the boundary shapes.

For this research, it was necessary to expand the grid to include regions in the plume. While extending the magnetic field solver was straightforward, extending the grid in the same manner is a little tricky. The boundary nodes were changed in order to capture the nodes along the centerline in the plume. More axial points needed to be added to the grid to maintain the proper spacing in the acceleration zone, as well as perform computations in the plume region. This increases the computational load, increasing the amount of time necessary for a given simulation to run.

6.3.1 Near-Field Plume

The grid for the SPT-100 plume is shown in figure 6.3. The grid spacing is consistent everywhere except the last cells along the centerline, where the rigid boundary was difficult to closely follow. The original simulation grid did not extend along the centerline in the plume, as that research was concerned with the ionization process. These cells do not appear to have any effect elsewhere in the simulation, as the density is low enough that ionization and charge exchange do not occur. The magnetic and electric fields have also fallen off such that particles moving through these cells are relatively unaffected. The regions of interest are those cells found off-axis and near the acceleration channel exit.

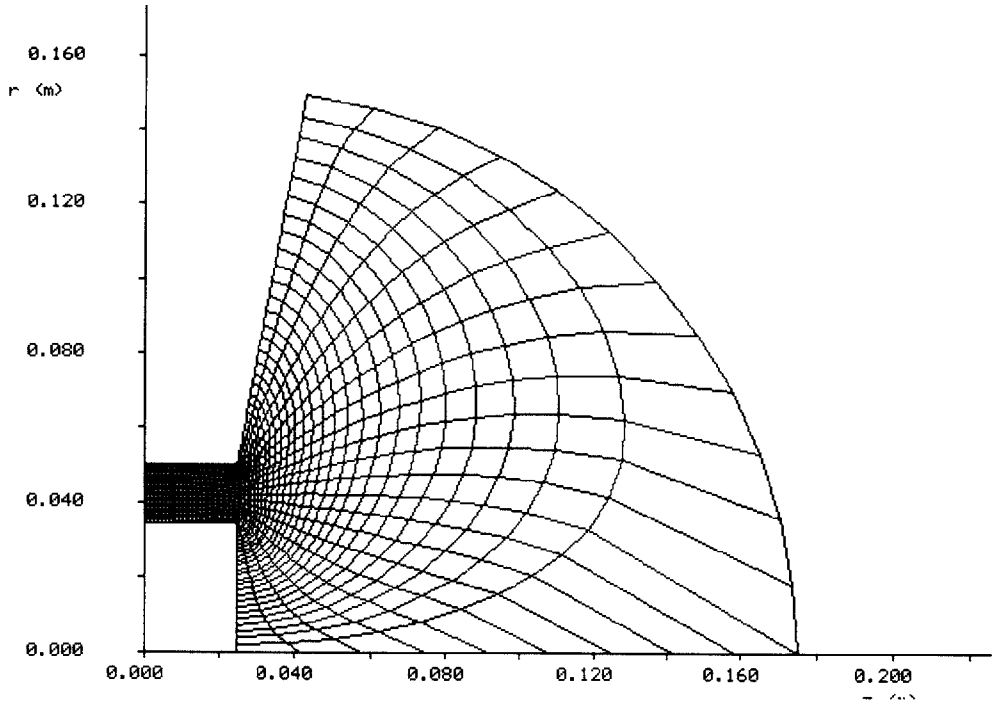

Figure 6.1: Two-dimensional grid for near-field SPT-100 geometry.

A more complex grid could easily be employed. However, for the purposes of this research, examining alternative geometries and other grid generation schemes are not as important, and are left to further testing and research. As previously reported in section 3.2.2, James Szabo increased the capability of the code to examine alternative geometries. The charge-exchange process could be studied with these geometries as well.

6.3.2 Far-Field Plume

In order to compare plume structure to previous results, it is necessary to make computations farther away from the thruster exit. Previous simulations using David Oh's code compared measurements at a radius of 60 cm to experimental results. King and Gallimore took measurements at 50 cm at the University of Michigan.

However, as explained in section 5.5.1, the magnetic field falls below that of the Earth's geomagnetic filed at the bounds of the near-field grid. The assumptions of Fife's code

may not be applicable in studying the far-field plume. However, the rate of maximum charge exchange collisions occurs within the bounds of the near-field grid. With some additional modeling of the Earth's field, it may be possible to expand this algorithm farther into the plume.

Chapter 7: Simulation Results

The following sections present the results from the simulation. The baseline calculations for the expanded grid are shown, along with a discussion of the unsteady effects computed at downstream "probe" locations. Then, the effect of CEX collisions is examined. The location, velocity, and energy distribution of the ions in the plume are plotted for study.

7.1 Baseline Plume Characteristics with Expanded Grid

Before looking at the effects of CEX events, it is important to examine the baseline characteristics of the near-field plume region with the expanded grid. The following sections discuss the performance parameters for an SPT-100 run according to Fife's original algorithm (without CEX, and no condition on current in the plume), on the expanded grid. The code finds the cathode itself, and downstream of that point, Φ^* is just a constant, so Φ is a function of ion number density and electron temperature alone. In general, the temperature, potential, and ion density are unchanged from the baseline plots in Chapter 3. Both runs show a peak temperature of near 18 eV occurring just outside the acceleration chamber, and a potential at the exit plane of near 130 V.

7.1.1 Potential

As seen in figure 7.1, much of the potential drop remains outside the engine exit. Ions created at the exit can travel radially without impacting a wall, allowing for an increased beam divergence angle. The potential contours can be adjusted by changing the boundary condition and the cathode placement. Fife found that to match his experimental results, the cathode should be placed 5 mm downstream of the exit. The above results allow the code to find the cathode itself, at a radius of 0.07m. Placing the cathode in this location gives result sthat seem to match the experimental work at the University of Michigan, where ions with energies over 200V were found at more than 90 from the

thruster center line. In Fife's thesis, he manual set the cathode 5mm from the exit to match his own results, where the potential at the exit was found to be only 35 V. In doing so, his temperature peak was inside the engine. Fife's experimental results show a temperature peak outside the engine, however.

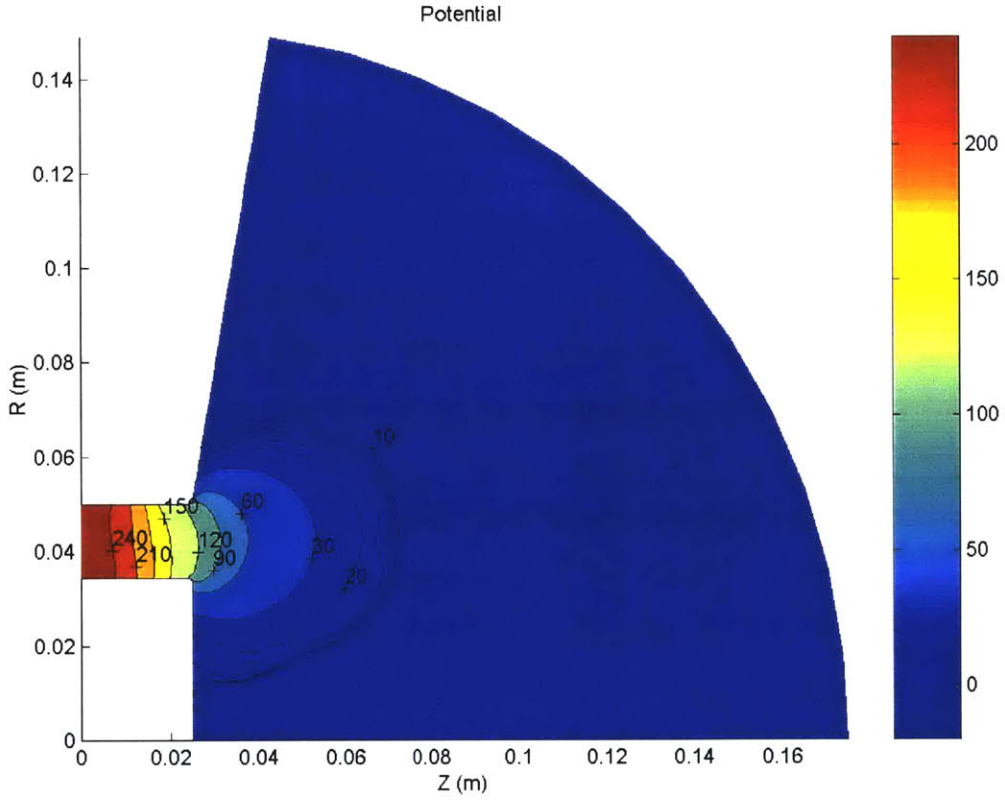

Figure 7.1: Space potential (V) plotted in the engine geometry. Cathode at r=0.07m.

Much of an ion's acceleration occurs outside the acceleration chamber, where the magnetic and electric fields are less regular. The potential is higher near the centerline of the engine where the "apparent jet" usually attaches. This "jet" is visible in the contour plot of ion density, which follows later. The next figure shows a close up of the acceleration zone, where most of the potential drop occurs. The potential at the exit plane is about 120V, so 180 V have dropped internally.

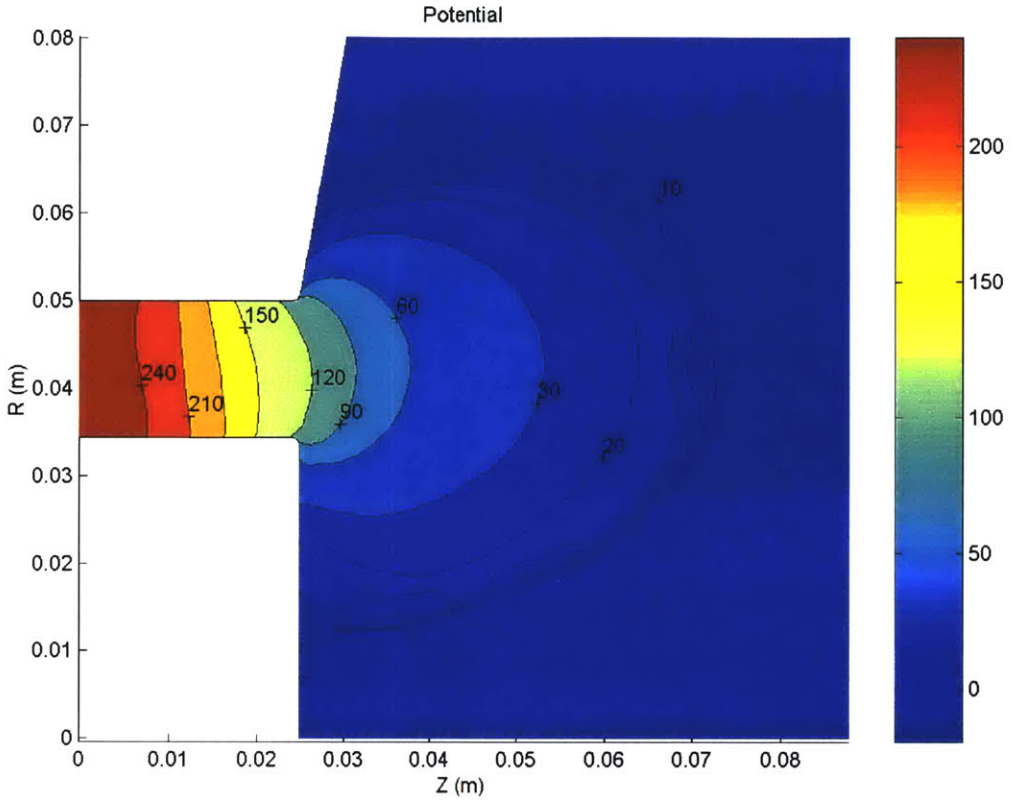

Figure 7.2: Zoom in for baseline potential contours. Cathode at r=0.07m.

7.1.2 Electric Field

Changes in potential give rise to the electric field, which is responsible for the forces that accelerate the ions. Figure 7.3 shows a vector plot of the electric field. Clearly, near the engine exit, the field has strong radial components. Notice that this happens despite the nearly radial shape of the magnetic lines in this zone. Thus, the usual argument that shaping the B-lines can "focus the beam" is incomplete. Ions created in this region, from ionization or CEX, can accelerate radially. The strongest field is still in the axial direction, imparting the greatest force on those ions that travel in the exhaust beam.

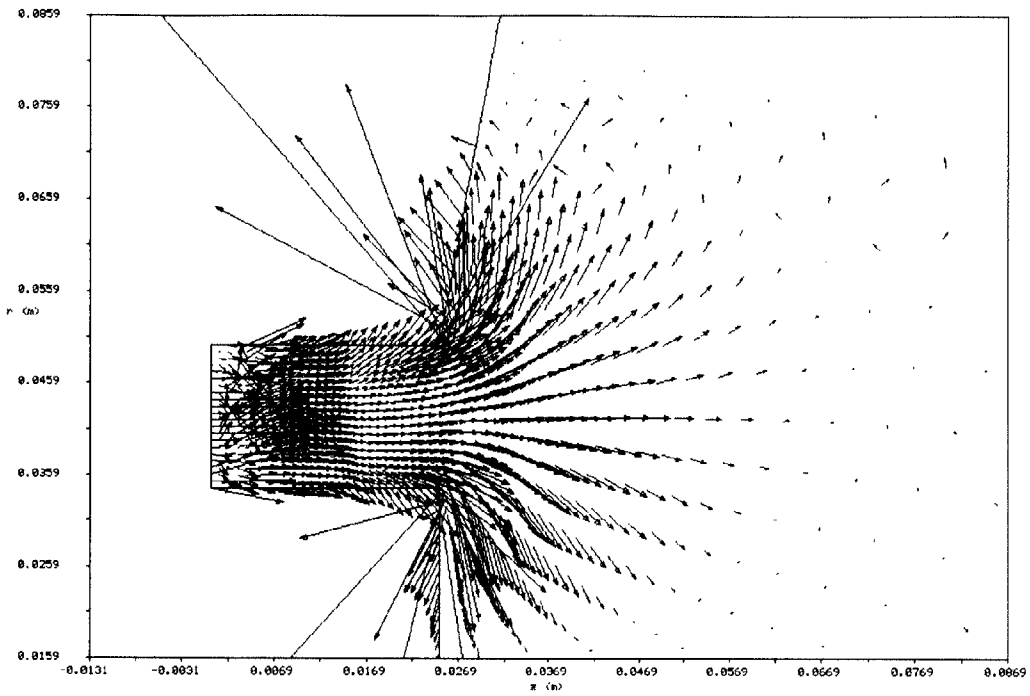

Figure 7.1: Electric field near acceleration zone.

There are some field vectors, at the corners of the engine, with negative z-components. Slow ions in this region can be pushed out of the beam, back towards the engine mounting and the spacecraft.

7.1.3 Ion Velocity

Figure 7.4 shows a vector plot of the average ion velocity for each grid point. Some ions accelerate radially with a large total velocity, indicating a high energy level. The fastest particles travel axially, but a considerable amount of energy is put into radial flow in the plume.

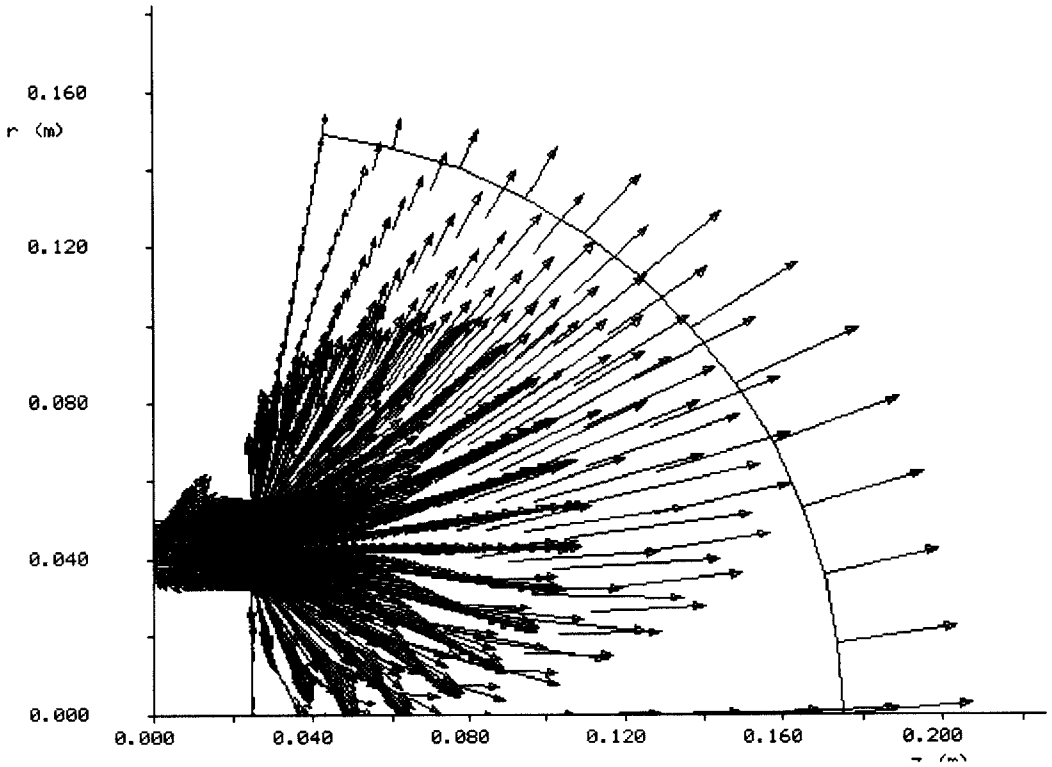

Figure 7.1: Average ion velocity.

The slow ions traveling radially are the particles that are susceptible to further accelerations from external space fields, which could draw the ions back towards the spacecraft and other components.

7.1.4 Ion Density

Figure 7.5 shows the ion density in the near plume region. The densest regions, outside of the acceleration zone, are found near the centerline of the engine. During typical Hall thruster operation, a "plasma jet" will form at the centerline. This jet appears as a conical region of relatively high plasma density that can attach itself to the center of the thruster. The base of the jet may also stand off from the thruster by a few centimeters, depending on magnetic field settings and cathode placement. The density falls off as the plume expands into vacuum.

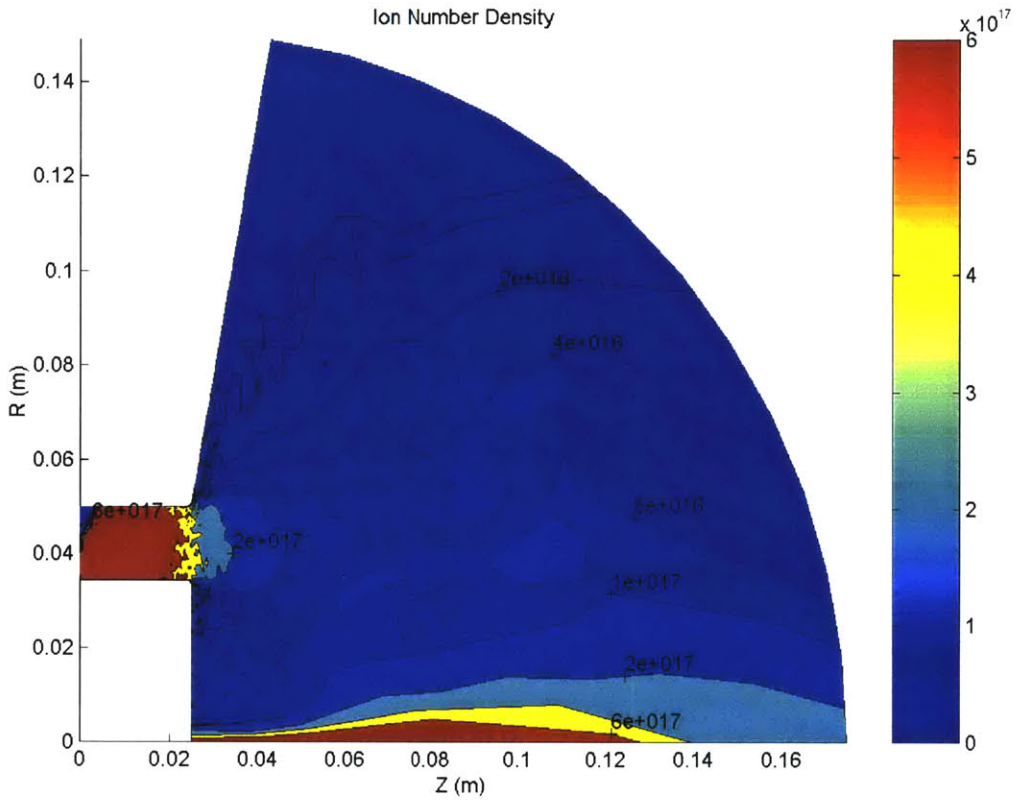

Figure 7.1: Ion number density in near plume region. [m^{-3}]

Evidence for the formation of the plasma jet is found in the higher density plasma focused towards the centerline. The ion beam widens, beginning about 6 cm from the thruster exit. The potential drop, which occurs outside the acceleration zone, allows for a relatively higher beam divergence angle. Results from further analysis of the plume will attempt to explain this in more detail. A region of high ion density can be seen accelerating radially just above the thruster exit. This plasma sees nearly 200 volts of potential drop, but moves perpendicular to the thrust axis.

7.1.5 Electron Temperature

As further evidence for the shape and formation of the plume, the electron temperature is shown in figures 7.6 and 7.7. Figure 7.6 shows the full grid domain, with the relatively hot plasma beam, while figure 7.7 shows a close up of the thruster exit.

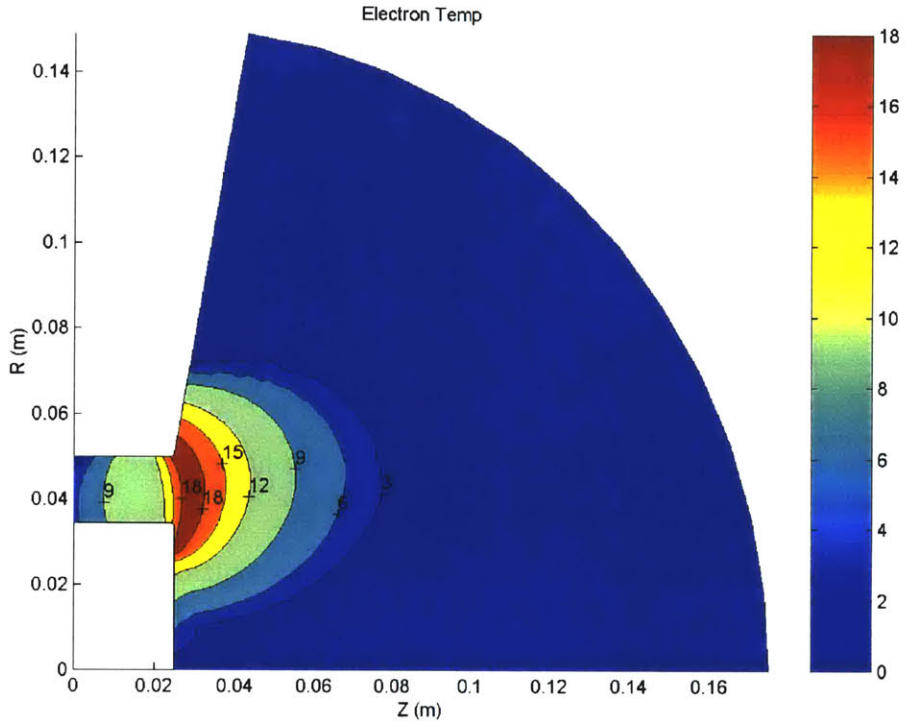

Figure 7.1: Electron temperature [eV].

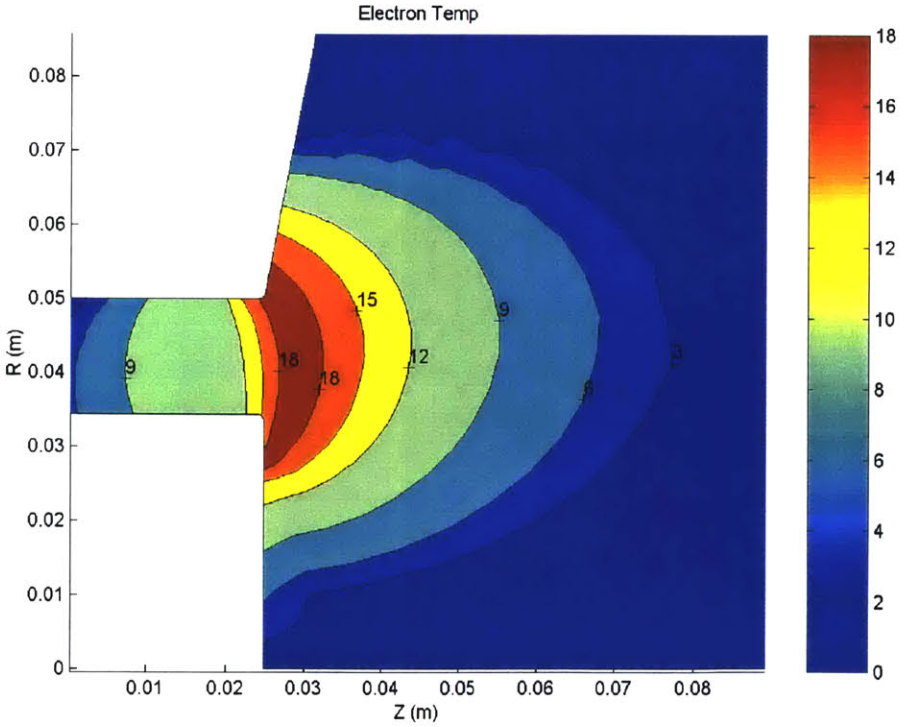

Figure 7.2: Electron temperature [eV] – zoom in.

The hottest region of the plasma is just outside the thruster exit, where the electric field grows strongest. These results match Fife's experimental work, in so far as the temperature peaks outside the acceleration zone. The peak temperature is a little higher than that observed experimentally; in fact, the simulation regularly predicts high temperatures.

7.1.6 Charge-Exchange Collisions

Figure 7.8 shows the regions of maximum CEX collisions. The highest rates occur inside the thruster itself, but collisions still occur at a rate near 10^{21} $m^{-3}s^{-1}$ at the thruster exit. While this is only 1% of the ionization rate, slow ions are created outside the engine, with lines-of-sight up to 90° off the thrust axis. There is still plenty of potential drop from which these slow ions can pick up radial velocity.

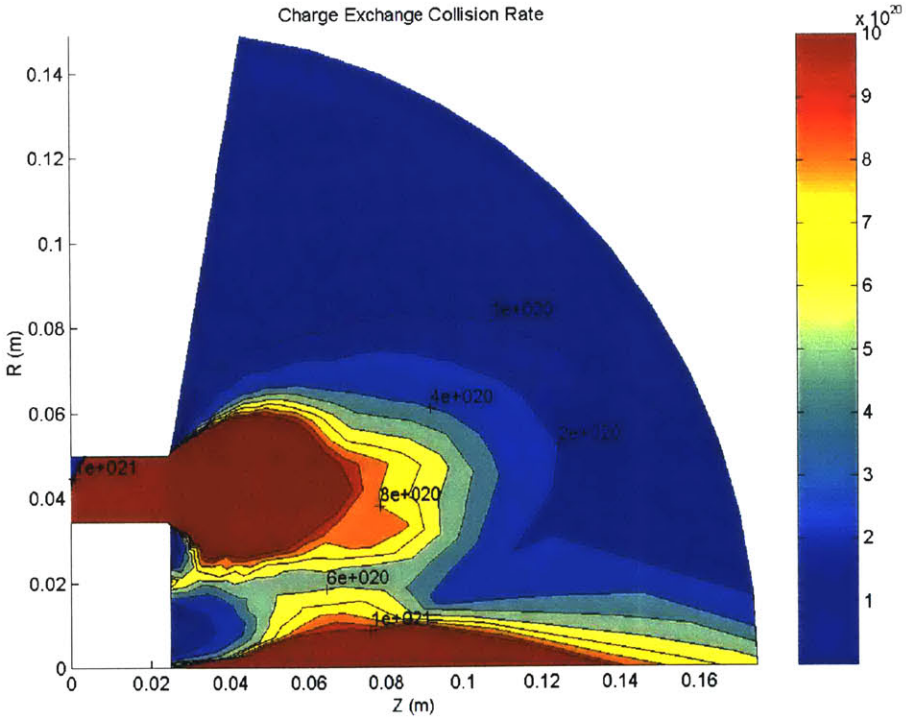

Figure 7.1:Charge exchange collision rate. [$m^{-3}s^{-1}$]

CEX events also occur in the plume jet where the ion and neutral densities are high. These ions, created at a low potential, can still react to space potentials and gain energy from spacecraft sheaths.

7.2 Unsteady Plume Characteristics

In addition to looking at static, time-averaged, pictures of plume performance, time dependent values can be examined. A set of "computational probes" were set up at several downstream locations to record changes in potential, temperature, and ion number density. "Probes" were placed at two axial locations along the center of the annulus, inside the acceleration zone. Other plume probes were placed at varied axial and radial locations, all of which are shown superimposed on the grid in figure 7.9.

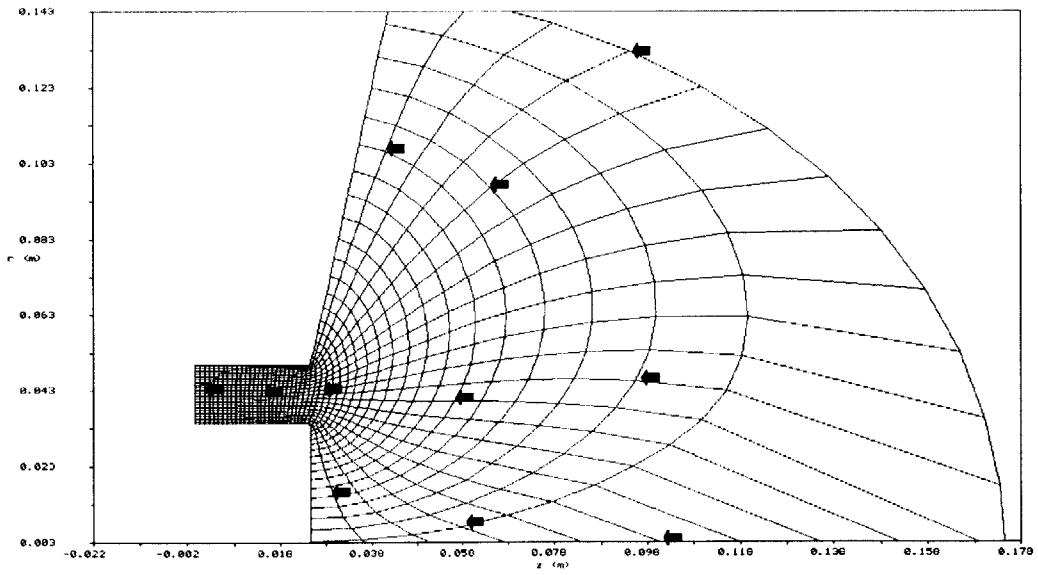

Figure 7.1: Simulation probe locations, super imposed on the grid.

The probes record the first 15,000 iterations of operation, from beginning of life. A transient is often seen in the first 1000 iterations or so. During this time, the anode current spikes. After it settles back down, regular oscillations are seen. Figure 7.10

shows the anode current and Isp for the engine, after the engine has settled into steady oscillatory behavior.

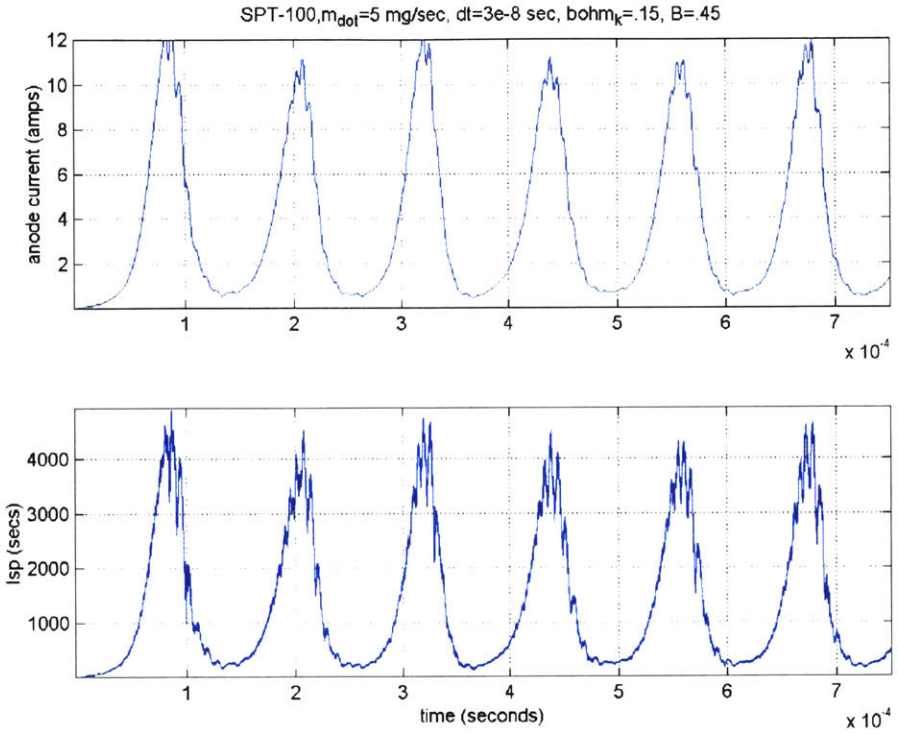

Figure 7.2: Anode current and Isp for hall thruster simulation.

The performance averages to 1580 seconds of Isp and an anode current of 4.4 A. The oscillations occur near 9 kHz. The beam current and anode voltage are plotted in figure 7.11. The same oscillations are apparent.

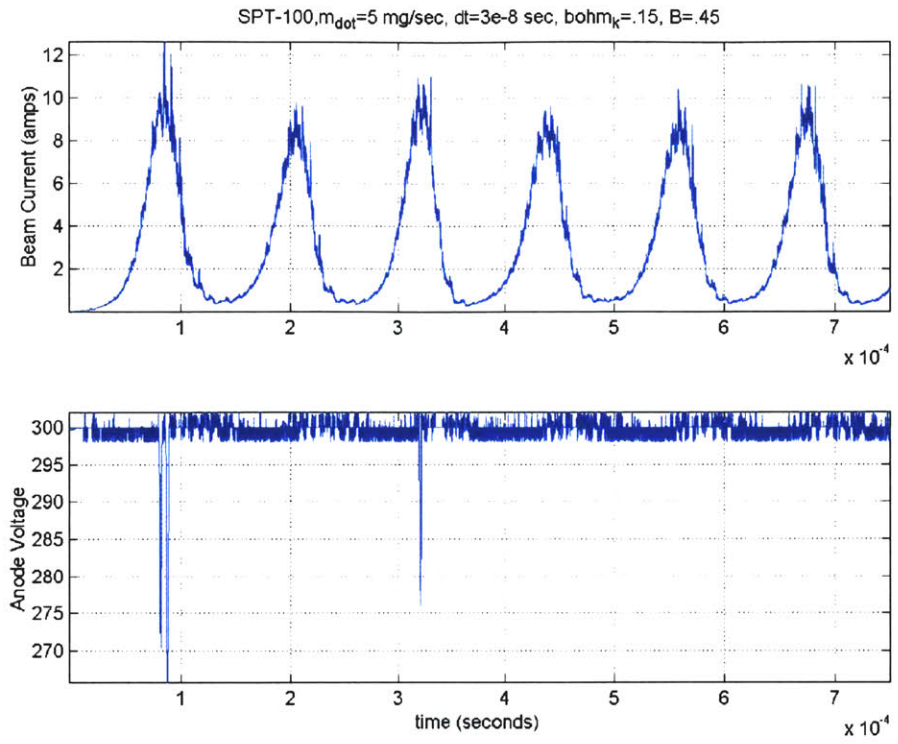

Figure 7.3: Beam current and Anode voltage for SPT-100 simulation.

The initial drop in anode voltage corresponds to the current spike in the first transient oscillation. The power supply simulates a constant voltage supply, but is used computationally to bring the current under control during the first iterations. Other spikes in anode current occur at places where the power begins to exceed the maximum power of the device; however, these points have little effect on the simulation.

The following plots show potential, electron temperature, and ion density respectively for each of the probe locations in the simulation, starting with the ones inside the engine and working out into the plume at successive axial stations. The low frequency oscillations match the oscillations in anode current and Isp. The high frequency oscillations are thought to be a remnant of the detailed wall interaction model. The simulation may be run with a simple wall model in which the higher frequency oscillations are not present. The detailed wall model assumes there is an sheath that moves from ion attracting to ion repelling depending on the potential and temperature distribution at a given time. The

wall current is a function of secondary electron emission, which is a function of electron energy. The simple wall model assumes the sheath always exits. However, the calculated temperatures are less accurate, tending to over predict the electron temperature at the exit.

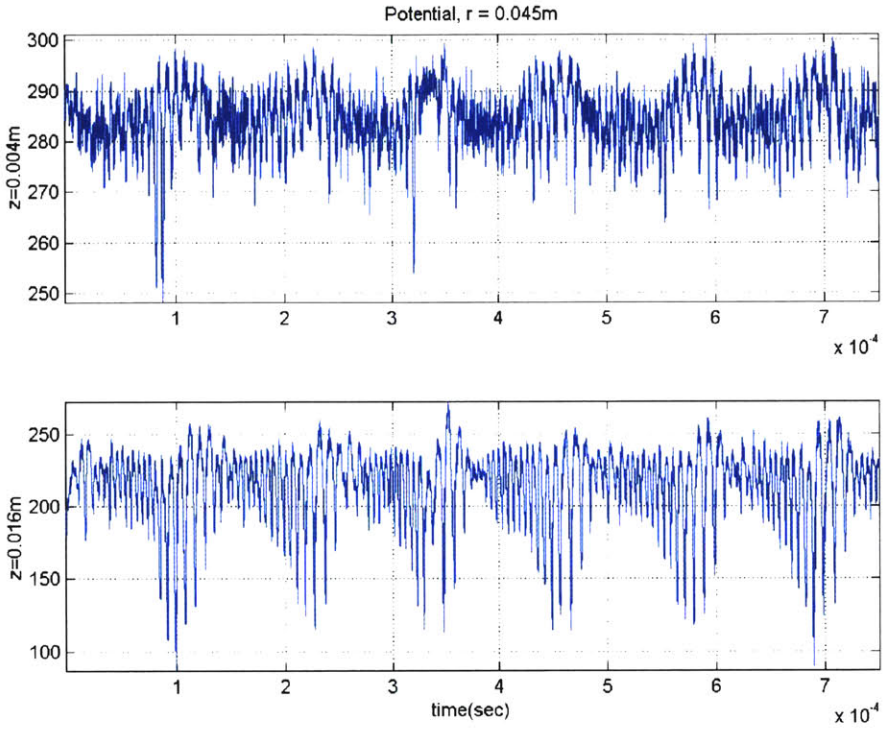

Figure 7.4: Potential vs. time in the acceleration zone, both axial stations shown.

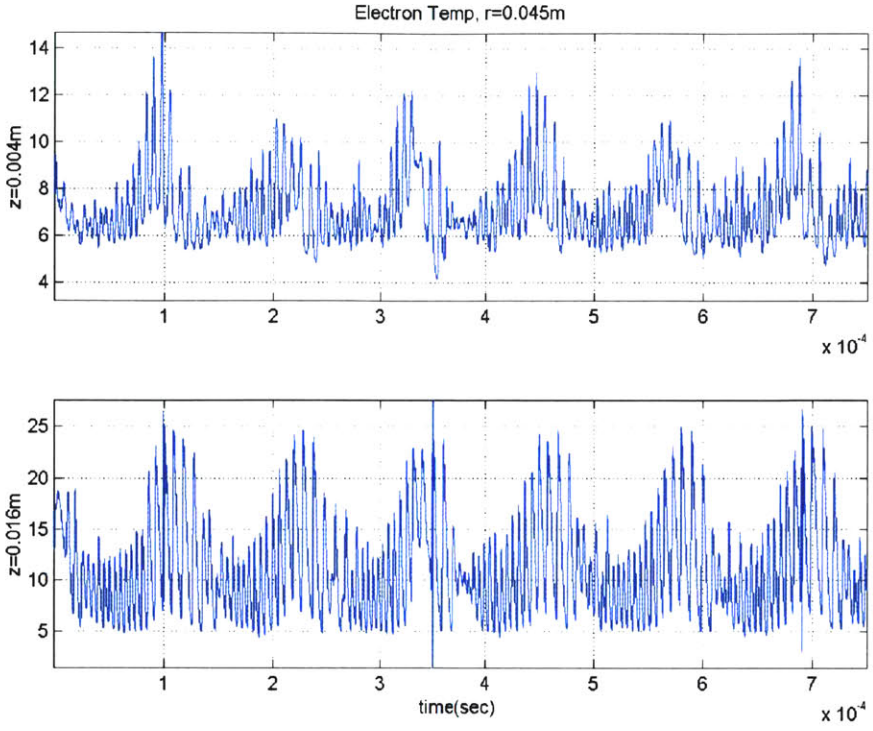

Figure 7.5: Electron temperature vs. time in acceleration zone.

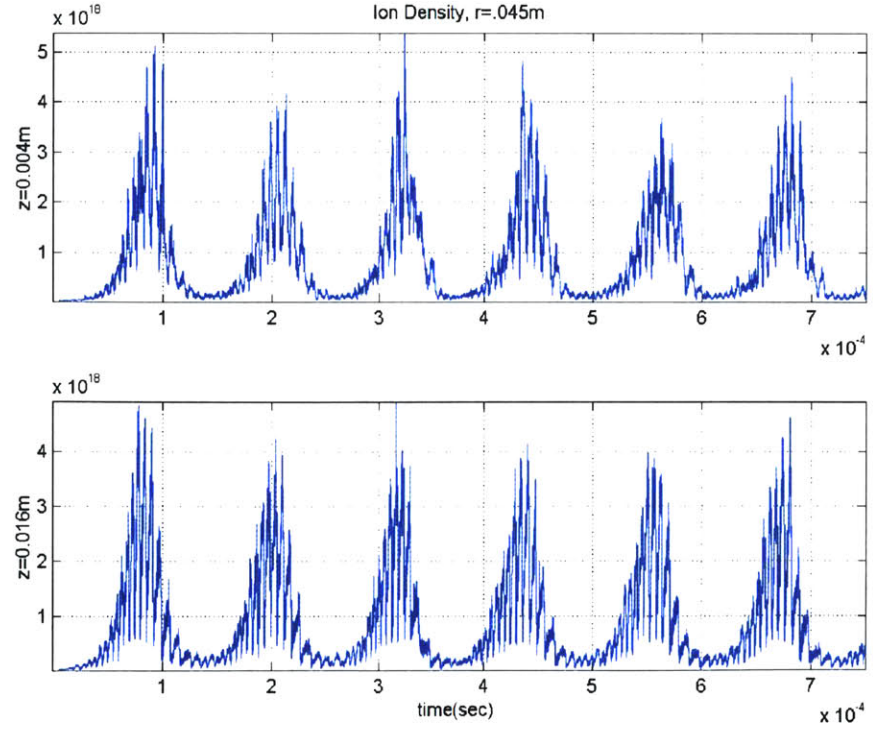

Figure 7.6: Ion density vs. time in acceleration zone.

For the plots in the plume probes, all three radial stations are shown for each axial position to view the characteristics in a profile across the plume.

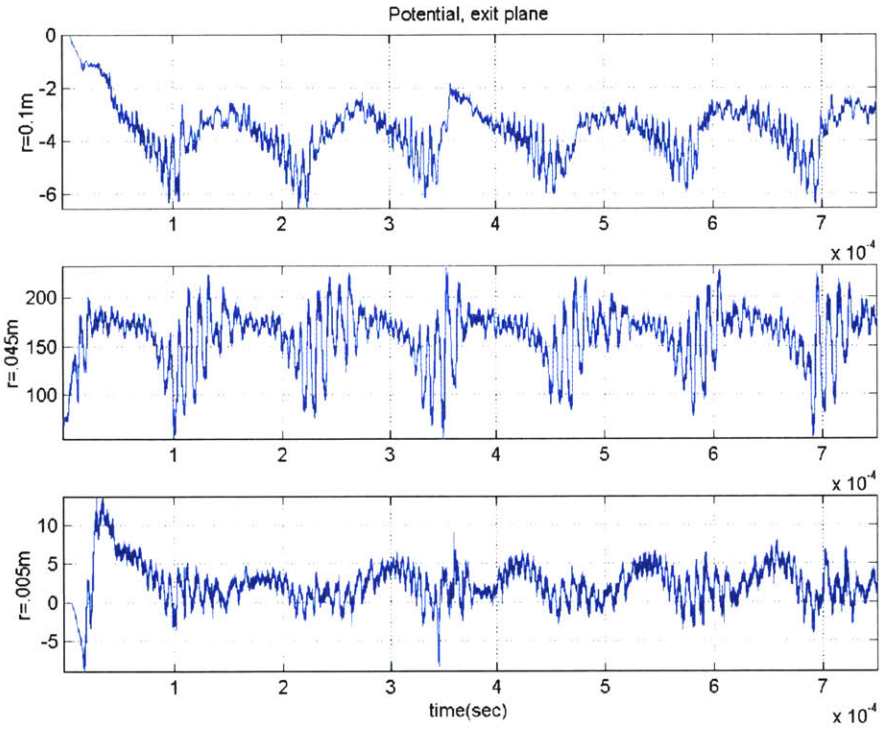

Figure 7.7: Potential vs. time at the exit plane.

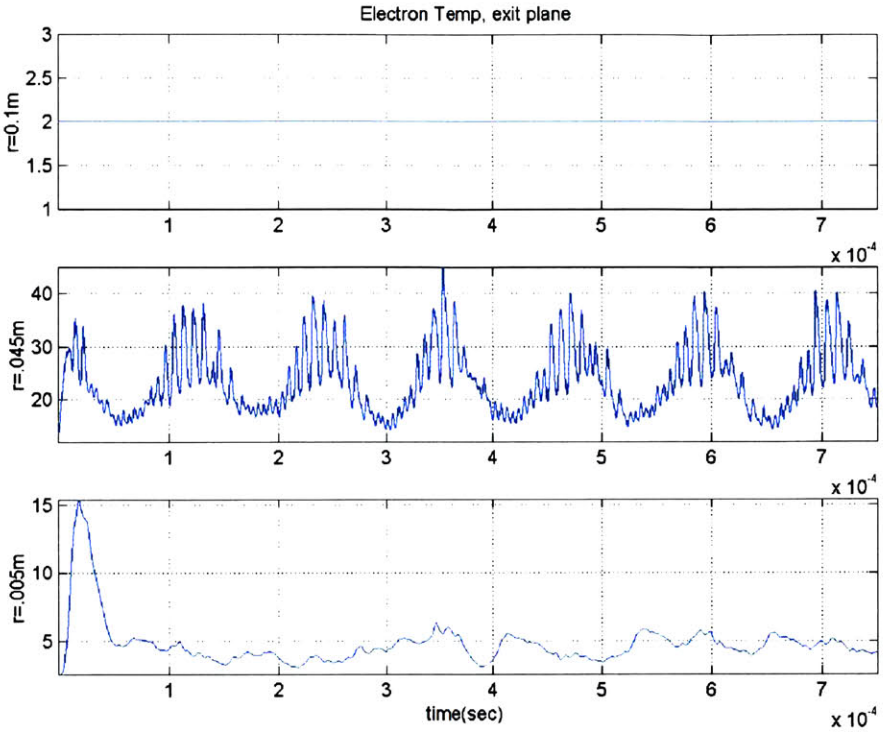

Figure 7.8: Electron temperature vs. time at the exit plane.

As seen at the 0.1 meter radial station in figure 7.16, the electron temperature is set at 2 eV. This corresponds to the downstream temperature boundary condition placed on the solution to the electron equations. At those locations beyond the last lambda line, the temperature is set at 2 eV. Due to the curvature of the lambda lines, (and curvature of the magnetic field in the near plume region) radial stations may fall outside the core flow where temperature is assumed to be constant as a boundary condition. This will also be apparent in figure 7.19 and 7.22, the electron temperature at further downstream locations.

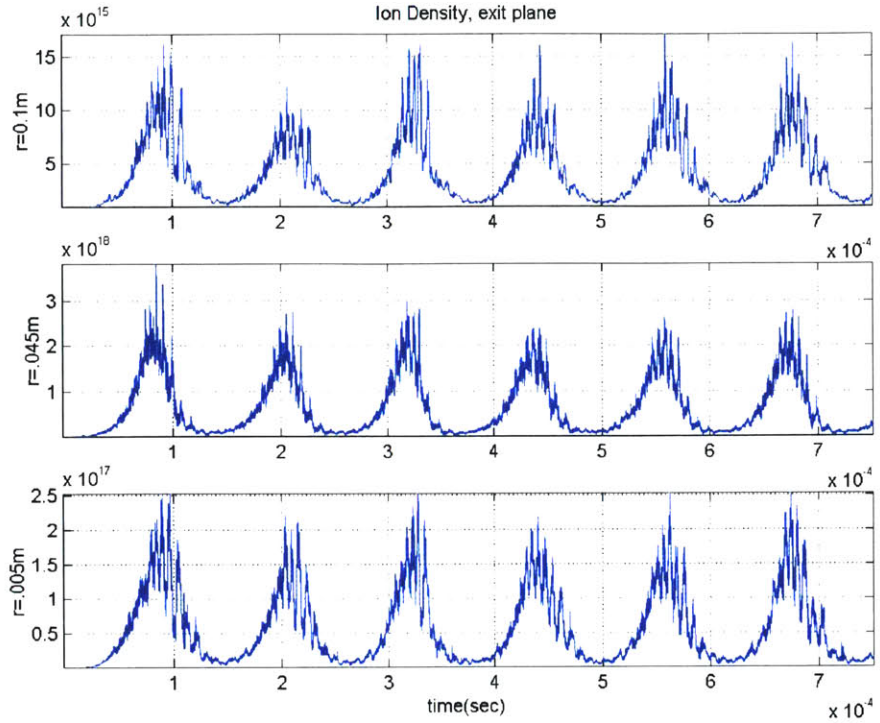

Figure 7.9: Ion density vs. time at the exit plane.

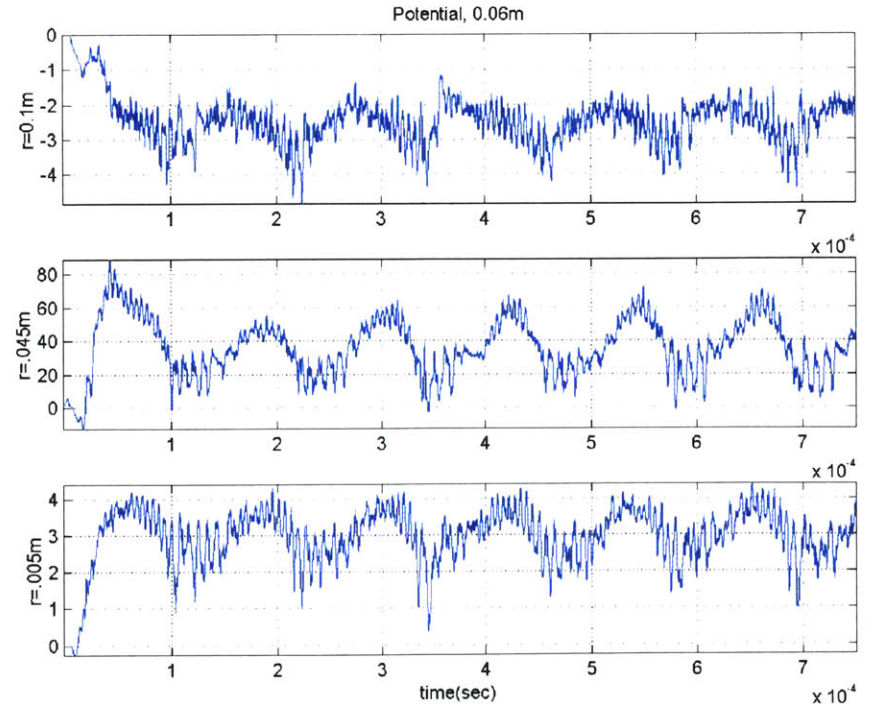

Figure 7.10: Potential vs. time, 0.06 m from anode. (3.5 cm from exit plane)

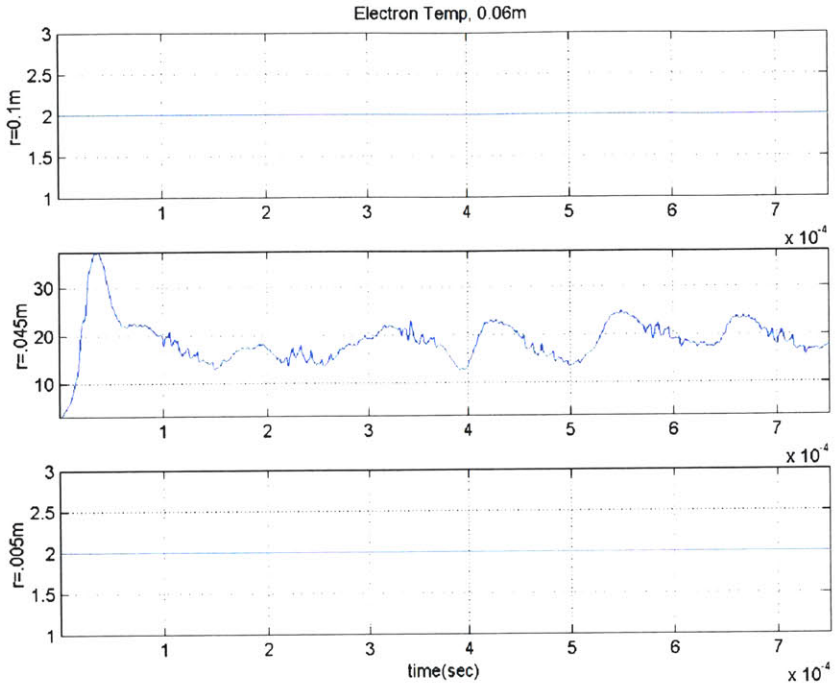

Figure 7.11: Electron temperature vs. time, 0.06 m from anode. (3.5 cm from exit plane)

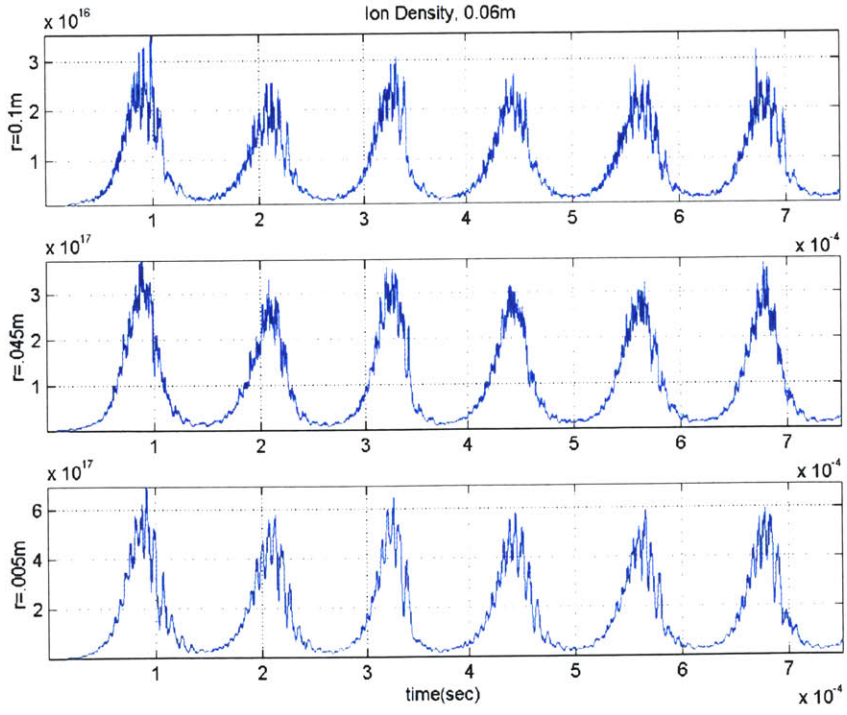

Figure 7.12: Ion density vs. time 0.06 m from anode. (3.5 cm from exit plane)

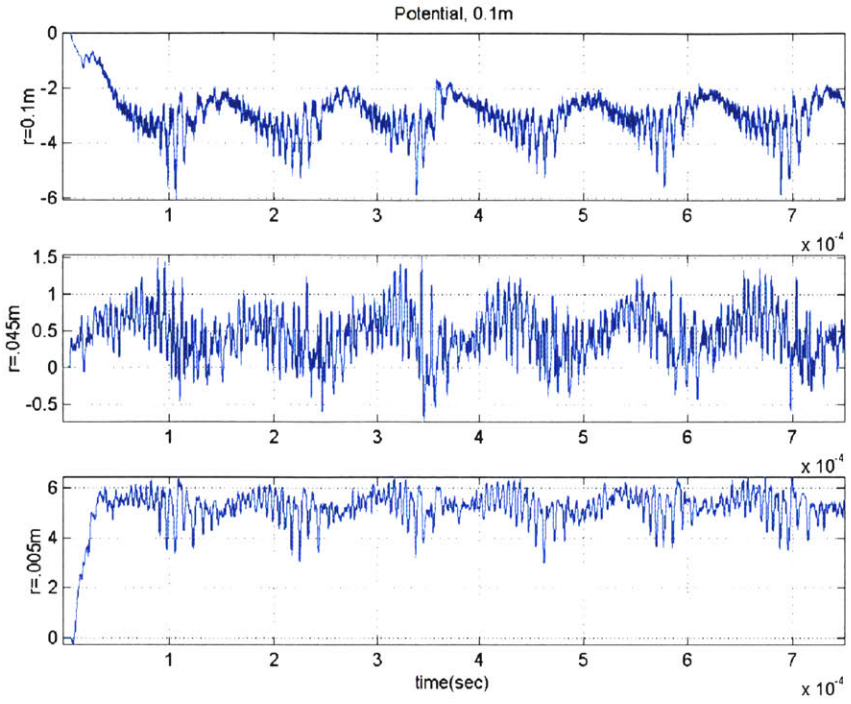

Figure 7.13: Potential vs. time, 0.1 m from anode. (7.5 cm from exit plane)

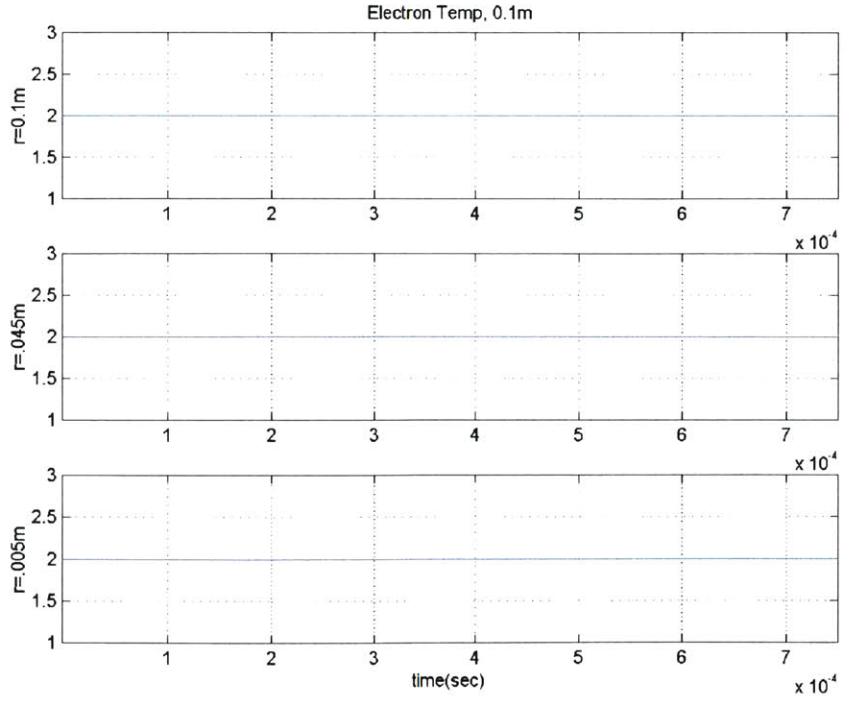

Figure 7.14: Electron temperature vs. time, 0.1 m from anode. (7.5 cm from exit plane)

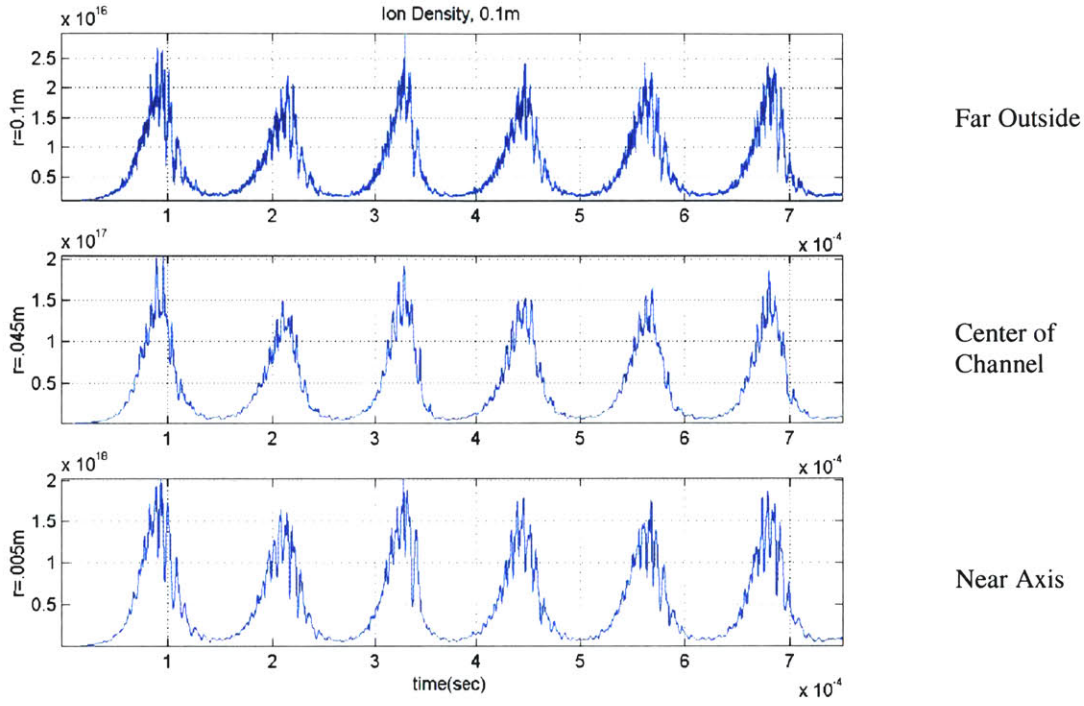

Figure 7.15: Ion density vs. time, 0.1 m from anode. (7.5 cm from exit plane)

The oscillations in ion density, on the scale of the entire simulation, appear to happen at the same time. Figure 7.24 shows a plot of the ion density from each downstream station along the centerline of the annulus, zoomed in for resolution. It is more clear that the rise and fall in ion density progresses from station to station over time, however it is still unclear if batches of ions are moving in a traveling wave or a standing wave. It only takes a few iterations in computational time for the ions to move from station to station, so not much can be said without more resolution.

Recent work [Fife, unpublished] confirms that for the magnetic geometry used here, the oscillations are predicted to be purely local. With magnetic shields that reduce B near the anode, a very difference behavior results, with detachments of small plasma clouds near the anode which then travel rapidly downstream.

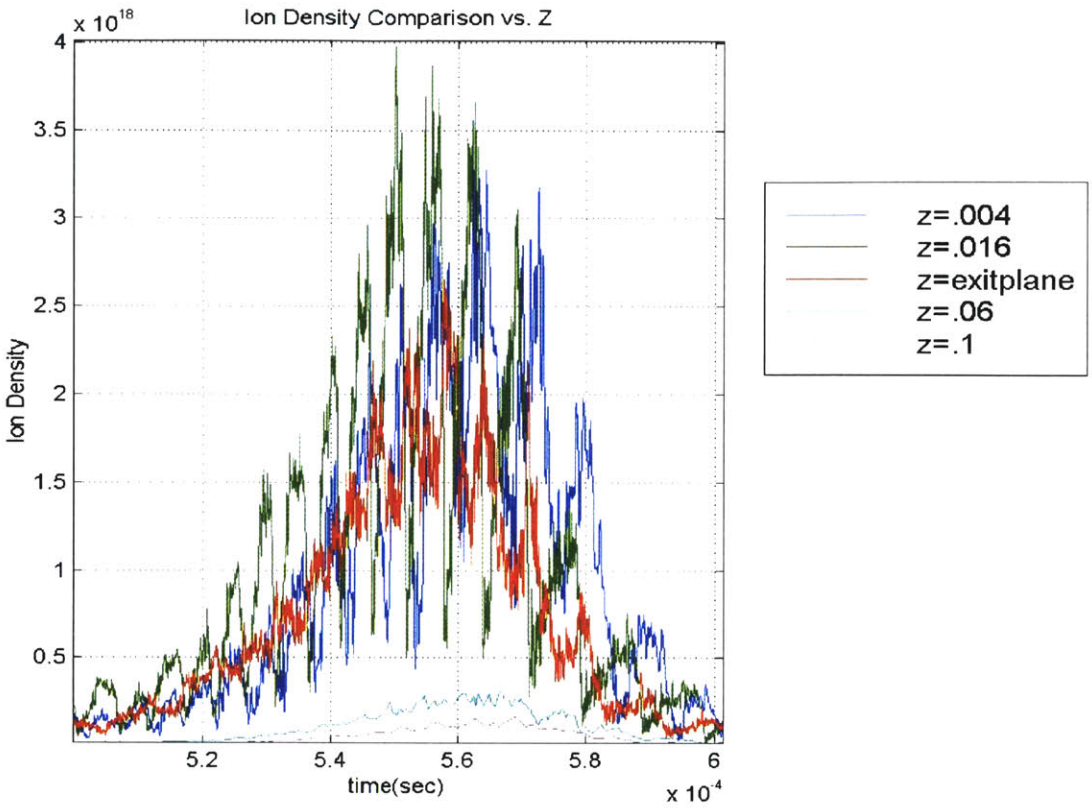

Figure 7.16: Ion density at successive downstream locations vs. time.

On the scale of a global oscillation, it is difficult to discern much about the ion density oscillations. They appear to be instantaneous. However, looking at a much smaller timescale, as in the next figure, one can see that the rise and fall in ion density progresses somewhat axially along the engine. The high frequency oscillations, believed to be caused by the detailed wall interaction, can be tracked moving axially. Once outside the engine, at points beyond the exit plane, these oscillations are not as apparent, as there is no wall interaction and the density has decreased as the plasma expands.

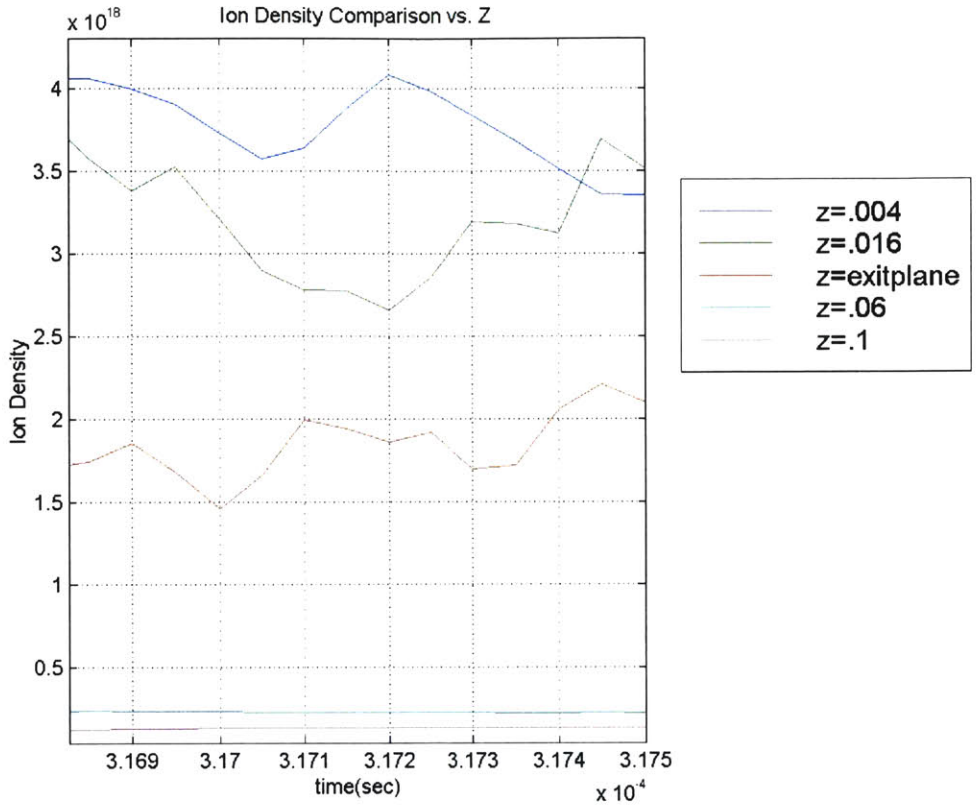

Figure 7.17: Close comparison of oscillations in SPT-100.

These oscillations appear much faster than the normal ion velocity. It is unclear what is the relationship of the traveling features in the above plot to the physics of a Hall thruster at this point. The simulation was re-run with a simple wall interaction model to eliminate many of the oscillations, but those results are inconclusive as well.

7.3 Effect of Charge Exchange Collisions

The simulation was run again assuming charge exchange collisions. The output data are plotted in the following figures. Many characteristics remain constant, even when CEX collisions are included. A few key differences are outlined below.

7.3.1 Two-Dimensional Results

Figure 7.26 shows the time-averaged plasma potential. The contours look much like the previous results; however, the potential at the exit plane is about 50 –60 V higher than the previous results. It is hypothesized that more ions stay inside the engine (slow ions from CEX), which elevates the potential.

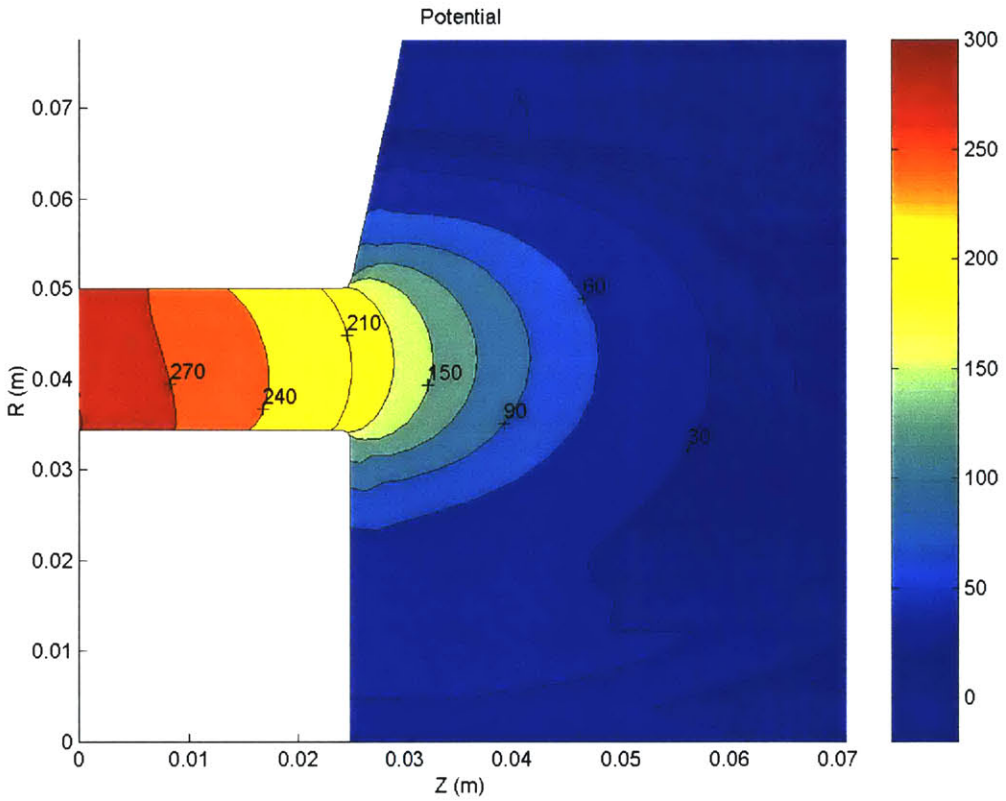

Figure 7.1: Plasma potential [V] for SPT-100 simulation, including CEX.

However, the ion density is very similar, as seen in figure 7.27. The density contours appear to extend slightly farther outside the engine than the baseline plot in figure 7.5. More work is necessary to confirm this hypothesis, though.

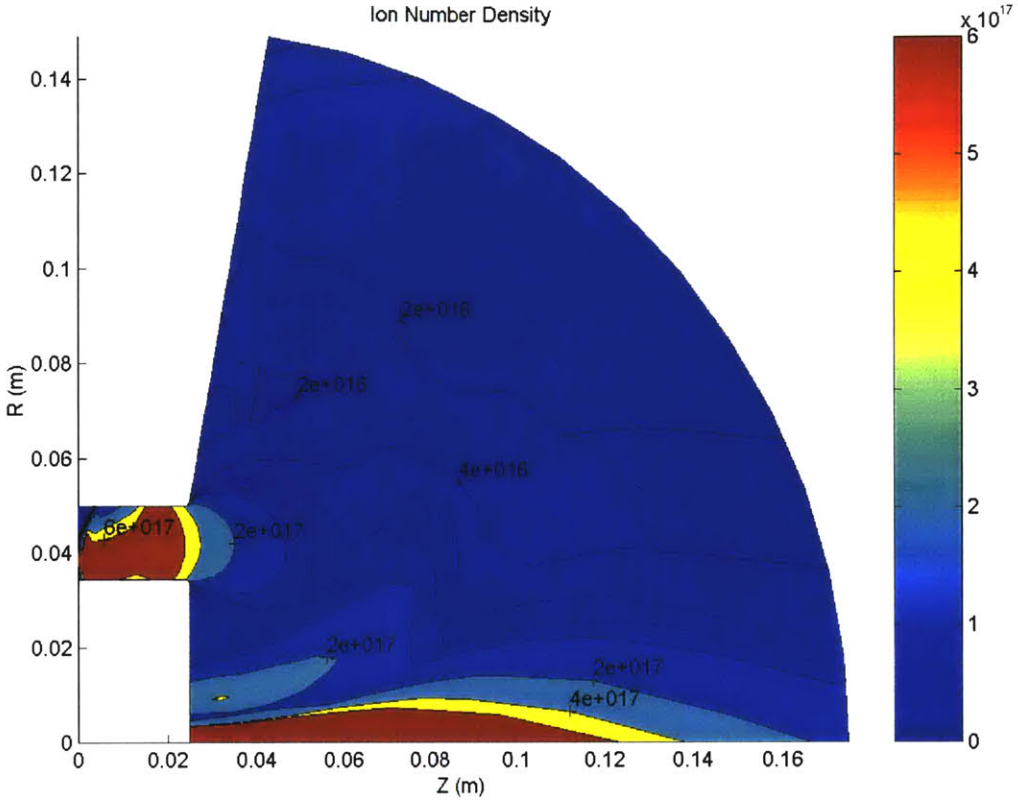

Figure 7.2: Ion density [m^{-3}]in SPT-100 simulation, including CEX.

The electron temperature matches the results that ignore CEX events as well.

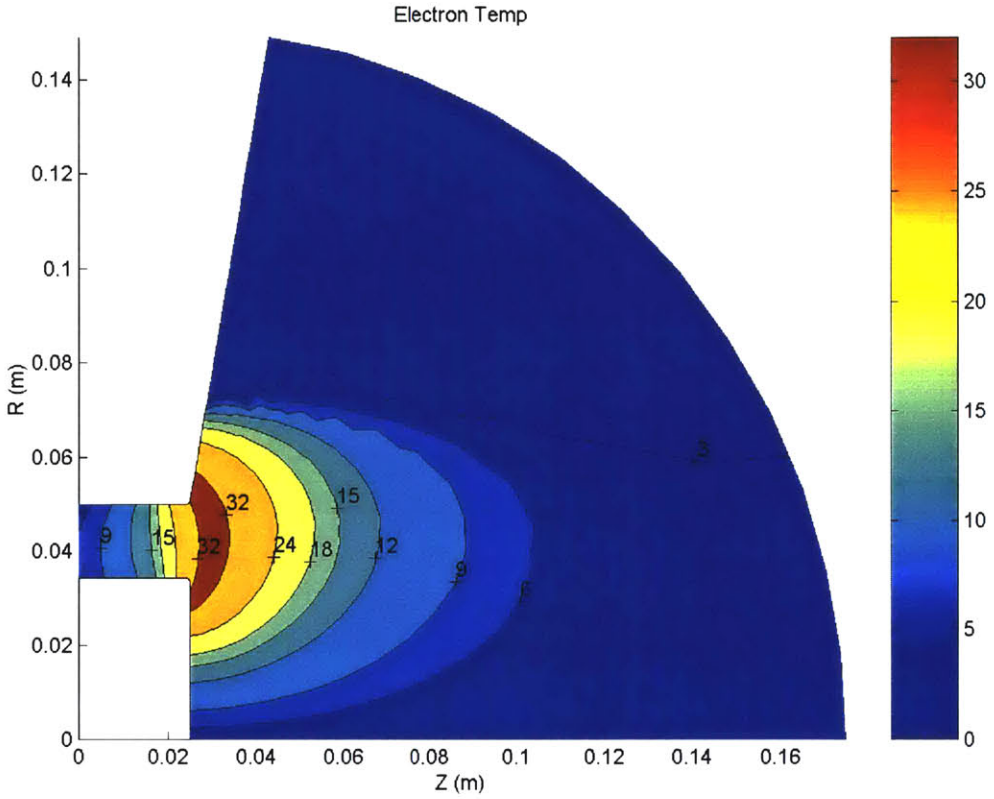

Figure 7.3: Electron temperature [eV] for SPT-100 simulation, including charge exchange.

There appears to be no significant differences, other than potential, between the simulation results, regardless of the presence of charge exchange ions in the simulation. The overall performance data are also similar to runs without CEX ions in the simulation. The Isp averages to 1600 seconds and the beam current is 4.5 Amps.

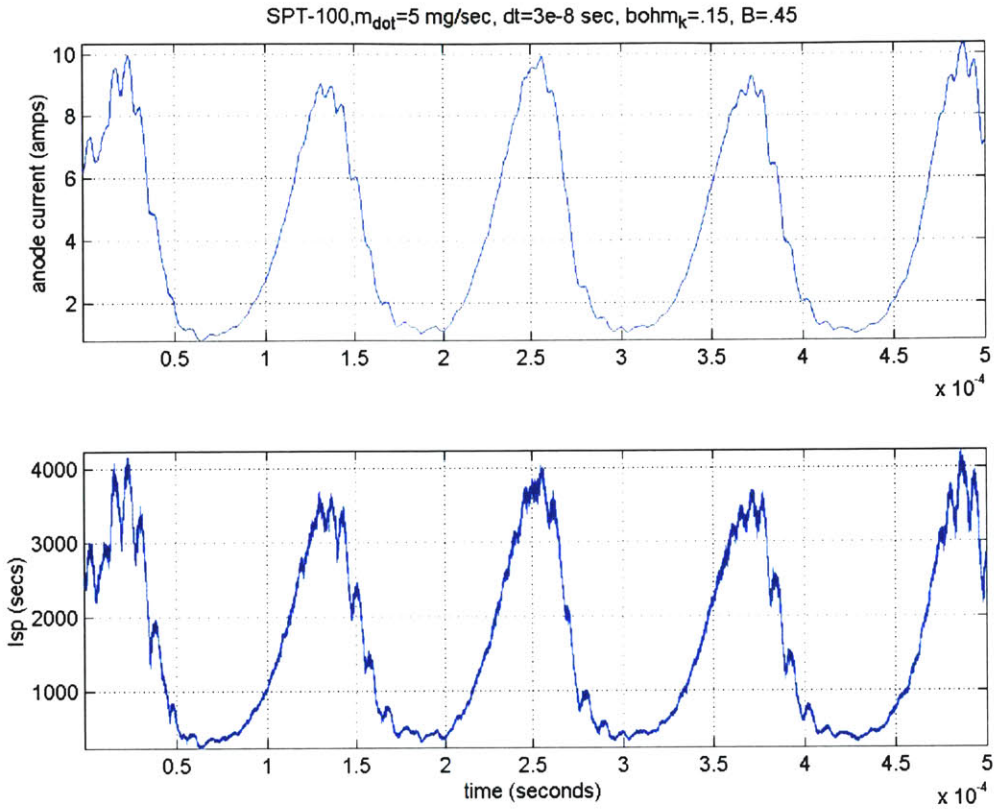

Figure 7.4: SPT-100 simulated performance with CEX collisions present.

7.3.2 Charge Exchange Ions in the Plume

Assuming that the performance of the engine itself, and the structure of the near plume region are relatively unaffected by CEX ions, it becomes interesting to look at those ions farther into the plume. As ions leave the simulation, traveling beyond the point at which it is safe to say that electrons are contained by the engine's magnetic field, their characteristics may be recorded for analysis. The following data plots predict the structure and attributes of the plume.

Figure 7.30 shows the beam current density plotted as a function of divergence angle in the plume. Previous experimental results show a current peak at the centerline of the engine. The results from this simulation, taken at a distance of 15 cm from the exit plane,

still show the effect of the center piece of the engine. The maximum current occurs slightly off the centerline, as the engine exhaust is from an annulus, not a single point at the center.

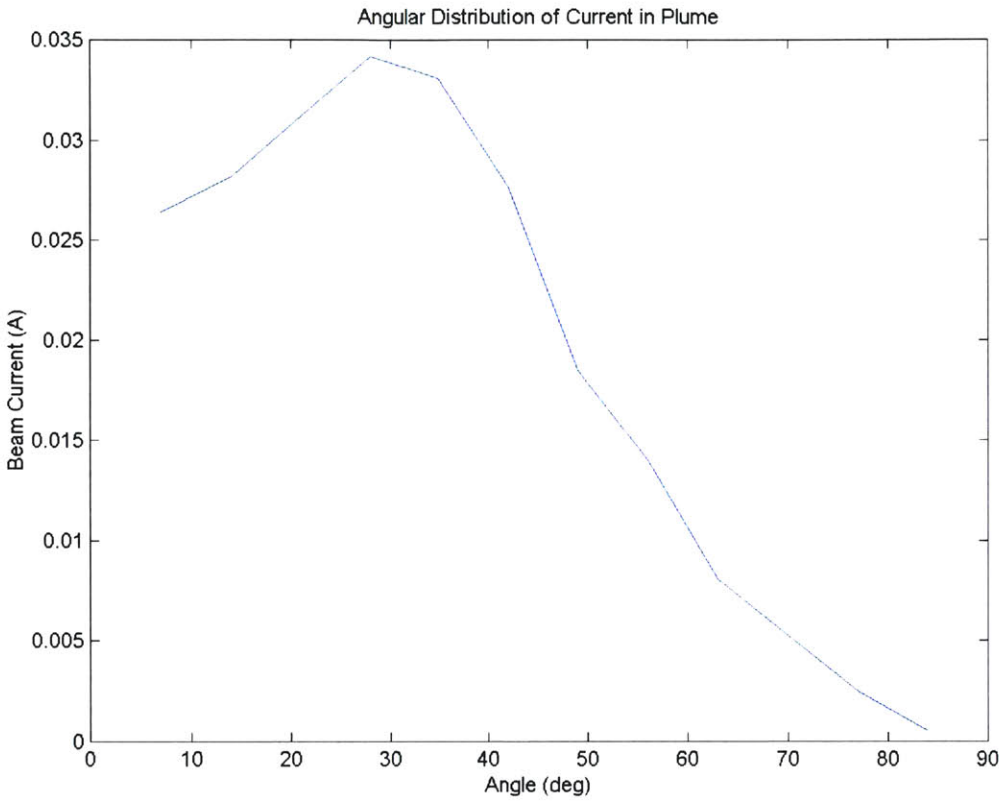

Figure 7.1: Beam current density [A/cm^2] in the plume, as a function of divergence angle.

The velocities of ions in the plume region, marked by type of ion, can be plotted in velocity phase space. The following figures show the axial and radial velocities of ions created inside the acceleration zone, ions created (through ionization collisions) outside the acceleration zone, and charge exchange ions. These ions were collected from those particles leaving the right-hand-side of the simulation grid, into the plume.

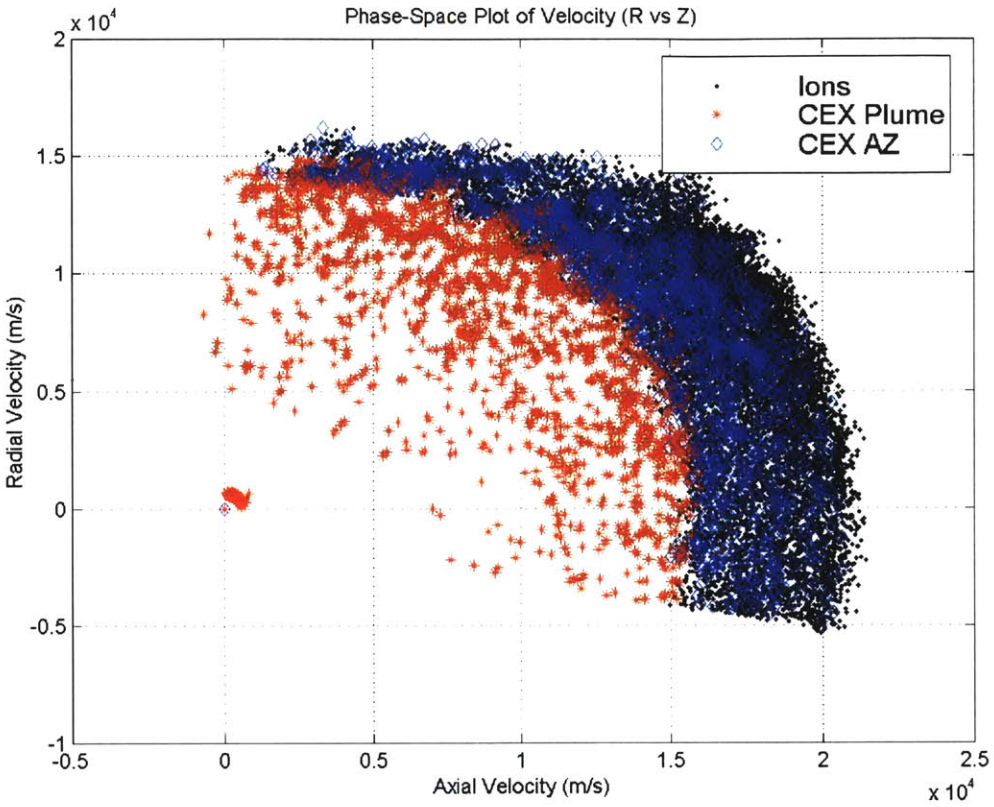

Figure 7.2: Velocity phase-space plot for ions in the plume.

The vast majority of ions were ionized inside the acceleration zone (AZ). However, all the low-speed ions (red star shapes) underwent charge exchange collisions. Also apparent in the figure is a dense band of particles with a total velocity near 15-20,000 m/s, the exhaust velocity of Hall thrusters.

The ions that underwent CEX collisions inside the acceleration zone are intermixed with those ions from normal ionization. It is unlikely that these CEX ions will be susceptible to the radial field like slower CEX ions found in the plume.

CEX ions make up a significant portion of low speed ions. The CEX ions appear to be the only ones that have negative axial velocities. The next figure shows the charge exchange ions alone. Many of these ions are being ejected radially from the plume. The small axial velocity will allow space potentials to draw them back into the spacecraft.

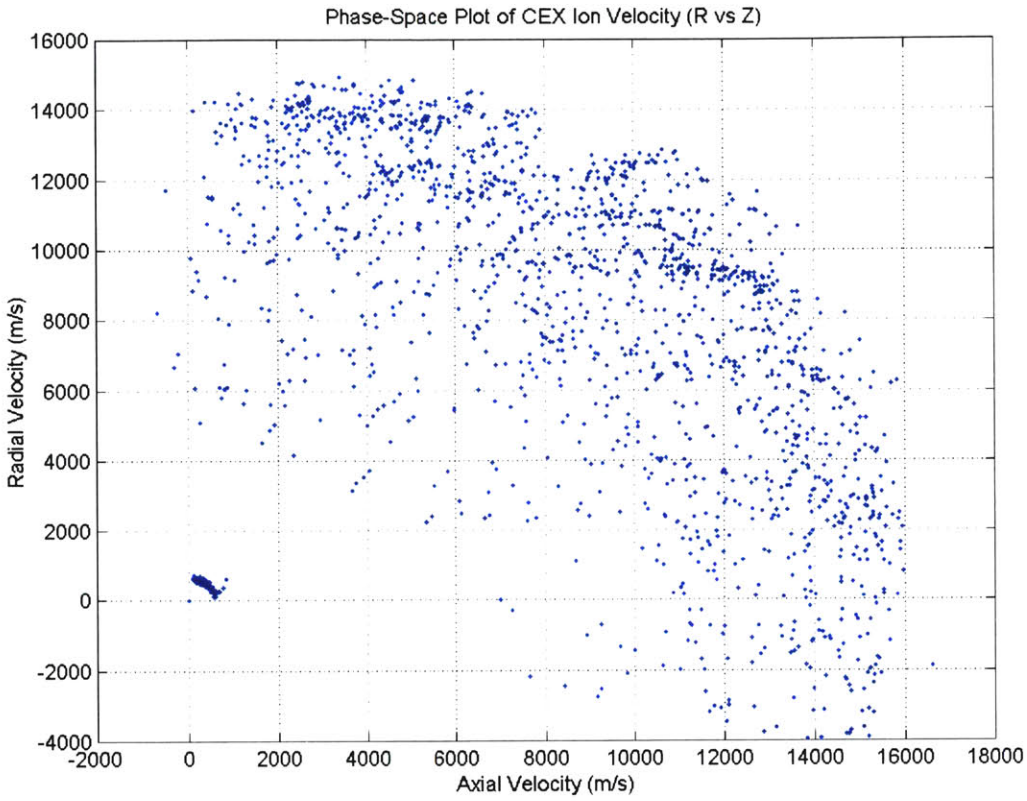

Figure 7.3: Velocity phase-space plots for CEX ions.

These plots only include those ions that leave the right-hand-side of the simulation. Ions can also enter the plume along the top boundary, extended from the exit plane, once they leave the acceleration zone.

7.3.3 Charge Exchange Ions in the Backflow Region

Ions travel through the top boundary (extension of the exit plane) of the simulation grid outside the acceleration chamber, directly heading towards the thruster, thruster mount and spacecraft. The type and velocities of ions crossing this boundary are plotted.

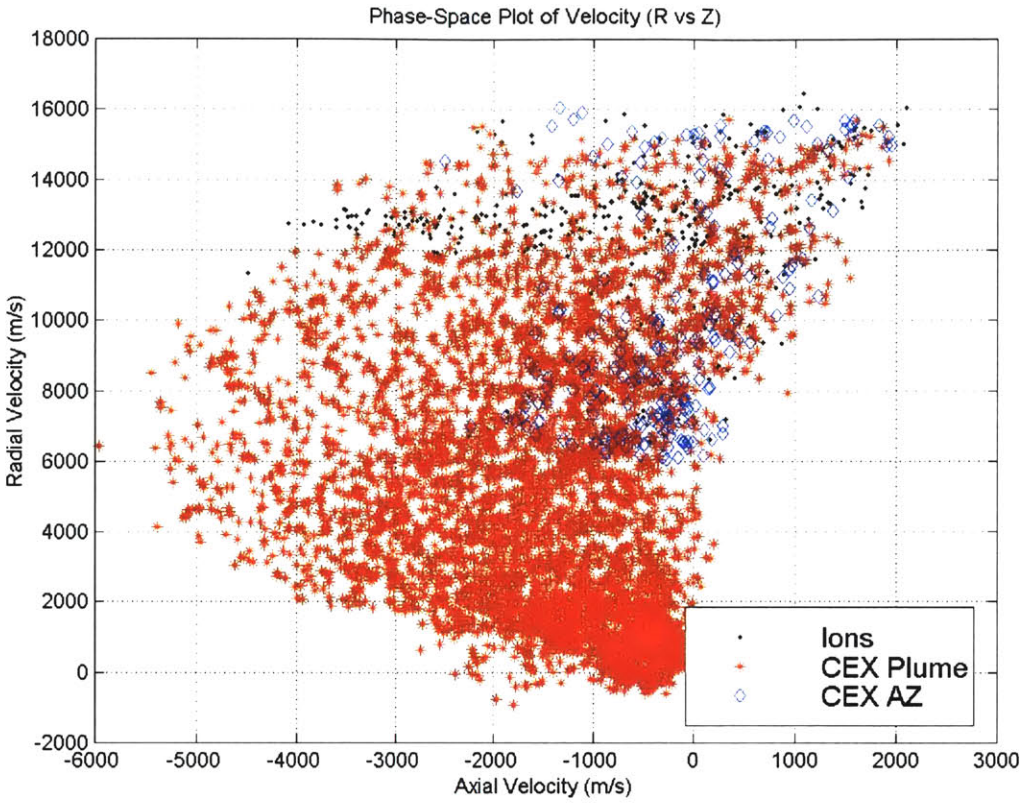

Figure 7.1: Velocity phase-space plot for ions in the back flow region.

In the back flow region, the charge exchange ions dominate. While some of these ions achieve fairly high axial velocities in the negative direction, the majority are moving radially. There is a minimum angle of about 35° to the backwards axial direction at which these ions travel as they leave the simulation. To determine where these ions are headed, the ion hit count is plotted verse radial distance from the thruster centerline. The following figure plots the number of "actual" ions (calculated from macro-particle mass) vs. the radial position at which they left the simulation.

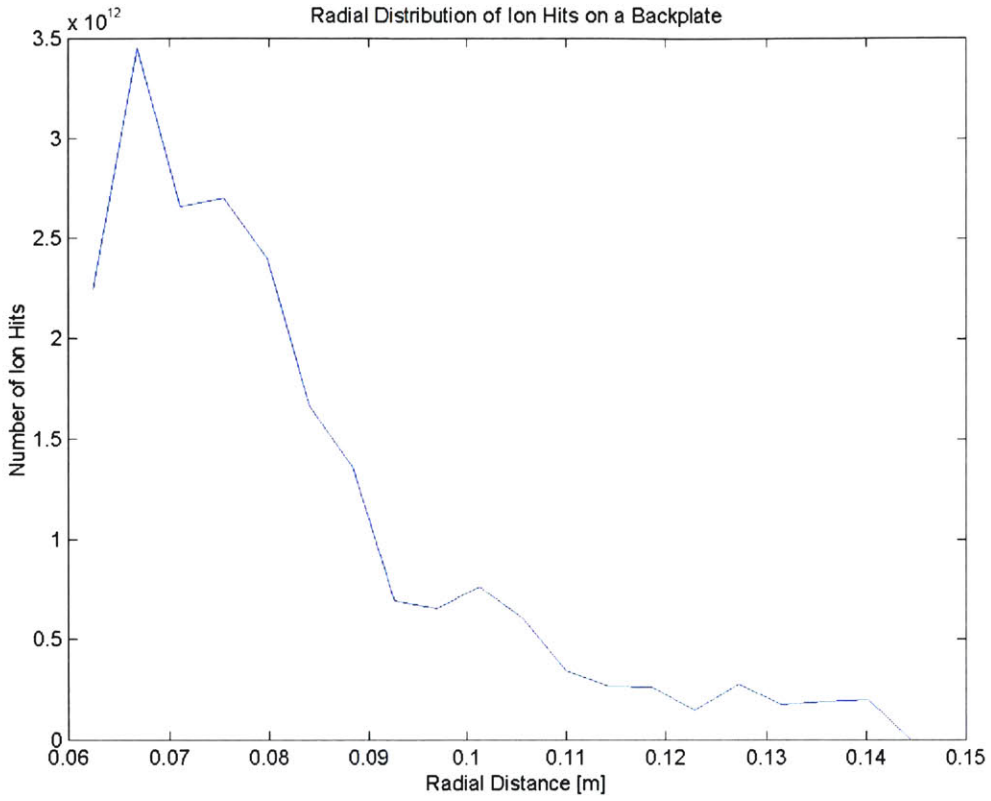

Figure 7.2: Distribution of ion hits along a radial "back plate." ($1.5x10^{-5}$ seconds)

According to the simulation results, the number of hits falls off by factor of 3 within the first 3 centimeters away from the outer edge of the thruster. For accurate experimental results, sensors should be placed fairly close to the engine itself.

The energy distribution of these ions, taken collectively, traveling backwards towards the spacecraft is plotted in the next figure. The energy peak is relatively low, as the only ions with a field of view of this region can only accelerate from outside the engine.

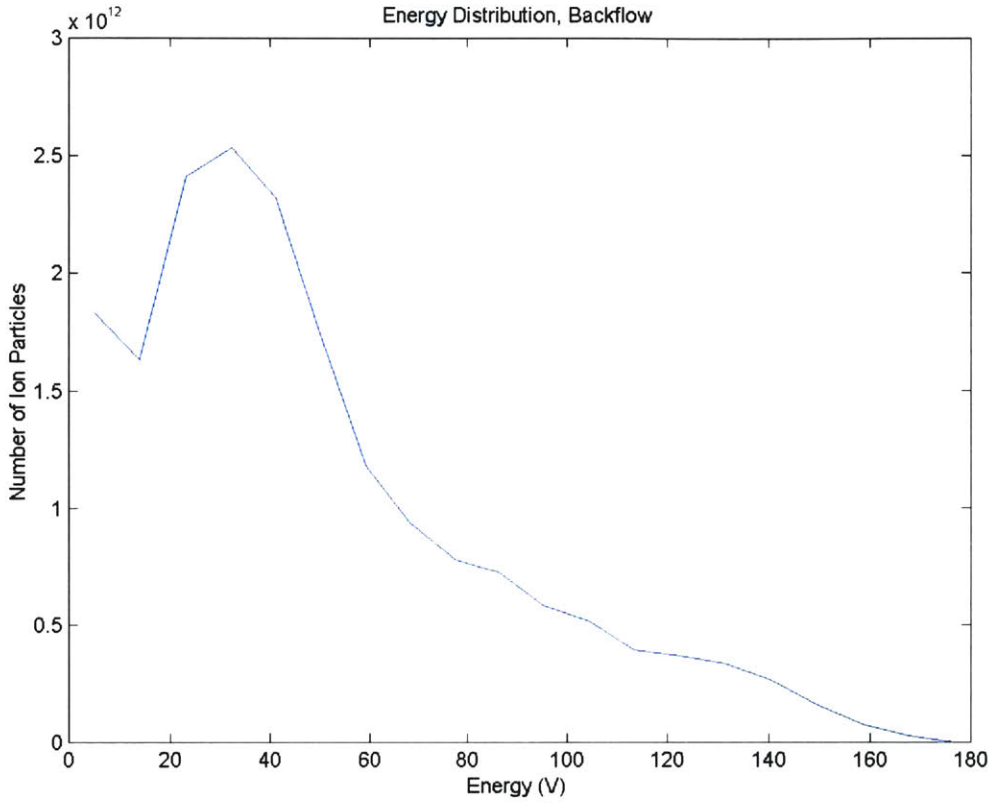

Figure 7.3: Energy distribution in the backflow region. ($1.5x10^{-5}$ seconds)

Most of the ions are created in the region of 25-50 volts of potential, found about 2.5-3 cm downstream of the engine exit, is a place with a relatively high rate of CEX collision, thus the prominence of CEX ions. Given that there is a minimum angle at which the ions are traveling, there is a shadowing effect in the backflow region behind the thruster, creating a natural shield around the structure of the engine itself.

7.3.4 Energy Distribution in the Plume

The following figures show the energy distributions as a function of divergence angle in the plume. Due to the geometry of the grid, the sample angles range from 7 to 84 degrees. Computations were not made in the backflow region to accurately estimate the angular energy dependence of these ions. The energies of all particles that cross the grid

were recorded over 150 iterations, or 0.75×10^{-5} seconds of real operation. Those ion hits can be plotted as a function of radial distance, as if they collided with a back plate.

As can be seen in the following figures, the energy peaks at about 250 V until one travels off axis. Then, the energy is much less, and a second prominent peak occurs. From the velocity plots, the low energy ions that form the second peak are primarily charge exchange ions.

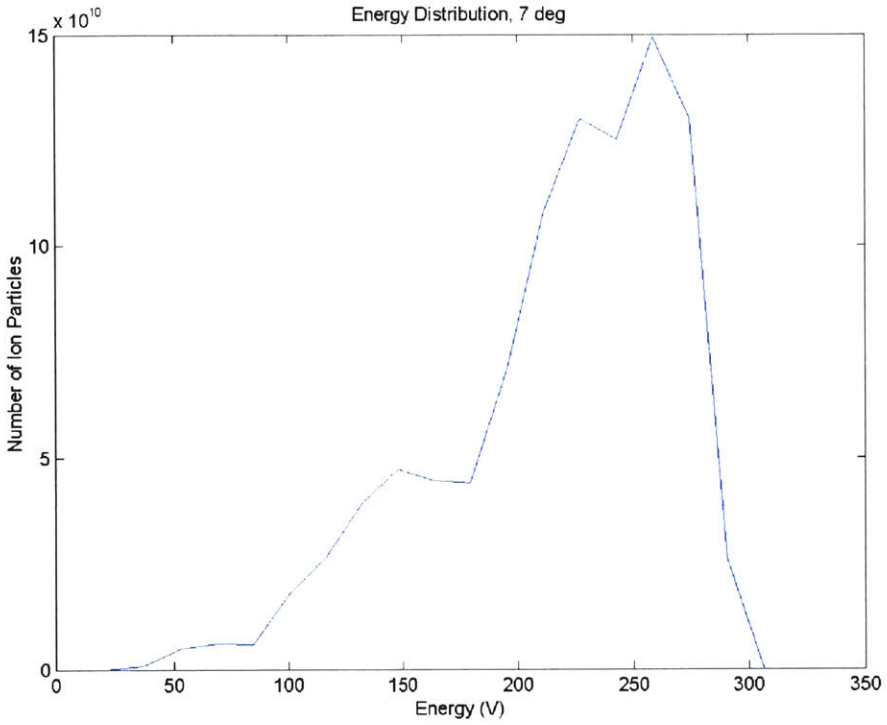

Figure 7.1: Plume energy distribution, 0-7° off-axis. [number of particles per cell]

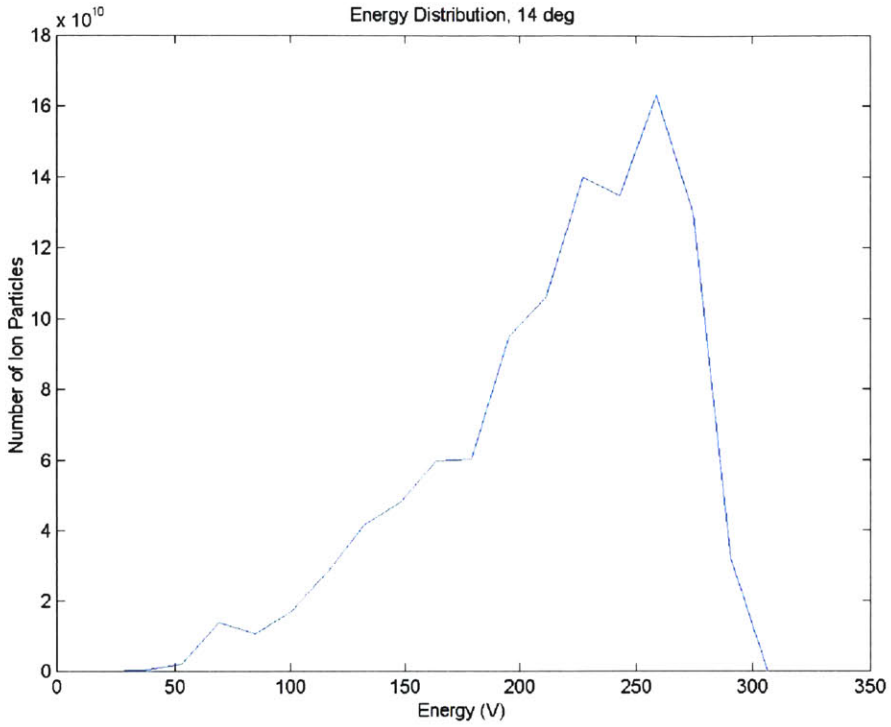

Figure 7.2: Plume energy distribution, 7-14° off-axis. [number of particles per cell]

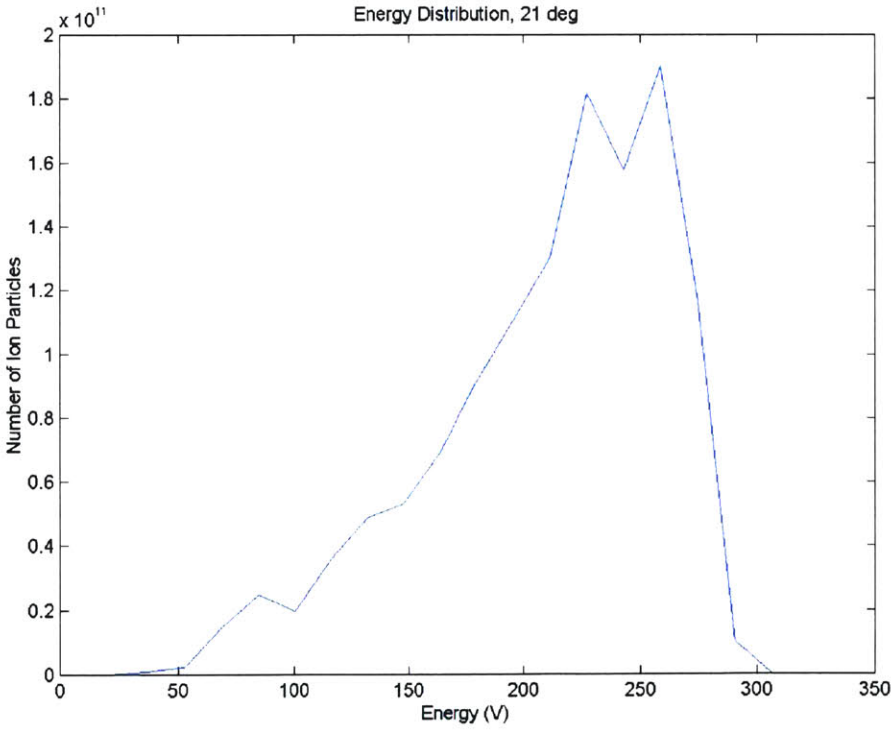

Figure 7.3: Plume energy distribution, 14-21° off-axis. [number of particles per cell]

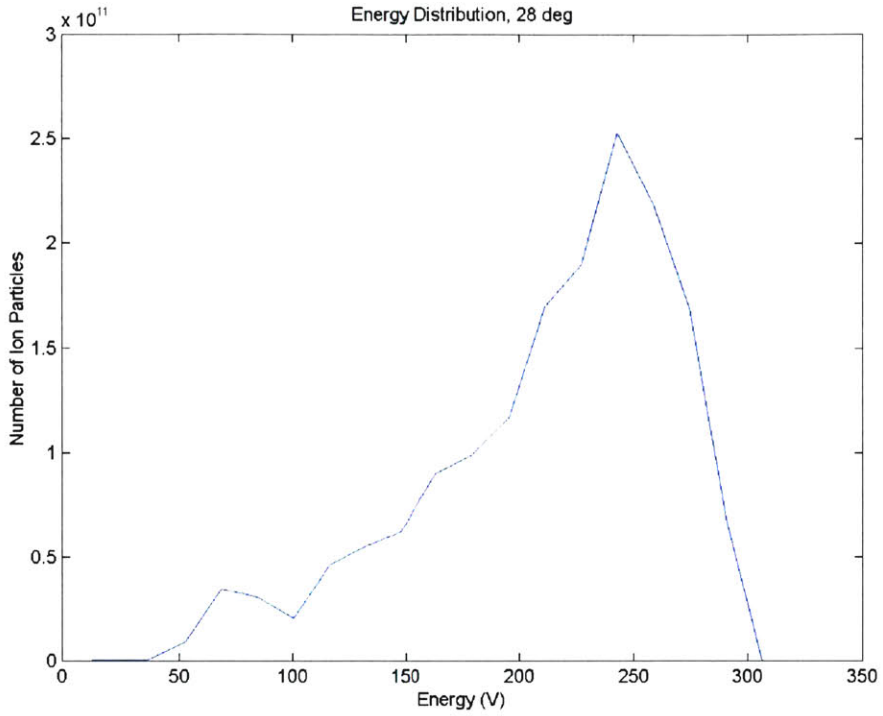

Figure 7.4: Plume energy distribution, 21-28° off-axis. [number of particles per cell]

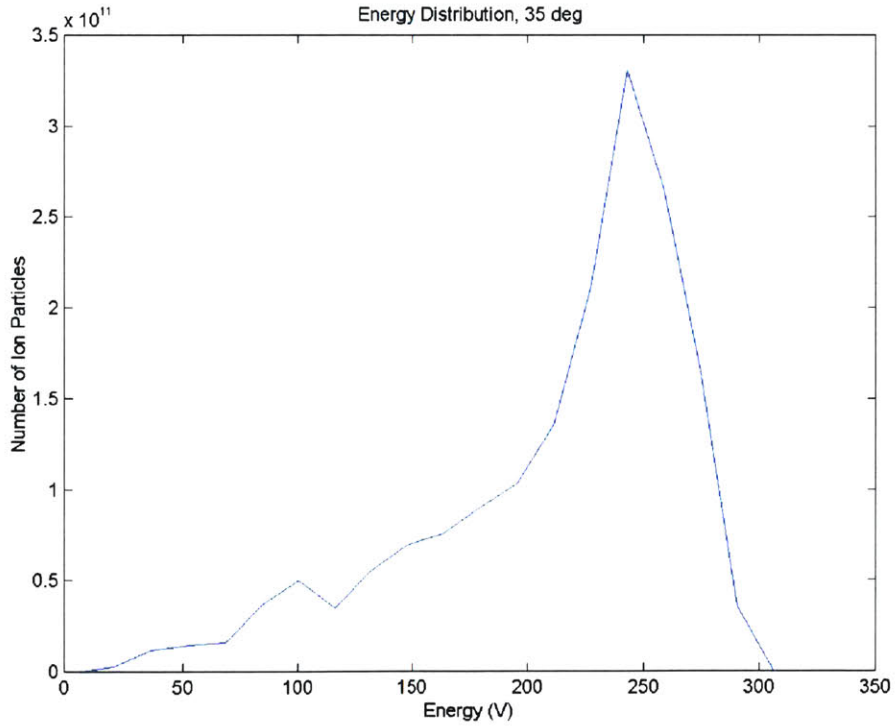

Figure 7.5: Plume energy distribution, 28-35° off-axis. [number of particles per cell]

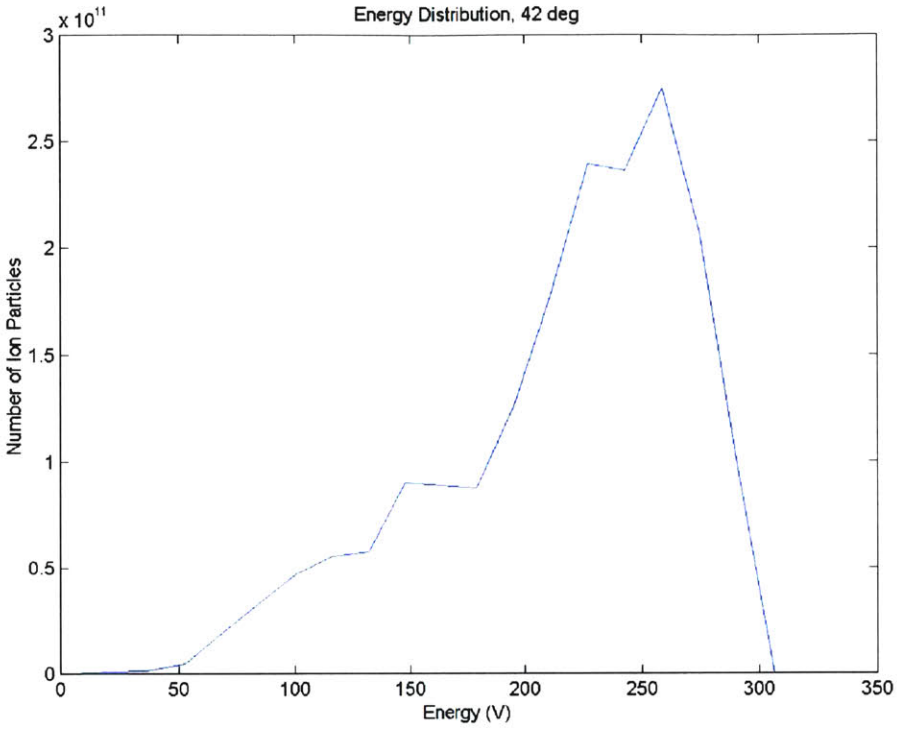

Figure 7.6: Plume energy distribution, 35-42° off-axis. [number of particles per cell]

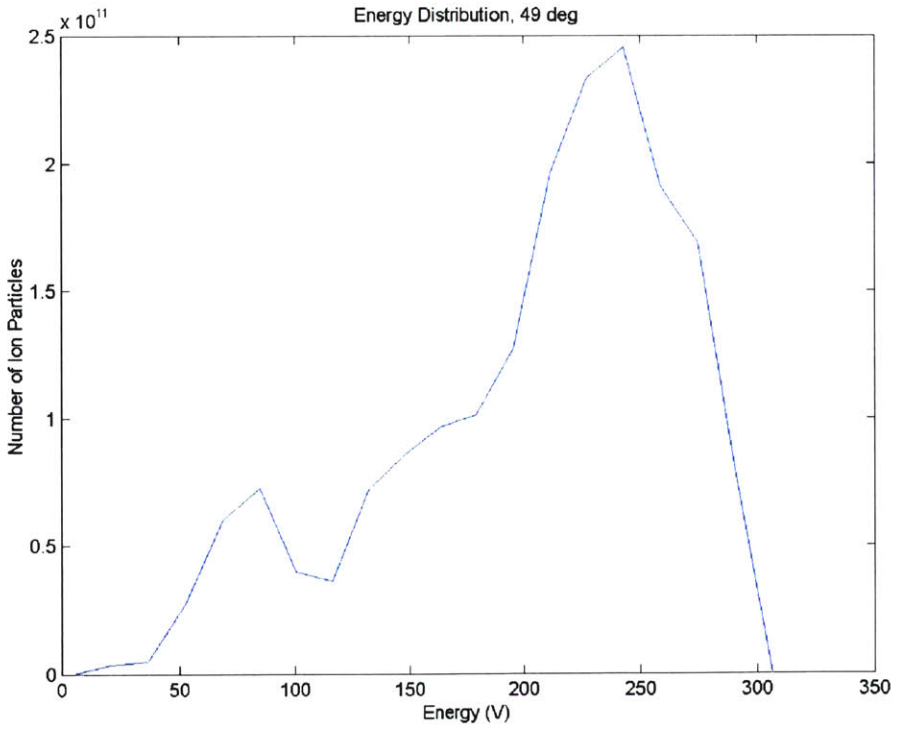

Figure 7.7: Plume energy distribution, 42-49° off-axis. [number of particles per cell]

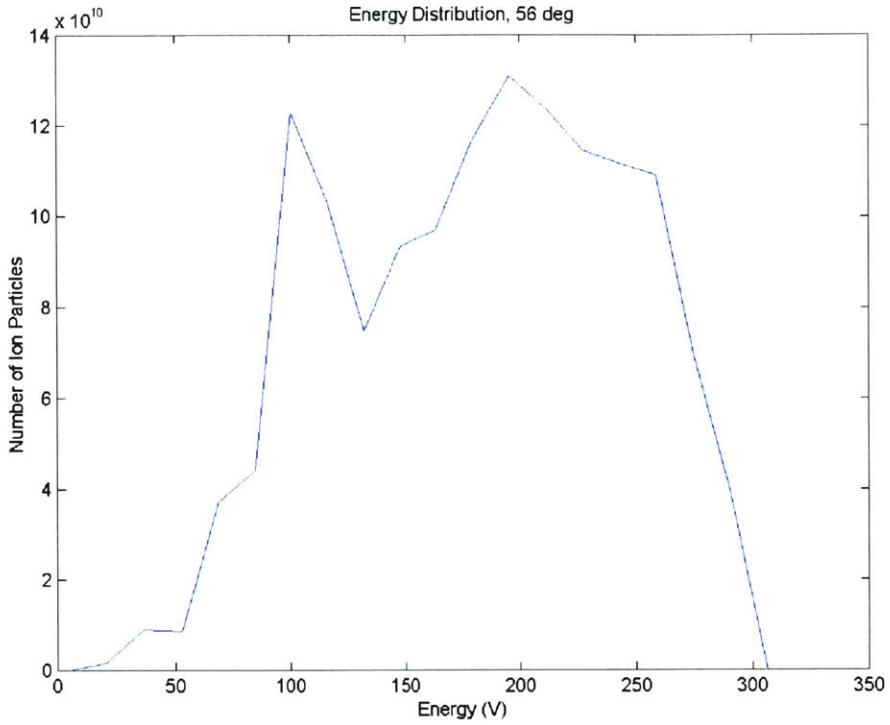

Figure 7.8: Plume energy distribution, 49-56° off-axis. [number of particles per cell]

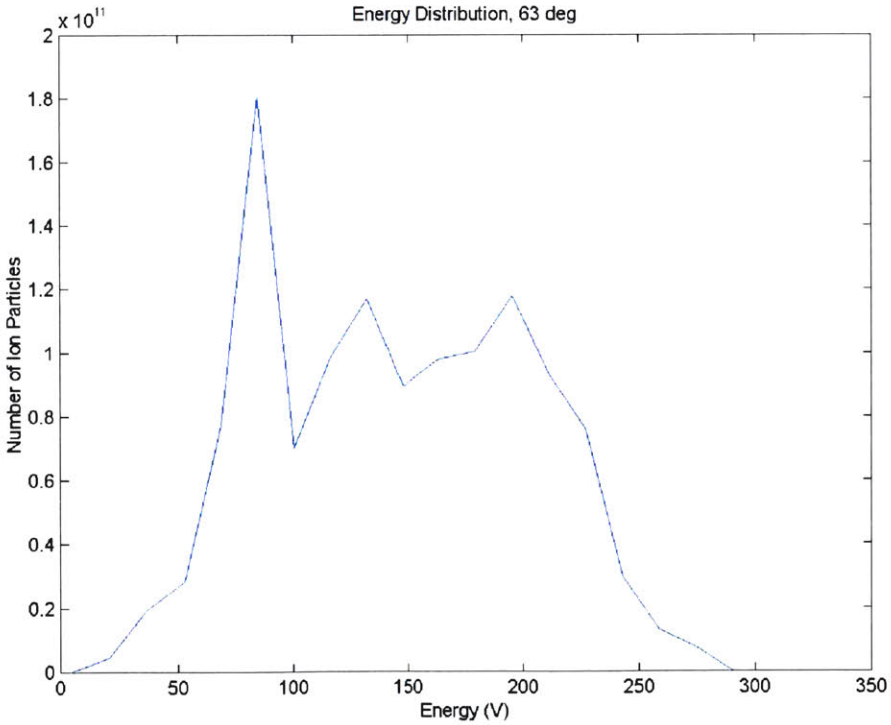

Figure 7.9: Plume energy distribution, 56-63° off-axis. [number of particles per cell]

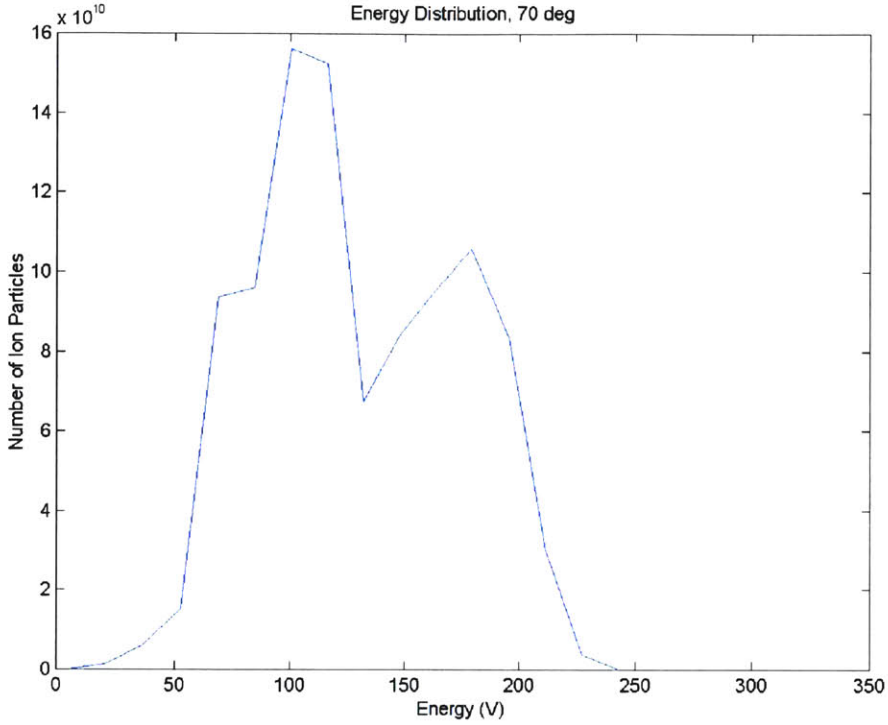

Figure 7.10: Plume energy distribution, 63-70° off-axis. [number of particles per cell]

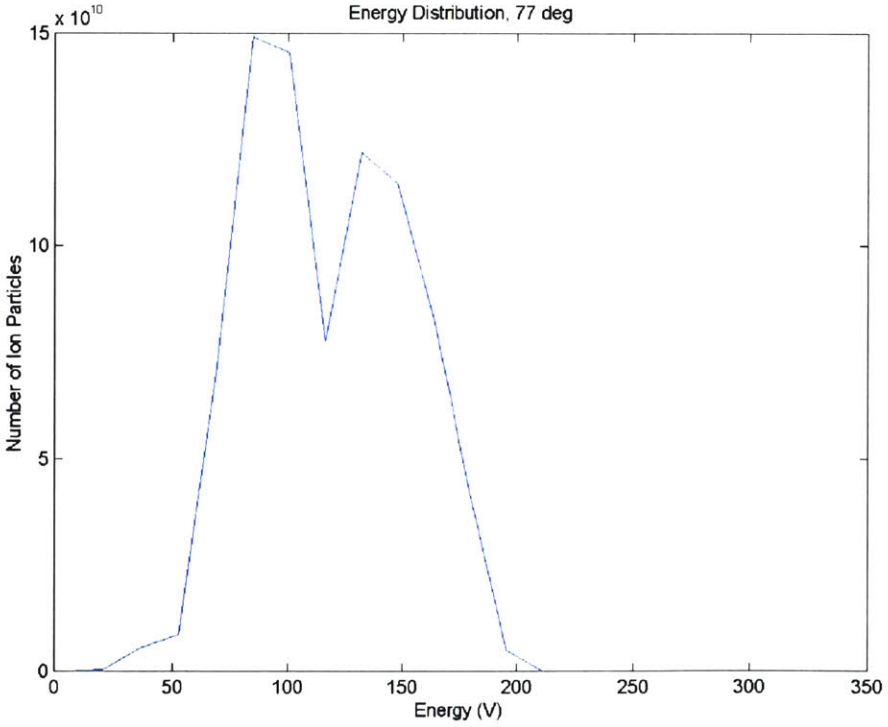

Figure 7.11: Plume energy distribution, 70-77° off-axis. [number of particles per cell]

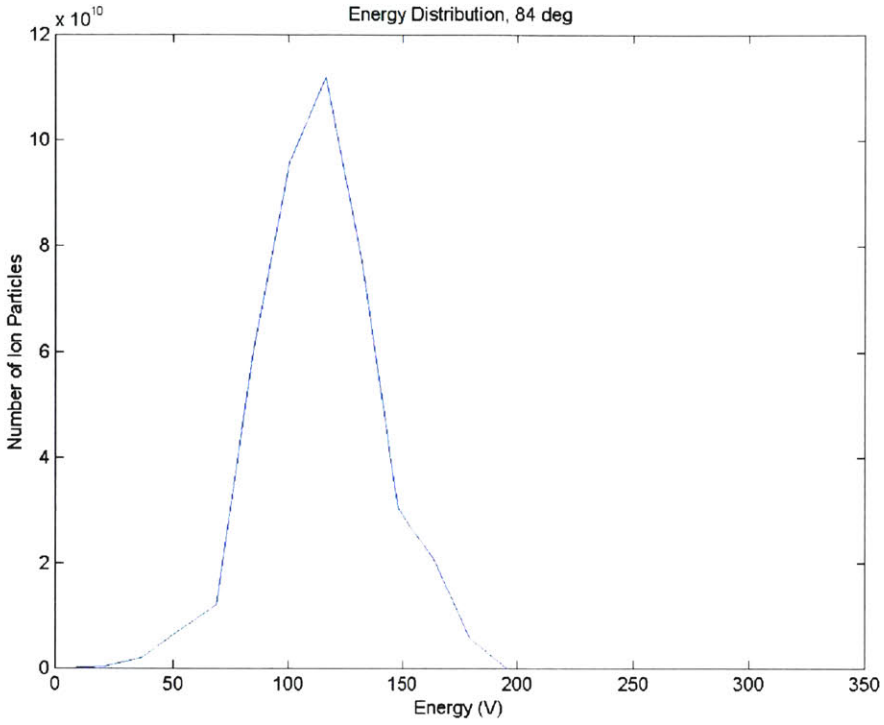

Figure 7.12: Plume energy distribution, 77-84° off-axis. [number of particles per cell]

Chapter 8: Conclusions and Recommendations

The three goals of the research are to:

- Calculate electron temperature and potential in the plume by solving the electron energy equations according to Fife's original algorithm, assuming zero net current in the plume.
- Expand the grid, extending the range of Fife's original simulation and use it to calculate unsteady performance characteristics in the plume region.
- Model the charge exchange process and study its effects on the simulation.

The following sections discuss the findings associated with each goal make recommendations for further research.

8.1 Net Current in the Plume

As previously explained, some attempts to match the temperature and potential profiles in the simulation were successful; however, as the simulation progressed the temperature and potential blow up at the boundaries. Attempts to revise the boundary conditions were unsuccessful. There is some relationship between the downstream potential distribution and the anode current oscillations that drives the anode current below zero. The mechanism to increase current as it drops below the nominal operating conditions is missing, once the current is set to zero in the plume, beyond the cathode.

The results of this work, therefore, make the same assumptions as Fife's original simulation concerning net current in the plume. Temperature is calculated up to the cathode, beyond which it is constant.

8.1.1 Recommendations

The magnetic field is so weak at the bounds of the current grid that assuming the electrons are isothermal along magnetic streamlines and conserving current may not be the best way to calculate temperature and potential in the plume. Other means for directly calculating the temperature should be researched. Continued work on Fife's algorithm, overhauling it to directly model the cathode may help. In this way, the calculation could be broken into two pieces, with boundary conditions applied separately.

The region just beyond the cathode is important to accurately model, as it is the location where CEX and ionization collisions occur most frequently in the plume. Efforts to calculate temperature and potential in this area should continue in the future. Fife's algorithm provides a unique starting point, but may need to be further revised to handle the changes.

8.2 Unsteady Plume Simulation Data

Expanding the grid seems to have no effect on the calculation of electron temperature, potential, or ion density in the near field plume or acceleration zone. The range of applicability extends as far as the assumptions about accurately modeling the magnetic field can be stretched.

The data recorded at locations downstream in the plume seem to confirm the predator-prey analogy for the low-frequency Hall thruster oscillations, although looking at the data on the scale of the speed of traveling ions is inconclusive. The ion density varies everywhere in the plume as batches of ions are formed in the engine and travel downstream. The amplitude of the oscillations die out as the distance downstream increases, due to the decreasing plasma density. The potential and temperature respond to these increases and decreases in ion density. The ionization rate adjusts to create more ions when the number density gets low, while the electric field increases when the density gets high. The increased electric field accelerates the new ions away more rapidly, decreasing the ion density again.

Additionally, even though no double ions were modeled, ions with speeds faster than the accelerating potential would allow can be found in the simulation. Wave-like features appear in unsteady data that travel faster than the standard ion velocity as well. It is unclear what these effects represent. Possibly, ions are riding wave fronts of potential, as the electric field fluctuates. These ions and waves may be able to obtain speeds faster than a normal accelerating potential would generate.

8.2.1 Recommendations

In order to study the traveling batches of ions throughout the engine oscillations, a more careful look must be taken. Oscillations, thought to be from the wall interaction model, make it difficult to track individual features on the scale of a single ion's travel time between locations. Some filtering and further reduction of the data may solve this problem. Additional modeling of the wall interactions may be necessary to understand the high speed oscillations in the Hall thruster simulation.

More careful tracking of individual ions could result in further understanding the process by which some ions have more energy than the accelerating potential would allow. These effects could be linked to high speed oscillations in potential from wall effects, or other phenomena.

Additionally, the simulation should be run, taking data in the plume with alternative geometries and different grids to look at other real engines and confirm the existing research. Just expanding the grid for an SPT-100 did not seem to have any effect on the simulation of performance. However, other geometries may be more effective at studying plume effects and interactions.

8.3 Effect of Charge Exchange Collisions

As modeled in this simulation, charge exchange collisions seem to have little effect on the overall engine operation and performance characteristics. One significant difference is the increase in potential outside the acceleration zone. Ions, which would normally speed away from the exit plane, after accelerating are instead slowing down (slow neutrals are being ionized). The creation of a cloud of slow ions locally increase the ion density and increases the potential. Ions created outside the acceleration zone, through CEX or ionization collisions, have a stronger radial electric field through which to accelerate.

The CEX collisions increase the number of low speed ions in the plume. In particular, these ions have very low axial velocity, but may have higher radial velocities. These ions are kicked out of the plume and may collide with spacecraft components. CEX ions were the most prominent in the back flow region, the side of the simulation open to the spacecraft. It is also worth noting that the density of ion "hits" in that region rapidly falls off with radial distance from the engine. The potential contours do not extend that far in the radial direction, so ions with negative axial velocities accelerating in the this regime will stay relatively close to the acceleration zone. Other ions will be kicked out with relatively large radial velocities.

In studying the energy distribution data, it is clear that Fife's simulation, even extended to the theoretical bounds of the magnetic field strength, still shows the properties of a near-field flow from an annulus. This makes it difficult to match experimental data taken from much farther away. Continuing to extend this geometry, modeling the thruster as an axisymmetric annulus, may not be as accurate as other plume simulations in predicting distributions of beam current and energy.

However, Fife's simulation does show the presence of both low and high energy ions at locations off the main thrust centerline. As the angle off-axis increases, the distribution smears out, and the energy decreases. However, some high energy ions can be found at angles greater than 80°, reiterating previous experimental work. The research by King et al.[1998] shows a very prominent peak at 200 V for angles greater than 90. This peak is

not present, even though the potential lines have moved further outside the engine with the presence of the CEX ions.

8.3.1 Recommendations

The existing simulation only contains singly charged Xenon ions. The CEX collision process should be modeled with Xe^{+2} to get better results. The extra charge on the Xe^{+2} allows those ions to accelerate to greater speeds, making them more dangerous to spacecraft components.

The effect of "shadowing" in the back flow region was briefly discussed in the results section; however, more work should go on in the area. The largest number of ions in the back flow region cross over very close to the engine, where the electric field is still strong. These ions have some minimum angle, but may still hit spacecraft components. Other research, using David Oh's simulation has looked at shielding around the exit of a Hall thruster [Asare, 1999]. These results seem to indicate that further work towards filtering out the high speed ions near the engine mount itself could prove beneficial.

Finally, verification of these simulated results should come from more experimentation. There is some disagreement in the available data concerning the shape of the potential contours and temperature in the plume. Continued correlation with experimental data is necessary to use Fife's code as a design tool.

Chapter 9: References

1 Absalamov, S.K., Andreev, V.B. et al. "Measurement of Plasma Parameters in the Stationary Plasma Thruster (SPT-100) Plume and its Effects on Spacecraft Components." AIAA-92-3145, July 1992.

2 Asare, B. "Computational Modeling of Expanding Plasma Plumes in Vacuum and in a Tank." Master's Thesis, Massachusetts Institute of Technology, Department of Aeronautics and Astronautics, September 1999.

3 Birdsall, C.K., and Langdon, A.B. "Plasma Physics via Computer Simulation." Adam Hilger, Bristol, 1991.

4 Fife, J.M. "Two Dimensional Hybrid Particle-in-Cell Modeling of Hall Thrusters." Doctoral Thesis, Massachusetts Institute of Technology, Department of Aeronautics and Astronautics, 1998.

5 King, Lyon B. and Alec Gallimore. "Ion Energy Diagnostics in the Plume of an SPT-100 from Thrust Axis to Backflow Region" AIAA-98-3641, 34th AIAA/ASME/SAE/ASEE Joint Propulsion Conference and Exhibit, Cleveland, OH, July 13-15, 1998.

6 Lubachevsky, B.D. "How to Simulate Billiards and Similar Systems." Journal of Computational Physics, vol. 94, 1991. Pp. 255-283.

7 Manzella, D.H. "Stationary Plasma Thruster Plume Emissions." AIAA-93-097, 23rd International Electric Propulsion Conference, Seattle, WA, September 13-16, 1993.

8 Oh, D.Y. "Computational Modeling of Expanding Plumes in Space Using a PIC-DSMC Algorithm." Sc.D. Thesis, Massachusetts Institute of Technology, Department of Aeronautics and Astronautics, 1997.

9 Qarnain, S. "Issues Regarding a Complete Computational Model of a Hall Thruster from the Acceleration Channel through the Plume." S.M. Thesis. Massachusetts Institute of Technology, Department of Aeronautics and Astronautics, May 1998.

10 Samanta Roy, R.I. and D.E. Hastings. "A Review of Contamination from Electric Propulsion Thrusters." AIAA 94-2469. 25th AIAA Plasma dynamics and Lasers Conference, Colorado Springs, CO, June 20-23, 1994.

11 Szabo, James J., Manuel Martinez-Sanchez, and Jeff Monheiser. "Application of 2-D Hybrid PIC Code to Alternative Hall Thruster Geometries." AIAA 98-3795, 34th AIAA/ASME/SAE/ASEE Joint Propulsion Conference and Exhibit, Cleveland, OH, July 13-15, 1998.

12 VanGilder, D.B., Keidar, M., Boyd, I.D. "Modeling Hall Thruster Plumes Using Particle Methods." AIAA-99-2294, 35th AIAA/ASME/SAE/ASEE Joint Propulsion Conference and Exhibit, Los Angeles, CA, June 20-24, 1999.

Appendix A: Unsteady Data with CEX

The following data plots are a record of the unsteady simulation calculations at the virtual probe locations for a simulation with CEX collisions present.

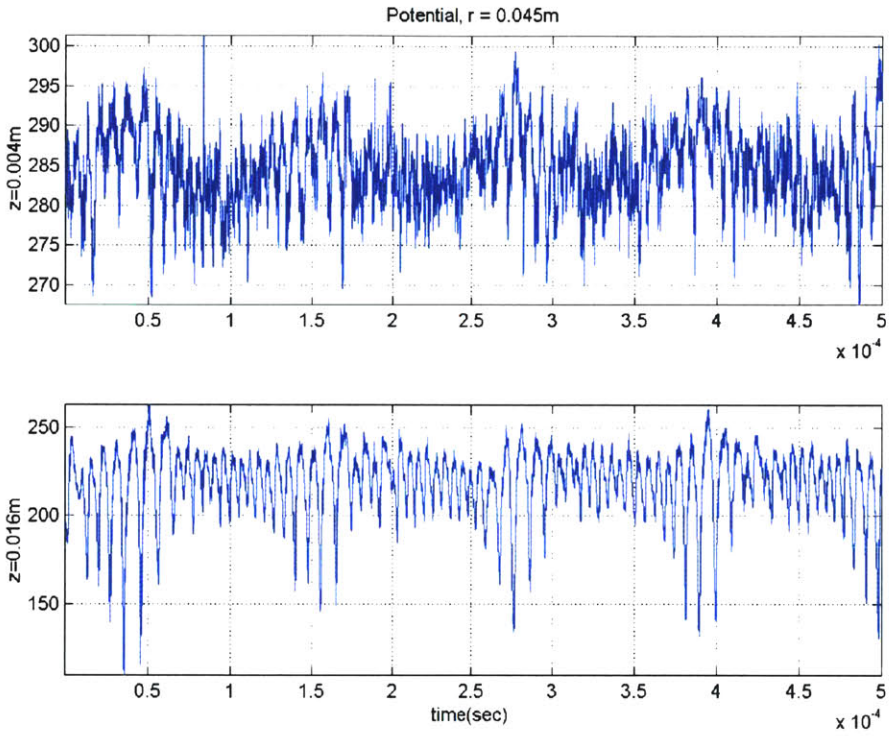

Figure A.1: Potential vs. time in the acceleration zone, both axial stations shown.

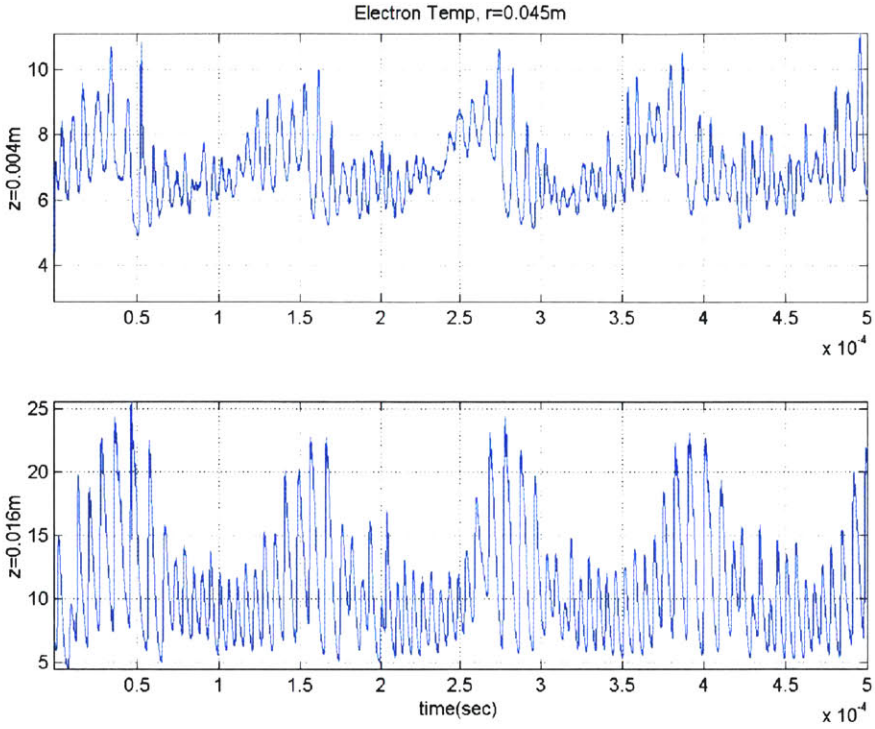

Figure A.2: Electron Temperature vs. time in the acceleration zone.

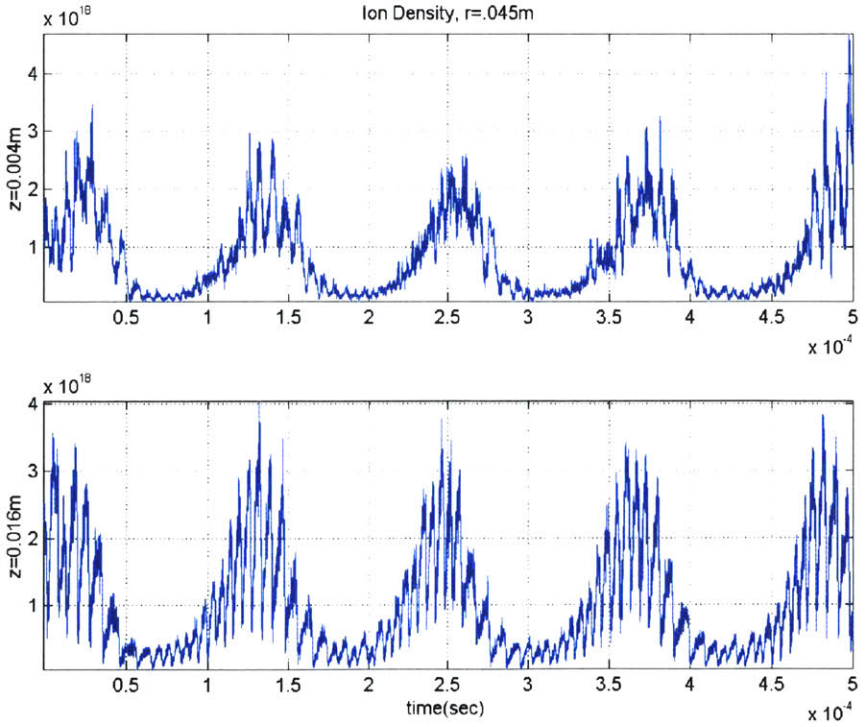

Figure A.3: Ion density in acceleration zone.

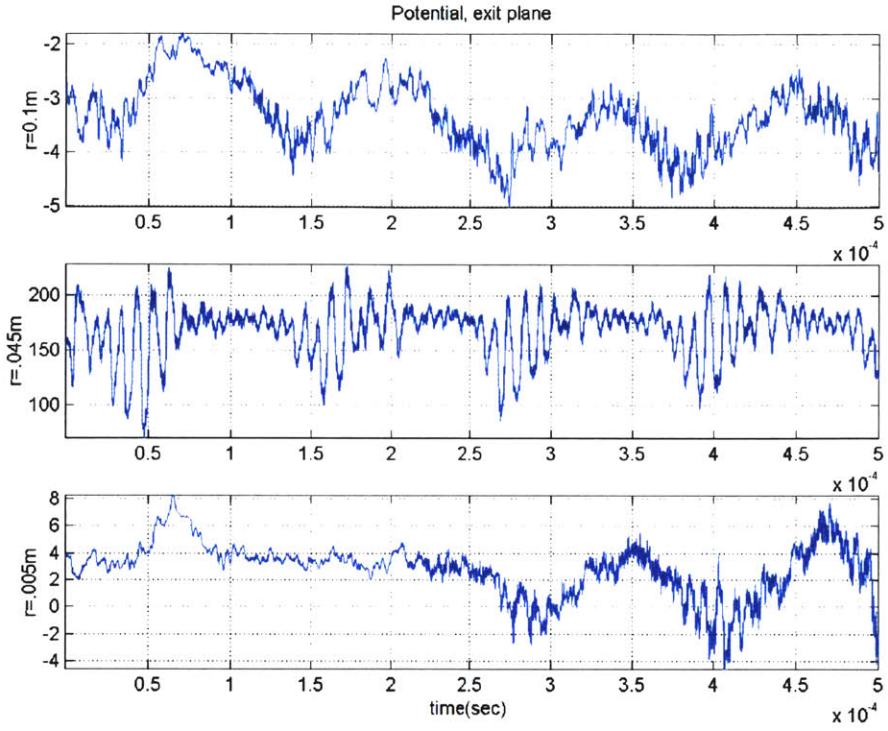

Figure A.4: Potential at the exit plane.

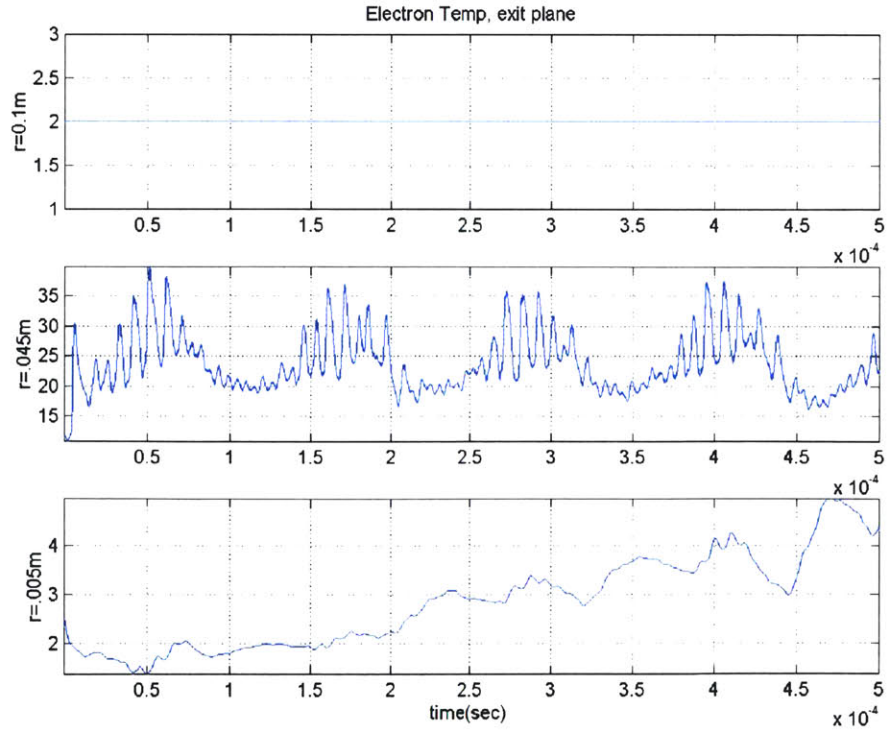

Figure A.5: Electron temperature at the exit plane.

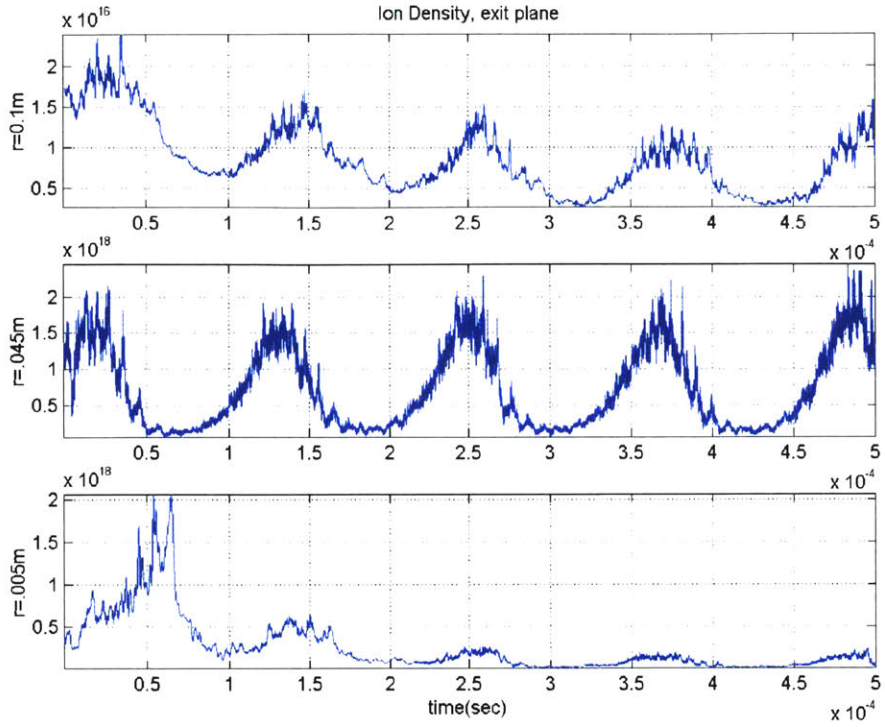

Figure A.6: Ion density at the exit plane.

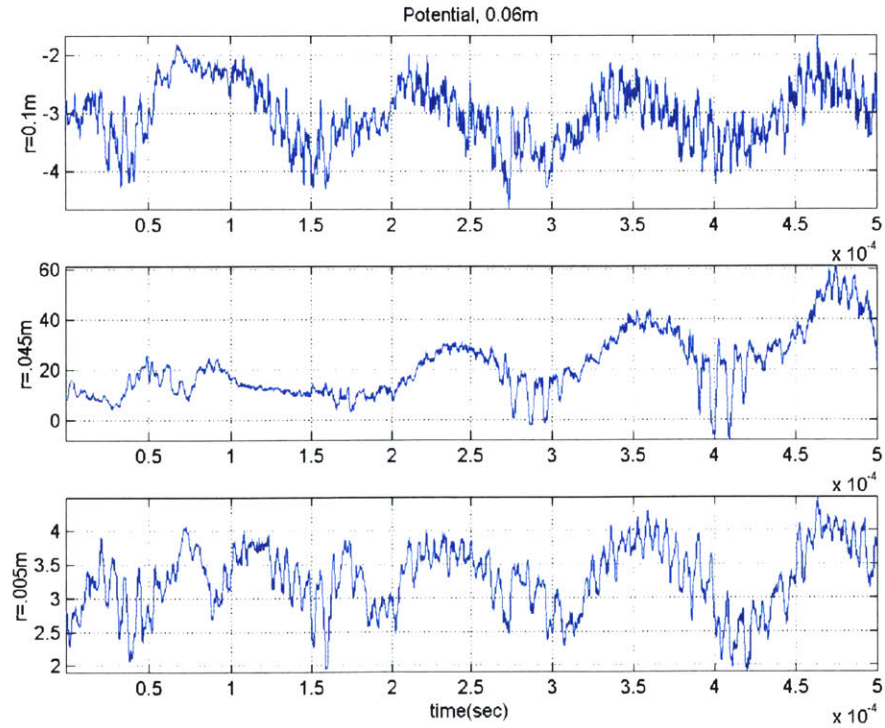

Figure A.7: Potential, 0.06 m from the anode.

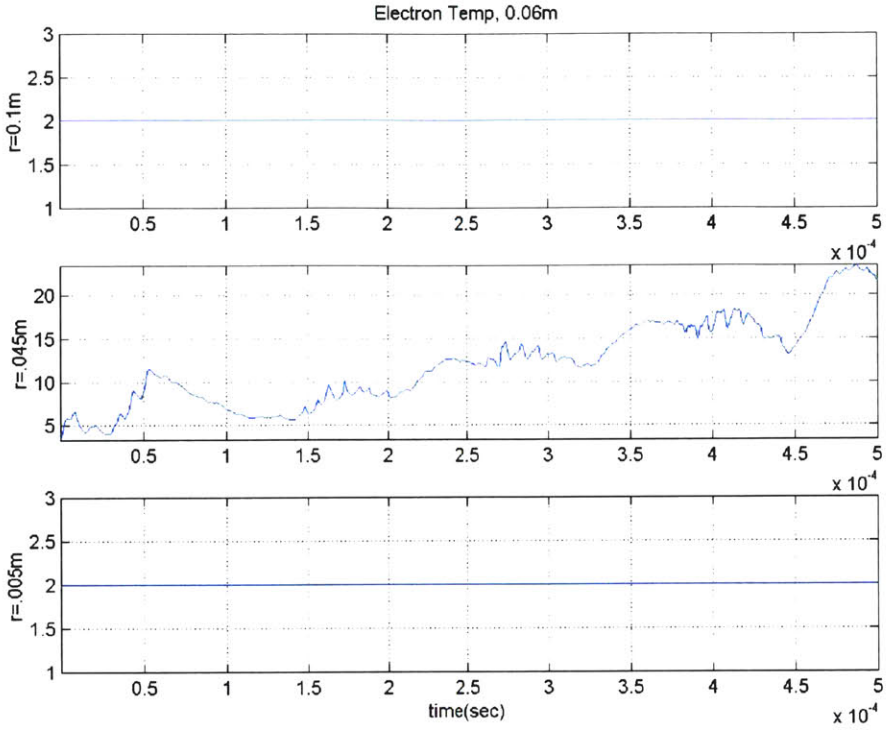

Figure A.8: Electron temperature 0.06m from the anode.

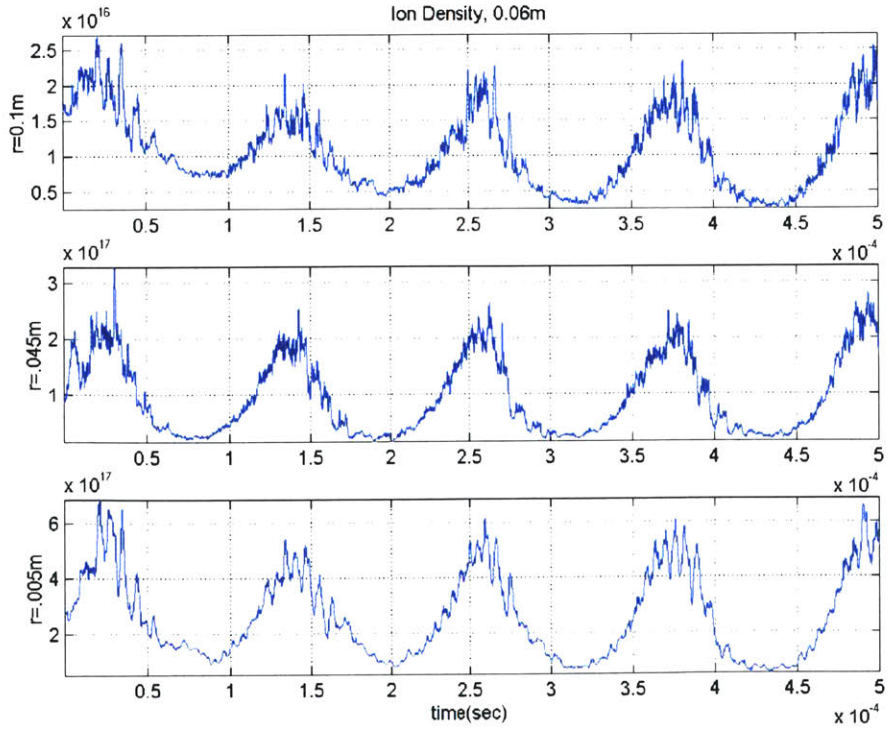

Figure A.9: Ion density 0.06 m from the anode.

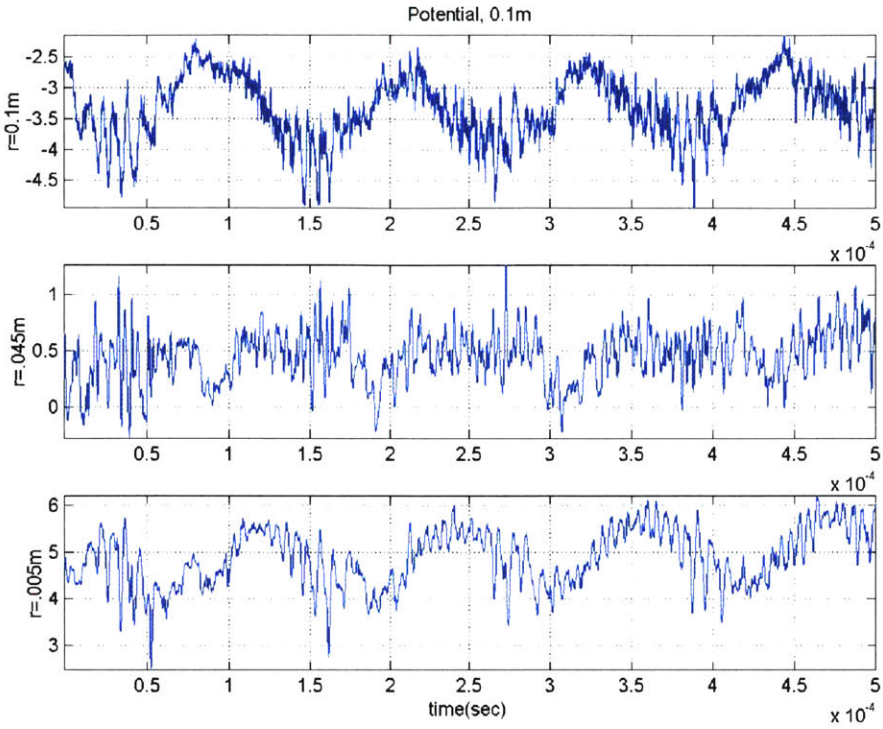

Figure A.10: Potential, 0.1 m from the anode.

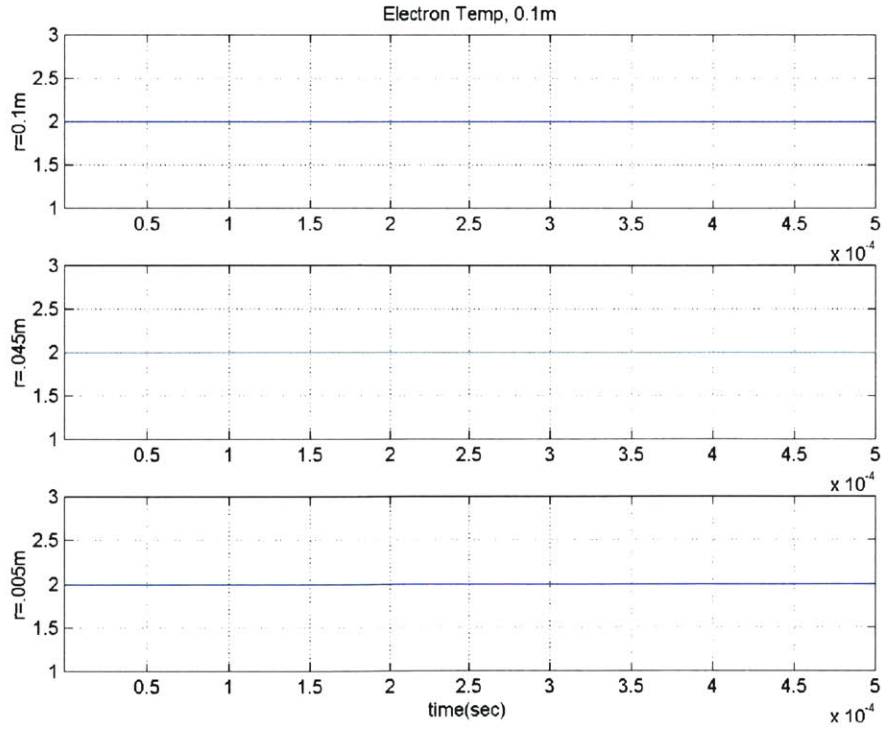

Figure A.11: Electron temperature, 0.1 m from the anode.

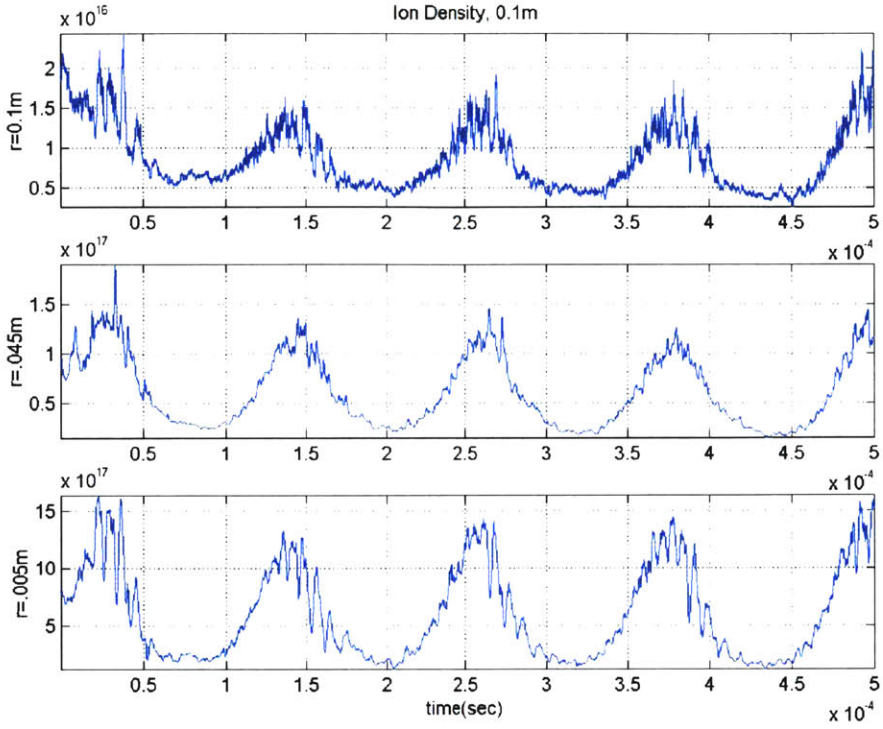

Figure A.12: Ion density, 0.1 m from the anode.

Appendix B: Sample Input Files

Running Hall requires three main sets of input values. A printout of the values used in the above work is included in this appendix. The three input files are "geo.in," which controls the geometry of the magnetic poles and is required for the magnetic field solver. The main program runs using values from "hall.h." Another file, "picin.h" contains identical variables, so both must be updated when changing a value. The final file, "a.inp" is written for specific cases and allows an operator to change some parameters without recompiling the code. Changes to other inputs require recompilation.

geo.in

```
-.08 .5 .5 200 200        # z_min, z_max, r_max, n_r, n_z
350.0                     # initial guess
.0179 .0422               # B-field reference point z-r coorinates
3
.0200 0.0 .0250 .0294 0.0
-.060 0.0 -.055 .0800 205.0      # 205 windings
.0154 .0550 .0204 .0800 545.0  # 4 coils of 85 windings each
2
-.055 0.00 .0200 .0200 205.0 0.0
-.055 0.0700 .0154 .0800 205.0 545.0
0
```

hall.h

```
/*=========================================================================
 * hall.h

*=========================================================================*/


/*-------------------------------------------------------------------------
*/
/* Some physical constants */
/*-------------------------------------------------------------------------
*/
#define PI                3.141593  /* pi */
#define EPSILON           1e-5      /* small number on xi-eta scale */
#define EPSILON2          1e-4      /* slightly larger on xi-eta scale
*/
```

```
#define K                1.38e-23   /* Boltzmann's constant */
#define E                1.602e-19  /* charge on one electron (C) */
#define MASS_ELECTRON     9.11e-31  /* mass of an electron (kg) */
#define G                9.80665    /* acceleration of gravity */


/*-------------------------------------------------------------------
*/
/* Select the thruster geometry and propellant type  */
/*-------------------------------------------------------------------
*/
#define GEOMETRY             SPT_100
#define PROPELLANT           XENON


/*-------------------------------------------------------------------
*/
/* Set some physical constants based strictly on the type of propellant
*/
/*-------------------------------------------------------------------
*/
#if (PROPELLANT==XENON)
/*--------------------------------------*/
#define E_I               1.94e-18     /* ionization energy (joules)
#define MASS_ION         2.18e-25      /* mass of a xenon ion (kg) */
#define CHARGE_PER_MASS (E/MASS_ION) /* charge-to-mass ratio for ions
*/
#define Q_LENTZ          4.13e-13      /* ionization parameter which
                                          depends upon the species --
#define Q_CONST           1.77e-19     /* ionization constant -- see
#define B1               1.0           /* 1.0 ionization constant
#define B2               0.85           /* 0.8 Lentz, .85 Szabo */
#define LOSS_A            0.254        /* from loss coefficient curve
fit */
#define LOSS_B            0.677        /* "" */
#define LOSS_C            2.0          /* "" */
#define ACCOMMODATION_I    0.80     /* thermal accommodation coeff for
ions */
#define ACCOMMODATION_N    0.80     /* thermal accommodation for
neutrals */


/*-------------------------------------------------------------------
*/
/* Constants relating to physical properties of specific geometries  */
/*-------------------------------------------------------------------
*/

#elif (GEOMETRY==SPT_100)

#define K_INJ_MIN          8        /* 8 injector bounds for ion_n() */
#define K_INJ_MAX         15        /* 15 injector bounds for ion_n()
*/
#define WALL_END_1_J      47      /* xi node at which inner wall ends
*/
#define WALL_END_2_J      28      /* xi node at which outer wall ends
*/
```

```
#endif


#define DELTA              0.6      /* secondary emmission coefficient
*/
#define T_WALL              900      /* dielectric wall temperature */
#define T_N_INJ           1000.0   /* temp of the injected neutrals (K)
*/

#define REFLECT_THRESHOLD .0025     /* r threshold for reflections */

#define SECONDARY_A        0.11    /* fit for secondary electron
emission */
#define SECONDARY_B        0.576    /* fit for secondary electron
emission */


/*---------------------------------------------------------------------
*/
/* Mass flow rate */
/*---------------------------------------------------------------------
*/
extern float M_DOT_AEQ;          /* 0.439 Amps */
                                 /*  mass flow rate in amp-equivalents
*/
extern float M_DOT;
                                 /*  mass flow rate in kg/s */
extern float I_A_0;              /* Nominal value of anode current
(Amps).
                                    This will usually be very close to
                            M_DOT_AEQ. */



/*---------------------------------------------------------------------
*/
/* Definitions for hall.c -- Program control flow  */
/*---------------------------------------------------------------------
*/
extern float DT;
extern float NEUTRALS_PER_DT;     /* 2.0/20 number of neutrals created
per dt
                             at the anode*/
#define T_E_RATIO         1000   /* ratio of the ion timestep to t_e */

#define IONS_PER_DT       10.0    /* number of ions created per dt at
                                     the anode */
extern float MASS_WALL_NEUTRALS;       /*
(M_DOT_AEQ/E*DT*MASS_ION/NEUTRALS_PER_DT/.5) */
                                 /* mass of neutrals produced at the
                              wall from recombination
                              -- same as injected mass */
#define ION_3_V           0      /* 2-V (0) or 3-V (1) ions? */
#define ION_NEUTRAL_COLLISIONS  0   /* ion-neutral collisions y/n 0/1
*/
#define RECOMBINE_BULK           0   /* recombine ions to neutrals
                                in bulk? 1/0 */
```

```
#define RECOMBINE_WALL   1      /* recombine ions to neutrals at wall?
1/0 */
#define PHI_TOLERANCE    2.0    /* tolerance of anode potential */
#define CONST_PHI_RELAX  1.0    /* relaxation parameter for phi-I
                                  convergence */
#define AVERAGE          1      /* average output over time */

#define ION_DIST_PLUME   0      /* store a z and r distribution of ion
                                   energies from the plume? */
#define PLUME_IONS     0     /* Records ions that leave the simulation
                          for plume analysis */
#define ION_TRACE        0      /* trace an ion? */
#define ION_TRACE_XI        32.0
#define ION_TRACE_ETA        5.0
#define ION_TRACE_V_Z        0.0
#define ION_TRACE_V_R        0.0
#define ION_TRACE_V_THETA  200.0
#define ION_TRACE_MASS  5.0e-18
#define NEUTRAL_TRACE        0      /* trace a neutral? */
#define NEUTRAL_TRACE_XI           2.0
#define NEUTRAL_TRACE_ETA          8.0
#define NEUTRAL_TRACE_V_Z        250.0
#define NEUTRAL_TRACE_V_R        -50.0
#define NEUTRAL_TRACE_V_THETA    200.0
#define NEUTRAL_TRACE_MASS     7.0e-15
extern int SAVE_ITS;            /* save data every SAVE_ITS iterations
*/
#define CHAMBER_PRESSURE 0      /* simulate chamber pressure?
                           if not, the next 3 quantites are
                           meaningless */
#define CHAMBER_N_PER_PANEL  .077  /* .077/.77 neutrals per timestep
per panel
                             from chamber */
#define PHI_EPS        .01      /* small value of discharge potential
*/
#define STD_OUTPUT     VERBOSE  /* If "Hush" prints out only a few
parameters
                                   to screeen.  If "Verbose" prints out
more
                           -JS, 12/4/97 */
#define ELECTRIC_OUTPUT VERBOSE  /* applies to function electric() in
hall.c */

/*---------------------------------------------------------------------
*/
/* Definitions for electron.c  */
/*---------------------------------------------------------------------
*/
#define LOSS_CONST       1.0        /* 3.5? */
                                    /* coeff for electron energy loss
term */
#define D_FAC            1.0        /* heat conduction coefficient
factor.
                                       Diffusion seems high, so this
factor
                              may be used to reduce it.  This
                              is probably the case since the
```

```
                                mechanism of Bohm diffusion
                                is not responsible for the heat
                                diffusion to the same degree as it is
                                for electron conductivity */
#define PHI_CATHODE      0.0        /* cathode potential (reference) */
#define T_E_ANODE       1160.0       /* anode electron temperature (.1
eV) */
#define IONIZ_CONST       1.0        /* constant factor of ionization
rate */
#define LAMBDA_CATHODE   2.8e-5      /* cathode position (set large to
                                let code determine it) or, set it
                                to what you want (1.8e-5 for SPT-100
                                to miss metallic center piece) */

/* This will vary with the thruster.  You must look at geometry and
determine*/

#define LAMBDA_END_INSULATOR  1.6e-5       /* Lambda at which the end of
the
                                     insulator is reached and
                                     contact is made with a metallic
                                     pole piece */

#define LAMBDA_END_INSULATOR_TOP   1.6e-5  /* on the top -- JS */

#define LAMBDA_END_INSULATOR_BOTTOM  1.6e-5 /* on the bottom -- JS */

#define N_LAMBDA            150     /* 160 integrations per timestep */
#define N_LAMBDA_PLUME      0      /* Number of lambda beyond cathode
*/
#define DCHI                .0005   /* .0008 Delta Chi for integration
*/
#define MAX_VALS            300    /* 300 maximum number of DCHI steps
*/
#define NEUMANN_ANODE       1        /* Neumann conditions at anode? */
#define ANODE_REGION      LINEAR    /* how to treat the anode region */
#define RESID_CONV          1.0e2          /* Te convergence (K) Note:
                                this must be low enough for
                                the iterative t_e newton
                                scheme to work in hall.c */
#define SMOOTH2             0           /* use second order smoothing?
*/
#define SMOOTH2_CONST       1e8            /* constant for second order
                                smoothing 1e8 */
#define SMOOTH4             0           /* use fourth order smoothing?
*/
#define SMOOTH4_CONST       5e4            /* constant for fourth order
                                smoothing 5e4 */
#define LINEARIZE_TERMS     0          /* linearize nedot and loss_phi
*/
#define DIFFUSE_CONST      1.0             /* constant for diffusion */
#define MOBILITY_FACTOR    1.0
#define CLASSICAL_K        0.0       /* mu[j][k] = mu_classical + mu_b */

/* mike has removed the slip velocity */
#define SLIP_VELOCITY       0              /* use the electron slip vel?
```

```
#define STEADY_STATE       0              /* 1: steady-state, 0:
temporal */
extern int FIXED_T_E;
/*#define FIXED_T_E          0 */             /* for debugging */
#define T_E(lambda) ((16.0-sqrt(sqrt((lambda-1.6e-5)*(lambda-1.6e-
5))/1.6e-5)*14.0)*11600.0)
    /*This is used for an initial guess -- Te as a function of lambda
*/
                            /*((16.0 - 3.93e6*lambda)*11600.0) -- SPT
*/
#define GUESS_T_E          1           /* guess at the electron temp.
*/
#define CATHODE_BC       DIRICHLET     /* cathode BC for electrons */
#define T_E_CATHODE     23200.0        /* cathode Te for Dirichlet BC
*/
#define WALL_LOSS      DETAILED_WALL    /* treatment of wall loss and
                                  conductivity */

/*---------------------------------------------------------------------
*/
/* Grid definitions  */
/*---------------------------------------------------------------------
*/

#elif (GEOMETRY==SPT_100)

#define N_Z             57          /* z-nodes 47*/
#define N_R             22          /* r-nodea 22*/
#define N_Z_AZ_1        30          /* nodes in AZ 30*/
#define N_Z_AZ_2        27          /* nodes in AZ 27*/
#define RAD_1           .0344    /* radial length to inner accel. wall
*/
#define RAD_2           .0500    /* radial length to outer accel. wall
*/

#define L_Z_1           .0248      /* length of accelerator inner wall
*/
#define L_Z_2           .0248      /* length of accelerator outer wall
*/
#define BOTTOM_MARGIN   .000       /* margin so r != 0 */
#define DZ0             .001       /* first cell width at the anode */

#define N_RC             0
#define ERRORMAX         .00001


#define ORTHOGONAL       1         /* 1 makes boundaries orthogonal */
#define ORTHO_TOP        1         /* unstable with gazillions of pts */
#define ORTHO_BOTTOM     1
#define ORTHO_LEFT       0
#define ORTHO_RIGHT      0


#define A_RHS            10          /* P weight bottom */
#define B_RHS            15          /* P weight top */
#define C_RHS            10          /* P weight left */
#define D_RHS            10          /* Q weight bottom */
```

```
#define E_RHS           15          /* Q weight top */
#define F_RHS           10          /* Q weight left */

#define FIRST_WIDTH_1   0.5       /* width of first cell nominal .25 */
#define FIRST_WIDTH_2   0.5


/*-------------------------------------------------------------------
*/
/* Definitions for ionize.c  */
/*-------------------------------------------------------------------
*/
/* IPC constants see 10/26/95 */
#define IPC_MIN          0.5   /* .7 for more -- min ionizations per
cell */
#define IPC_MAX          1.0      /* 1.0  max ionizations per cell */
#define N_I_DOT_MIN      4e23       /* where IPC_MIN is reached */
#define N_I_DOT_MAX      4e24       /* where IPC_MAX is reached */
/* these constants control the number of ions which appear -- if IPC-
min
   is too low, you'll have massive ions, but not enough of 'em */

/*-------------------------------------------------------------------*/
/* Definitions for the magnetic field  */
/*-------------------------------------------------------------------
*/
#define COARSE_MARGIN         .01
#define RESIDUAL_CONVERGENCE  1.0e-14    /* convergence criteria for
lambda */
#define MAX_LAMBDA_IT         4000
#define RELAX                 1.0        /* lambda's over-relaxation */
#define SMOOTH                1.0e-8     /* smoothing */


/*-------------------------------------------------------------------
*/
/* PPU-related constants  */
/*-------------------------------------------------------------------
*/

#define I_MAX        12.0    /* max current for constant voltage mode*/
#define MAX_POWER        3600.0    /* maximum power output (W)  450*/
#define V_0              300.0   /* Anode voltage initial guess */
#define R_1               20     /* 20.0    spt-100 value */
#define C_1               1.0e-4 /*1.0e-4   spt-100 value */
#define R_M               1.0 /* 1.0       spt-100 value */
#define L_M               1.0e-2 /* 1.0e-2    spt-100 value */
#define V_R_0            2.0    /* expected error variance in Vd */


/*-------------------------------------------------------------------
*/
/* Miscellaneous constants  */
/*-------------------------------------------------------------------
*/
#define ERROR_SQ_MAX     7.11e-10  /* on-tenth of the smallest cell
width --
```

```
                                        used in ion.c, neutral.c */
#define MIN_NEUTRAL_MASS (MASS_ION*10.0)
#define MIN_ION_MASS     (MASS_ION*10.0)
```

a.inp

```
<Case name to prefix hall output data files - Null prefix permitted.>

<Separate file name prefix for grid.dat - Null prefix permitted.>

<Separate file name prefix for sigma.dat - Null prefix permitted.>

<Separate file name prefix for BG2 output files - Null prefix
permitted.>

<XI_INJ_MIN  XI_INJ_MAX  ETA_INJ_MIN  ETA_INJ_MAX>
1.0           1.05         5.0         9.0
<M_DOT  I_A_0>
5e-6  4.0
<SAVE_ITS>
2000
<P_CHAMBER  T_CHAMBER>
5.0e-5     300.0
<B_0  PHI_ANODE>
.020  300.0
<PPU_TYPE>
CONSTANT_VOLTAGE
<DT NEUTRALS_PER_DT>
5e-8  2.0
<LOG_DATA NEUTRALS_ONLY IONS_ONLY PARTICLES_ONLY>
1 0 0 0
<FIXED_T_E>
0
<Q_I_N_MOMENTUM Q_I_N_CHARGE_EX>
2.15e-18 4.8e-19
<Q_E_N_MOMENTUM>
22e-20
<BOHM_K>
.15
```

2240-17